

DEPARTMENT OF PHYSICS  
UNIVERSITY OF JYVÄSKYLÄ  
RESEARCH REPORT No. 1/2012

**High-Precision Momentum Measurements of  
Projectile Fragments in Sn+Sn Collisions  
at 1·A GeV**

by

**Ville Föhr**

Academic Dissertation  
for the Degree of  
Doctor of Philosophy

*To be presented, by permission of the  
Faculty of Mathematics and Science  
of the University of Jyväskylä,  
for public examination in Auditorium FYS-1 of the  
University of Jyväskylä on January 27, 2012  
at 12 o'clock noon*



Jyväskylä, Finland  
January 2012



# Preface

My involvement with this work began in the early 2006, out of a suggestion by Timo Enqvist, who was the supervisor of my master thesis and a former member of the CHARMS<sup>1</sup> group at GSI. He introduced me the possibility to work in this group led by Karl-Heinz Schmidt whom I visited later in 2006 and he invited me to join this new subject in my career. Ever since he has provided fruitful and exciting discussion on the physics as well as on the life itself which at times may be indistinguishable. Aleksandra Kelić-Heil, as the new leader of the CHARMS group, took the heavy burden of being my supervisor at GSI. She holds the honour of providing the biggest portion to accomplishing this work and for that I'm forever thankful.

I am especially grateful to professor Juha Äystö, my supervisor at the Department of Physics in the University of Jyväskylä, for his continuous encouragement and devotion on my graduate studies and for the opportunity to do my thesis work in a collaboration between the University of Jyväskylä and GSI.

I would like to thank all my other CHARMS friends Maria Valentina Ricciardi, Radek Pleskač, Strahinja Lukić and Antoine Bacquias with whom I had a great pleasure of sharing the same office for quite a while. I am indebted to the whole collaboration group members, who have introduced me to the FRS, to the code calculations and to the correct understanding of the physical processes. With these people I had the pleasure to participate numerous coffee break discussions and other recreational activities.

I would like to thank the reviewers Alain Boudard and Haik Simon for the careful reading and correction of this work.

I want to express my gratitude to my parents, my sister Anne, and my uncle Samuel for encouraging me in my physics studies. For the same reasons I also want to thank my parents-in-law and all my friends, especially Pekka, who showed remarkable effort in the search for the baryonic “dark matter”.

Finally, I would like to dedicate my deepest thanks to my beloved wife Pia. She is the one who kept me going in the everyday life, who supported and

---

<sup>1</sup><http://www-wnt.gsi.de/charms/>

accompanied me in all the times outside the work. This work would have not accomplished without your constant inspiration and motivation. During this journey I've had the pleasure to wed you and to have a wonderful son with you.

Jyväskylä, January 2012

Ville Föhr

# Abstract

Föhr, Ville

**High-Precision Momentum Measurements of Projectile Fragments  
in Sn+Sn Collisions**

at 1.4 GeV

Jyväskylä: University of Jyväskylä, 2012, 146 p.

Department of Physics Research Report No. 1/2012

ISSN: 0075-465X; 1/2012

ISBN: 978-951-39-4630-2 (paper version)

ISBN: 978-951-39-4631-9 (electronic version)

Diss.

Production cross-sections and longitudinal velocity distributions of the projectile-like residues produced in peripheral and mid-peripheral reactions  $^{112}\text{Sn} + ^{112}\text{Sn}$  and  $^{124}\text{Sn} + ^{124}\text{Sn}$  both at an incident beam energy of 1.4 GeV were measured with the high-resolution magnetic spectrometer, the Fragment Separator of GSI. For both reactions the characteristics of the velocity distributions and nuclide production cross-sections were determined for residues with nuclear charge  $Z \geq 10$ . A comparison of the results of the two reactions is presented and the results are studied in the frame of dynamical transport calculations coupled with a statistical multifragmentation code. In mid-peripheral collisions the simulations show that the rapidly expanding participant zone interacts with the spectator matter giving substantial increase on the longitudinal velocity that shows sensitivity to the nucleon-nucleon cross section and to the momentum dependence of the nuclear mean field.

**Keywords:** heavy ion: scattering, nuclide: yield, magnetic spectrometer: experimental results, velocity spectrum, Darmstadt SIS, 1 GeV/nucleon, fragmentation, multi-fragmentation, abrasion-ablation, equation of state, momentum dependence, transport theory, mean field approximation

**Author's address** Ville Föhr  
Department of Physics  
University of Jyväskylä  
Finland

**Supervisors** Dr. Aleksandra Kelić-Heil  
GSI—Helmholtzzentrum für Schwerionenforschung GmbH.  
Darmstadt  
Germany

Prof. Juha Äystö  
Department of Physics  
University of Jyväskylä  
Finland

**Reviewers** Dr. Haik Simon  
GSI—Helmholtzzentrum für Schwerionenforschung GmbH.  
Darmstadt  
Germany

Dr. Alain Boudard  
CEA/Saclay Orme des Merisiers  
Gif-sur-Yvette Cedex  
France

**Opponent** Prof. Pawel Danielewicz  
National Superconducting Cyclotron Laboratory  
Michigan State University  
United States of America

# Contents

<b>1</b>	<b>Introduction</b>	<b>21</b>
<b>2</b>	<b>The Experiment</b>	<b>27</b>
2.1	Accelerator facility at GSI . . . . .	28
2.1.1	The heavy-ion synchrotron SIS18 . . . . .	29
2.1.2	The FRagment Separator . . . . .	29
2.2	Experimental setup . . . . .	34
2.2.1	The Hall probes . . . . .	35
2.2.2	Multiwire proportional chambers . . . . .	35
2.2.3	Plastic scintillators . . . . .	36
2.2.4	MUlti-Sampling Ionization Chambers . . . . .	38
<b>3</b>	<b>Data analysis</b>	<b>41</b>
3.1	Calibrations . . . . .	41
3.1.1	Calibration of beam monitor . . . . .	42
3.1.2	Determination of the parameters for magnetic deflection	42
3.1.3	Calibration of the scintillators . . . . .	46
3.1.4	Time-of-flight calibration . . . . .	47

3.1.5	Corrections of the energy-loss signals . . . . .	49
3.1.6	Mass and nuclear charge identification . . . . .	51
3.2	Measuring the velocity distributions . . . . .	53
3.2.1	Correction for the beam dose . . . . .	56
3.2.2	Dead time determination . . . . .	56
3.2.3	Correction for the reduced FRS angular transmission . . . . .	58
3.2.4	Reconstruction of the velocity distributions . . . . .	58
3.3	Evaluation of the formation cross-sections . . . . .	61
3.3.1	Target thickness . . . . .	61
3.3.2	Correction for the limited angular acceptance . . . . .	62
3.3.3	Correction for secondary reactions . . . . .	63
3.4	Error analysis . . . . .	64
3.4.1	Uncertainty of the velocity distribution . . . . .	65
3.4.2	Uncertainty of the production cross section . . . . .	66
<b>4</b>	<b>Experimental results</b>	<b>69</b>
4.1	Velocity distributions and their moments . . . . .	69
4.1.1	Width of the velocity distributions . . . . .	72
4.1.2	Mean value of the velocity distributions . . . . .	75
4.2	Production cross-sections . . . . .	77
<b>5</b>	<b>Theoretical models</b>	<b>85</b>
5.1	Projectile fragmentation in non-central heavy-ion collisions . . . . .	85
5.2	Collision stage . . . . .	86
5.3	Break-up stage . . . . .	88
5.4	Ablation stage . . . . .	90

---

<b>6</b>	<b>Data interpretation</b>	<b>91</b>
6.1	Asymmetry of the measured velocity distributions . . . . .	94
6.2	Mean longitudinal velocity . . . . .	97
<b>7</b>	<b>Calculations</b>	<b>101</b>
7.1	Boltzmann-Uehling-Uhlenbeck (BUU) transport model . . . . .	101
7.1.1	Results from the BUU calculations . . . . .	105
7.2	Coupling with ABRABLA . . . . .	109
7.3	Discussion . . . . .	111
<b>8</b>	<b>Conclusion</b>	<b>115</b>
<b>A</b>	<b>Information of the used targets</b>	<b>119</b>
<b>B</b>	<b>Layers of matter in the experiment.</b>	<b>121</b>
<b>C</b>	<b>FRS Magnetic settings</b>	<b>125</b>
<b>D</b>	<b>Production cross-sections</b>	<b>129</b>



# List of Tables

3.1	Summary of time-of-flight calibration measurement. . . . .	49
3.2	Numerical values used in the equation 3.19. . . . .	62
3.3	Examples of the transmission coefficients and their estimated uncertainties for two different trajectories passing the focal planes at $x_{S2}$ and $x_{S4}$ . . . . .	66
7.1	Values for the parameters in the mean field used in the calculations. First three parameters $a$ , $b$ and $\nu$ refer to Eq. 7.4 and the next two to Eq. 7.6. $m^*/m$ is the Landau effective mass in normal matter at Fermi momentum. The last column gives the incompressibility of nuclear matter. . . . .	103
7.2	Summary of the BUU calculations performed with different parameters. . . . .	105
A.1	Isotopic composition of $^{112}\text{Sn}$ target. . . . .	119
A.2	Chemical impurities of $^{112}\text{Sn}$ target. . . . .	119
A.3	Isotopic composition of $^{124}\text{Sn}$ target. . . . .	119
A.4	Chemical impurities of $^{124}\text{Sn}$ target. . . . .	120

B.1	List of layers in the beam line. In the third column the nuclear charge of the layer material is given or if the layer consist of several different materials then the thickness is given in aluminum equivalent units ( $Z=13$ ). The setup column indicates the following: Calib.: The layer is used in the beam line during calibration runs only, Meas.: The layer is used in the beam line during the data measurement. . . . .	124
C.1	List of FRS magnetic field setting used to measure the data in $^{112}\text{Sn} + ^{112}\text{Sn}$ experiment. . . . .	126
C.2	List of FRS magnetic field setting used to measure the data in $^{124}\text{Sn} + ^{124}\text{Sn}$ experiment. . . . .	127
D.1	Production cross sections . . . . .	129
D.2	Production cross sections . . . . .	131

# List of Figures

1.1	Figure is reprinted from ref. [Mor89]. Explanation of data points can be found from the reference. The line marks the Morrissey systematics. . . . .	23
1.2	Mean values of the velocity distributions of reaction residues, excluding fission, produced in $^{238}\text{U} + \text{Pb}$ [E <sup>+</sup> 99] (solid squares) and $^{238}\text{U} + \text{Ti}$ [REP <sup>+</sup> 03] (open circles) at 1·A GeV in the frame of the projectile. Relative uncertainties are shown. The absolute uncertainty amounts to less than 0.05 cm/ns for each system, $^{238}\text{U} + \text{Pb}$ and $^{238}\text{U} + \text{Ti}$ , independently. The dashed line marks the Morrissey systematics [Mor89]. Figure is taken from ref. [REP <sup>+</sup> 03]. . . . .	24
1.3	The change in the net average c.m. momentum per nucleon $\Delta  < P/A >  $ of the spectator in the $^{197}\text{Au} + ^{197}\text{Au}$ system at $T_{lab} = 1\cdot A$ GeV. Open symbols represents results obtained with reduced in-medium nucleon-nucleon cross sections; filled symbols represent results obtained at $b = 6$ fm with free cross sections. A negative value of $\Delta  < P/A >  $ indicates a spectator deceleration, while a positive value indicates a net acceleration. Figure is taken from Ref. [SDL01]. . . . .	25
2.1	A schematic drawing of the GSI facility showing the linear accelerator (UNILAC), synchrotron (SIS), fragment separator (FRS), storage ring (ESR) and several experimental areas designed for different research purposes. . . . .	28
2.2	A schematic drawing characterizing the ion-optical elements of the FRS. . . . .	30

2.3	Fragment selection criteria of the FRS determined by one magnetic field setting in the first stage of the FRS (red dashed lines) and in the second stage of the FRS (black dashed lines) with respect to the nuclear chart. . . . .	32
2.4	Measurements of the $x$ and $y$ position of the beam by Multiwire Proportional Counters at the dispersive image plane S2 during the initial calibration measurements. . . . .	33
2.5	Schematic view of the Fragment Separator (FRS) and the associated detector equipment used in this experiment. The notation of different detectors is explained in the text. More technical drawings with accurate detector positions can be found in Appendix B. . . . .	35
2.6	A schematic diagram of the treatment of the signals from two scintillators used in the experiment for measuring the $x$ -positions at S2 and at S4 and of the time-of-flight of the fragment. Photomultiplier's (PM) signals pass by constant-fraction discriminators to impose a lower threshold and to eliminate the pulse-height dependence of the timing signal. The ADC signals are recorded to the DAQ. . . . .	37
2.7	A schematic view of the parallel-plate ionization chamber used in the experiment. . . . .	39
3.1	Determination of the calibration factor of SEETRAM output. Dashed line shows the quadratic calibration curve fitted to the data showing scintillator counts versus the SEETRAM output. Solid line shows the linear part of the fit. . . . .	43
3.2	Determination of the calibration factor for TRAF0 counts. Dashed line represents the linear calibration fit to the data showing the SEETRAM output versus the TRAF0 output. . . . .	43
3.3	Measurement of the dispersion at S2 and a linear fit of the measured values. Slope of the fit determines the dispersion. . . . .	45

- 3.4 (a) 2-dimensional plot showing the uncorrected scintillator signal versus the energy loss measured by the MUSIC detectors. (b) Same plot after the correction for the walk of the CFD-units. The effect of the correction is seen especially for the lower energy loss signals corresponding to ion charge states from 10 to 28. The dashed lines corresponds to the physical borders of the scintillator plane. The color scale representing the bin count is logarithmic. . . . . 47
- 3.5 Position information of MW21 plotted against the SCI21 data during the measurements used for dispersion determination as described in section 3.1.2. The fitted curve represent the obtained calibration curve of the SCI21. . . . . 48
- 3.6 Calibration of the TAC units with a pulse generator for the *ToF* measurements: (a) signals from the left sides of the scintillators SCI21 and SCI41. (b) signals from the right sides of the scintillators SCI21 and SCI41. The distance between two peaks corresponds to a time of 10 ns. . . . . 48
- 3.7 Time-of-flight calibration: Lines are linear fits of the measured values. Fits define the time delay  $\Delta t$  and the total flight path  $s_0$  according to the equation 3.6. . . . . 50
- 3.8 Nuclear charge resolution determined from the average energy loss in the MUSIC detectors before (light blue) and after the correction for the position at S4 and for the velocity of the passing fragments (black). . . . . 51
- 3.9 Angle of the fragments flight path through the FRS measured with the MUSIC detectors plotted as a function of the  $A/Z$  ratio: (a) before the angle correction and (b) after the angle correction. Data was measured during the experiment  $^{124}\text{Sn} + ^{124}\text{Sn}$ . . . . 52
- 3.10 A close-up of the recognition pattern of fragments  $^{58}\text{Co}$ ,  $^{59}\text{Co}$  and  $^{60}\text{Co}$  formed in  $^{124}\text{Sn} + ^{124}\text{Sn}$  reactions. Recognized isotopes are enclosed with black line segments, that are used as conditions in further analysis. Projections to both dimensions of the 2-dimensional histogram are shown. Limits used in the plot and in the projections are the following:  $Z \in [25.5, 28]$  and  $A/Z \in [2.27, 2.33]$ . 54
- 3.11 Recognition patterns of fragments formed in  $^{112}\text{Sn} + ^{112}\text{Sn}$  reactions. Settings measured with degrader (left) are shown separately from those obtained without degrader (right). . . . . 55

3.12	Recognition patterns of fragments formed in $^{124}\text{Sn} + ^{124}\text{Sn}$ reactions. Settings measured with degrader (left) are shown separately from those obtained without degrader (right). . . . .	55
3.13	Dead time determination by comparing accepted triggers to actual recorded events. . . . .	57
3.14	Transmission matrix used in the experiments to compensate the losses due to the reduced transmission inside the angular acceptance of the FRS. Matrix is obtained from the ion optical calculation described in the reference [BPCS02]. The color coding corresponds to penetration factor of the ion through the FRS determined completely by the fragments horizontal position at S2 and S4. . . . .	59
3.15	(a) Velocity distributions of the isotope $^{22}\text{Ne}$ ( $Z=10, A=22$ ) measured in the $^{124}\text{Sn} + ^{124}\text{Sn}$ experiment in total of 14 different magnetic field settings that are shown separated. (b) The full velocity distribution of $^{22}\text{Ne}$ after the joining described by the Eq. 3.14. The error bars are shown for each bin of the velocity distribution. Certain periodic structure due to imperfectness of the joining and due to imperfect correction for the reduced angular transmission can be seen. . . . .	60
3.16	Secondary-reaction correction factor in different layers of matter obtained from AMADEUS [Sch] calculation. . . . .	64
4.1	Velocity distributions in the rest frame of the projectile for several nuclides measured in the reaction $^{124}\text{Sn} + ^{124}\text{Sn}$ . The fitted functions are shown as dotted lines. . . . .	70
4.2	Velocity distributions in the rest frame of the projectile for several nuclides measured in the reaction $^{112}\text{Sn} + ^{112}\text{Sn}$ . The fitted functions are shown as dotted lines. . . . .	71
4.3	Left: Longitudinal velocity distributions in the rest frame of the projectile as function of the fragment's nuclear charge measured in the reaction $^{112}\text{Sn} + ^{112}\text{Sn}$ . Right: Same plot for the fragments measured in the reaction $^{124}\text{Sn} + ^{124}\text{Sn}$ . The color scale is logarithmic and represents the relative abundances of the velocity for each mass number of the fragment. . . . .	73

4.4	Standard deviation of the Gaussian part of the fitted functions to the fragment momentum distributions for both systems; $^{112}\text{Sn}(1.4\text{ GeV})+^{112}\text{Sn}$ (upper diagram) and $^{124}\text{Sn}(1.4\text{ GeV})+^{124}\text{Sn}$ (lower diagram). Given curves represent the prediction of Bacquias <i>et al</i> [BFH <sup>+</sup> 11] (green), model of Goldhaber [Gol74] (blue) and the empirical parametrization by Morrissey [Mor89] (red). . . . .	74
4.5	Mean value of the longitudinal velocity distributions in the frame of the projectile of residues produced in peripheral and mid-peripheral collisions for the systems $^{124}\text{Sn}(1.4\text{ GeV})+^{124}\text{Sn}$ (open squares) and $^{112}\text{Sn}(1.4\text{ GeV})+^{112}\text{Sn}$ (filled circles) as a function of their relative mass loss. The data points are weighted averages of the mean values of the different isobars. The mean values represent the mean velocities inside an angular range of 15 mrad. . . . .	76
4.6	Cross-sections for both systems; $^{112}\text{Sn}(1.4\text{ GeV})+^{112}\text{Sn}$ (upper diagram) and $^{124}\text{Sn}(1.4\text{ GeV})+^{124}\text{Sn}$ (lower diagram). . . . .	78
4.7	Isotopic cross-sections of the measured fragments with nuclear charge $Z=10$ to $Z=25$ in the reaction $^{112}\text{Sn} + ^{112}\text{Sn} @ 1.4\text{ GeV}$ (filled dots) and in $^{124}\text{Sn} + ^{124}\text{Sn} @ 1.4\text{ GeV}$ (open squares). Dashed lines represent the prediction of EPAX [SB00] for $^{112}\text{Sn} + ^{112}\text{Sn}$ and solid lines for $^{124}\text{Sn} + ^{124}\text{Sn}$ . . . . .	79
4.8	Isotopic cross-sections of the measured fragments with nuclear charge $Z=26$ to $Z=41$ in the reaction $^{112}\text{Sn} + ^{112}\text{Sn} @ 1.4\text{ GeV}$ (filled dots) and in $^{124}\text{Sn} + ^{124}\text{Sn} @ 1.4\text{ GeV}$ (open squares). Dashed lines represent the prediction of EPAX [SB00] for $^{112}\text{Sn} + ^{112}\text{Sn}$ and solid lines for $^{124}\text{Sn} + ^{124}\text{Sn}$ . . . . .	80
4.9	Isotopic cross-sections of the measured fragments with nuclear charge $Z=42$ to $Z=50$ in the reaction $^{112}\text{Sn} + ^{112}\text{Sn} @ 1.4\text{ GeV}$ (filled dots) and in $^{124}\text{Sn} + ^{124}\text{Sn} @ 1.4\text{ GeV}$ (open squares). Dashed lines represent the prediction of EPAX [SB00] for $^{112}\text{Sn} + ^{112}\text{Sn}$ and solid lines for $^{124}\text{Sn} + ^{124}\text{Sn}$ . . . . .	81
4.10	Mean neutron-to-proton ratio found in the isotopic distributions of $^{112}\text{Sn} + ^{112}\text{Sn}$ and in $^{124}\text{Sn} + ^{124}\text{Sn}$ at 1.4 GeV. Dashed lines represent the prediction of EPAX [SB00] for $^{112}\text{Sn} + ^{112}\text{Sn}$ and solid lines for $^{124}\text{Sn} + ^{124}\text{Sn}$ . . . . .	83

- 5.1 Schematic view of a relativistic heavy-ion collision: a neon nucleus collides with an incident velocity  $\beta_{inc}$  on the uranium nucleus in the laboratory frame with an impact parameter 5 fm. The swept-out nucleons from the projectile and target are called the fireball, and their center of mass has the velocity  $\beta$  in the laboratory frame. The figure is reprinted from Ref. [WGJ<sup>+</sup>76]. 86
- 5.2 Second largest atomic number as a function of the largest atomic number  $Z_{max}$  observed in an ALADIN experiment for the reaction  $^{136}\text{Xe}$  (600-A MeV) + Al (panel a). Colors depict the relative cross-sections, in logarithmic scale. Panel b shows the probability of observed fragment with nuclear charge  $Z$  being the heaviest fragment produced in the event. . . . . 89
- 6.1 Longitudinal velocity distribution in the beam frame of the various reaction products (see text for details) according to ABRABLA [GS91] simulation, as a function of mass number in reactions  $^{124}\text{Sn} + ^{124}\text{Sn}$  (left panels) and  $^{112}\text{Sn} + ^{112}\text{Sn}$  (right panels). See the text for details. Both reactions have the initial projectile energy of 1-A GeV. In total one million reactions were simulated to accumulate the spectra. The cut due to the FRS angular acceptance is applied [BPCS02]. . . . . 93
- 6.2 Longitudinal velocity distribution in the beam frame of three different fragments produced in the reaction  $^{136}\text{Xe}(1\text{-A GeV}) + p$ . The corresponding (expected) global distributions in the  $(v_{\parallel}; v_{\perp})$  plane and the limits of the FRS acceptance are displayed on the right. Taken from [NSTG<sup>+</sup>07]. . . . . 95
- 6.3 Longitudinal velocity distribution of fragment  $^{31}\text{P}$  (histogram) together with the 3 Gaussian fit functions, revised with ABRABLA calculation (green), and a sum of them (red) reproducing the data. 96
- 7.1 Contour plots of the system-frame baryon density at several time steps projected to the reaction plane in BUU simulation of  $^{124}\text{Sn} + ^{124}\text{Sn}$  at 1-A GeV and  $b = 7$  fm. The time steps are written on each panel. Right bottom corner representing time 160 fm/c. The calculations have been carried out employing the soft momentum-dependent EOS. The contour lines for the densities correspond to the values, relative to the normal density. . . . . 106

- 7.2 Time development of the prefragment mass (a) and the velocity in the center of mass frame (b). BUU simulation is carried out with the momentum independent (MI) mean field, SOFT EoS and In-medium cross section for different impact parameters in the collision of  $^{124}\text{Sn} + ^{124}\text{Sn}$  at 1.4 GeV. Both quantities display saturation well at the time 160 fm/c, which is the chosen time step to use as input for the evaporation code ABRABLA [GS91]. . . . . 107
- 7.3 Results of the BUU simulation for the average momentum per mass of the projectile prefragment as function of impact parameter formed in the reaction  $^{112}\text{Sn} + ^{112}\text{Sn}$  at 1.4 GeV (panel a) and in  $^{124}\text{Sn} + ^{124}\text{Sn}$  at 1.4 GeV (panel b). Varied parameters are: momentum dependence of the mean field (MD/MI), nucleon-nucleon cross section (FREE/IN-MED), and to lesser extend the incompressibility of nuclear matter (SOFT/HARD). Numerical fluctuations are shown as error bars in the studied cases at  $b=5.5$  and  $b=11.5$ . . . . . 108
- 7.4 Results of the evaporation code ABRABLA for the reaction  $^{124}\text{Sn} + ^{124}\text{Sn}$  at 1.4 GeV. Calculations reveal the dispersion in the final residue mass due to the de-excitation processes as function of initial impact parameter (panel a) or as function of prefragment mass (panel b). . . . . 110
- 7.5 Mean values of the longitudinal velocity distributions of the final residues as measured in  $^{112}\text{Sn} + ^{112}\text{Sn}$  and in  $^{124}\text{Sn} + ^{124}\text{Sn}$  at 1.4 GeV together with the coupled calculations performed with BUU + ABRABLA. Experimental data is shown in symbols and model calculations in solid lines. Experimental error bars are not plotted for clarity. (MI,IN-MED) corresponds to the momentum independent mean field and reduced nucleon-nucleon cross section and (MD,FREE) corresponds to the momentum dependent mean field and free nucleon-nucleon cross section. All simulations are performed with the soft EOS. Calculations with these two different parameter configurations are shown for both systems because they produce the lowest (MI,IN-MED) and the highest (MD,FREE) residue velocities according to Fig. 7.3. . . 112

- B.1 Detector positions during the experiments at S2, the intermediate image plane of the FRS. After the vacuum window we have the first multiwire chamber (MW21), slits, plastic scintillator SCI21, the second multiwire chamber (MW22) and lastly the degrader. Positions of the mentioned elements are given as distances in units of mm measured from the last vacuum window of the FRS along the central beam line. . . . . 122
- B.2 Detector positions during the experiments at S4, the final image plane of the FRS. After the vacuum window we have the multiwire chamber (MW41), the first MUSIC detector (MUSIC41), the second MUSIC detector (MUSIC42), slits, the second multiwire chamber (MW42) and lastly the plastic scintillator SCI41. Positions of the mentioned elements are given as distances in units of mm measured from the last vacuum window of the FRS along the central beam line. . . . . 123

# Chapter 1

## Introduction

Since heavy-ion beams at relativistic energies  $E > 100 \cdot A$  MeV became available in laboratories [GGL<sup>+</sup>84, Kie88], a possibility to study static and dynamic properties of nuclear matter over a wide range of temperature and density has been opened [GH78, Poc97]. Depending on the impact parameter  $b$ , heavy-ion collisions can be divided into three groups [BP49]:

One extreme are central collisions in which projectile and target completely overlap. In this type of collisions, high densities and high excitation energies can be achieved [BG88], and thus they appear to be an excellent tool to study the equation of state of hot and compressed nuclear matter as well as in-medium nucleon-nucleon interactions. To this goal, immense experimental effort has been, and is still being, invested to measure for example the flow pattern of nucleons and particles, kaon production or charged-particles correlation in central heavy-ion collisions [RR97, Sen04, RAA<sup>+</sup>10]. Since high densities and high excitation energies are achieved only for short time intervals of the order  $10^{-22}$  s and in volumes of the order  $100 \text{ fm}^3$  [CSFN90], it is mandatory to understand the complete dynamic evolution of the reaction in order to extract the information on the nuclear equation of state under these extreme conditions. This is still not an easy task.

An other extreme is the case of large impact parameters leading to very peripheral collisions. This type of collisions is characterized by a small mass loss in projectile and/or target and rather low excitation energies. Projectile-like fragments move with velocities very close to the original one of the projectile. These collisions have been proved to be an excellent tool to study e.g. nuclear-structure effects at large deformations [SSB<sup>+</sup>00, SBB<sup>+</sup>98, RIJS00] or different spatial distributions of neutrons and protons, in particular near the surface [KPA<sup>+</sup>07].

For the intermediate range of impact parameters, a considerable amount of excitation energy [SBC<sup>+</sup>93] and a slight linear momentum transfer are induced, but compression is small. Thus, the mid-peripheral heavy-ion collisions at relativistic energies are an ideal scenario for studying multifragment decay of the spectator matter due to purely thermal instabilities [SKW<sup>+</sup>96], avoiding any compression effect. Multifragmentation reactions have been extensively studied in order to search for the signals of the liquid-gas phase transition in finite nuclear systems [Poc97, PMR<sup>+</sup>95, Tra05]. Since some time, isotopic effects in multifragmentation reactions also gained a lot of interest [BLT02, TZD<sup>+</sup>09, LGL09, Tra08], as neutron-star models or supernova simulations demand a nuclear equation of state similar to those met in mid-peripheral relativistic heavy-ion collisions [DPBB94, DKLR95, BM04]. Similar to the experiments where central collisions are studied, a lot of effort is invested in developing devices covering the full solid angle in order to attain particle multiplicities as well as correlations between observed particles.

This intermediate range of impact parameters in heavy-ion collisions at relativistic energies have been for long and successfully described by the geometrical abrasion model [BST73], which suggests a clear cut between participant matter, corresponding to the overlap zone of the two nuclei, and spectator matter outside the overlap zone. The part of the projectile nucleons, encountering the target nucleons in the overlapping volume, are decelerated and their longitudinal kinetic energy is converted into thermal and potential compression energy. After the compression phase, a rapid expansion or a so-called participant blast occurs [SDL01], where the matter in the participant region may expand also in the transverse directions. For a certain range of beam energies, the particles emitted from the participant zone towards the reaction plane can encounter the spectators and get redirected or absorbed. On the contrary, the particles emitted essentially perpendicular to the reaction plane are largely unhindered by the spectators. This gives rise to so-called elliptic flow pattern of the participant matter, which means that the presence of the cold spectator matter blocks the in-plane expansion of the participant matter and causes the out-of-plane transverse direction to be more favorable [GKK<sup>+</sup>90, DP92, Dan95, RR97, PCG<sup>+</sup>96]. This collective behavior of participant matter is also commonly referred as the squeeze-out which has been under intense study with hydrodynamical models [DLG<sup>+</sup>98, Dan00, GKK<sup>+</sup>90]. The squeeze-out is found to be governed by the collision geometry and the passage time of the shadowing projectile and target spectators, as well as by the pace at which the expansion develops, and therefore is connected to the nuclear equation of state.

On the other hand, since the spectators serve to deflect particle emissions toward the reaction plane, their properties may be significantly modified. The spectators can be viewed as probes which were present at the site of the nuclear explosion leading to the rapid particle emission. This suggests that the spectator characteristics are sensitive to the nuclear force through the participant-

spectator interaction, and could provide a tool for investigating the equation of state of nuclear matter, that could complement the results obtained from the flow analysis. Especially interesting observable has proved to be the mean momentum of the spectator.

Unfortunately, detailed experimental information on kinematical properties of projectile residues produced in heavy-ion collisions at relativistic energies is rather lacking. A review on measured mean velocities of spectator-like fragments has been presented by Morrissey in 1989 [Mor89]. The collection of the data he used can be seen in Fig. 1.1 together with the systematics deduced from the data. A clear correlation between the observed momentum shift with

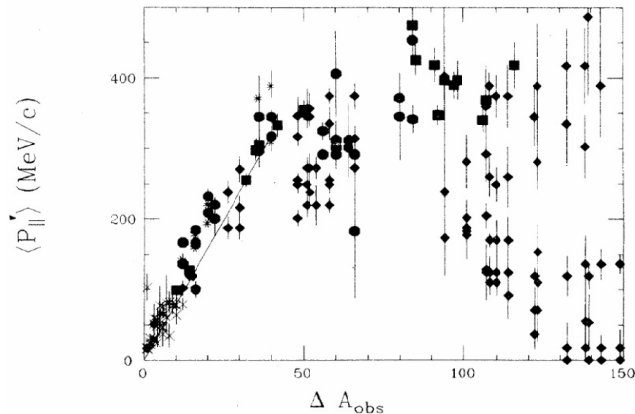


Figure 1.1: Figure is reprinted from ref. [Mor89]. Explanation of data points can be found from the reference. The line marks the Morrissey systematics.

the mass loss in very peripheral collisions has been observed. This shift has been interpreted as the consequence of friction in the nucleus-nucleus collision [Mor89, AMHS76]. On the other hand, the momentum distributions of lighter fragments, with a mass loss larger than about one-third of the mass of the projectile, respectively, the target nucleus, showed a large spreading with no clear tendency. In order to yield conclusive results, the momentum distributions of projectile residues have to be measured with high precision. This can only be achieved with high-resolution magnetic spectrometers, as experimental set-ups covering full solid angle do not have the required resolution. Since then, a lot of new data on the momentum distributions have been measured, but unfortunately only few of them cover the whole range - from projectile down to the lowest nuclear charges of produced fragments

[WDD<sup>+</sup>94, NSB<sup>+</sup>04, NSTG<sup>+</sup>07, HSR<sup>+</sup>08]. To overcome this lack of high-precision data on the velocities of projectile fragments, a dedicated experimental campaign [REP<sup>+</sup>03, Hen05] has been started at GSI using the heavy-ion accelerator SIS18 and the Fragment Separator (FRS).

First dedicated measurement was performed in 1999 [E<sup>+</sup>99] where for the first time velocities of  $^{238}\text{U}$  residues were measured down to the lightest nuclei. The mean momentum of the spectator residues as a function of mass-loss from the projectile, at first slows down, reaches a minimum, and becomes faster again for large mass losses. The results of this pioneering work and the one following it, are presented in Fig. 1.2. The lightest residues, i.e the ones after largest mass loss, produced in the heavy systems are found to become even faster than the beam particles. In these experiments the mean longitudinal velocities were measured with high enough precision to exclude any doubts of experimental error. In the later experiments, the spectator re-acceleration in other heavy reaction systems has been observed [REP<sup>+</sup>03, Hen05]. Driven by

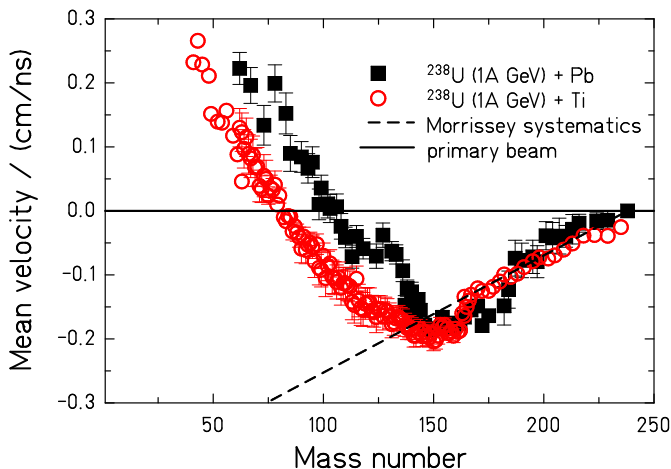


Figure 1.2: Mean values of the velocity distributions of reaction residues, excluding fission, produced in  $^{238}\text{U} + \text{Pb}$  [E<sup>+</sup>99] (solid squares) and  $^{238}\text{U} + \text{Ti}$  [REP<sup>+</sup>03] (open circles) at 1-A GeV in the frame of the projectile. Relative uncertainties are shown. The absolute uncertainty amounts to less than 0.05 cm/ns for each system,  $^{238}\text{U} + \text{Pb}$  and  $^{238}\text{U} + \text{Ti}$ , independently. The dashed line marks the Morrissey systematics [Mor89]. Figure is taken from ref. [REP<sup>+</sup>03].

the re-acceleration phenomena, the participant-spectator interaction and the longitudinal momentum transfer to spectators in energetic reactions were studied with a microscopic hydrodynamical transport code [SDL01]. According to

these calculations, the momentum distributions of spectator residues in mid-peripheral collisions should be sensitive to the nuclear force. Some results of these calculations are shown in Fig. 1.3 where the change in the net average c.m. momentum per nucleon of the spectator is presented as a function impact parameter. Calculations carried out with the momentum dependent mean field

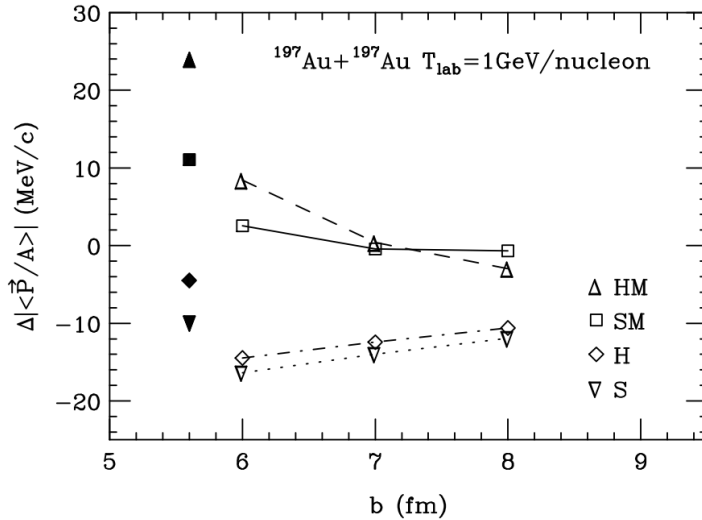


Figure 1.3: The change in the net average c.m. momentum per nucleon  $\Delta| \langle P/A \rangle |$  of the spectator in the  $^{197}\text{Au} + ^{197}\text{Au}$  system at  $T_{lab} = 1.0 \text{ GeV}$ . Open symbols represents results obtained with reduced in-medium nucleon-nucleon cross sections; filled symbols represent results obtained at  $b = 6 \text{ fm}$  with free cross sections. A negative value of  $\Delta| \langle P/A \rangle |$  indicates a spectator deceleration, while a positive value indicates a net acceleration. Figure is taken from Ref. [SDL01].

reveal the capability to produce the post-beam-velocity values of the residues with decreasing impact parameter in which the non-momentum dependent calculations failed. Also the use of free nucleon-nucleon cross section instead of the reduced in-medium cross section seems to enhance the spectator velocities. Despite the great success in reproducing the re-acceleration effect, the calculations carried out with microscopic BUU transport code had difficulties to explain the measured data in  $^{197}\text{Au} + ^{197}\text{Au}$  collisions at  $1.0 \text{ GeV}$  performed with the FRS by Henzl *et al.* [Hen05]. In the work of Henzl *et al.*, the re-acceleration was found to occur in much more peripheral collisions compared to the re-acceleration predicted by the theory. However these results were somewhat ambiguous since the calculations also failed to reproduce correctly the beam velocity, i.e. the velocity after zero mass loss. There are many difficulties in comparing the experimental results with microscopical calcula-

tions. Most experiments on nucleus-nucleus collisions provide the momentum of the projectile or target residue as a function of its mass. Neither the spectator mass, before evaporation, nor the mass loss due to evaporation can be measured due to the short time scale of the evaporation process. For the same reason it is not straight forward task to determine the impact parameter from which the observed residue may have emerged. On the other hand microscopic models are clumsy or incapable of describing the evaporation stage which is normally handled with statistical code due to its nature.

The present work represents the next step in this campaign, and is dedicated to a study of the influence of the isotopic composition of the projectile on the kinematical properties of projectile residues in peripheral and mid-peripheral relativistic heavy-ion collisions. To this goal, two symmetric systems  $^{112}\text{Sn}+^{112}\text{Sn}$  and  $^{124}\text{Sn}+^{124}\text{Sn}$  at the projectile energy of  $1\cdot A$  GeV have been studied.

In addition to the high-precision data on the longitudinal velocity of the projectile fragments, also the production cross-sections have been measured. In this work, theoretical calculations with the transport code BUU [Dan00, DB91] combined with an improved elaborate statistical multifragmentation code ABRABLA [GS91, KRS09], are shown to be capable of reproducing quantitatively the experimentally obtained results of the momenta of the final evaporated residues as a function of its mass in peripheral collisions of  $^{112}\text{Sn} + ^{112}\text{Sn}$  and  $^{124}\text{Sn} + ^{124}\text{Sn}$  at 1 GeV per nucleon. More over, constraints to the momentum dependence of the mean field and to the in-medium cross section are presented on the basis of the re-acceleration phenomenon in mid-peripheral collisions.

This work is ordered in the following way: chapter 2 introduces the experimental approach in these two experiments. A detailed survey of the detector calibration and of the analysis of the experimental data in order to obtain the desired observables is described in chapter 3. Experimentally obtained velocity distribution of the final residues, as well as the moments of this distribution and production cross-sections are presented in chapter 4. In chapter 5, a detailed discussion on the physics related to non-central heavy-ion collision is presented. Chapter 6 provides an interpretation of the measured data on the basis of abrasion-ablation model. In chapter 7, the performed calculations with microscopic hydrodynamical model are described, and a comparison to experimental data is given. Conclusion and outlook are found in chapter 8.

## Chapter 2

# The Experiment

In the previous chapter we came to a conclusion that, in spite of the experimental and theoretical efforts, there has been difficulty of explaining the momenta of the fragmentation residues. To extend the investigations, two systems:  $^{112}\text{Sn} + ^{112}\text{Sn}$  and  $^{124}\text{Sn} + ^{124}\text{Sn}$  at an incident beam energy of  $1\cdot A$  GeV, were studied in the present work. The systems were selected to explore the role of the isotopic composition of the projectile on the kinematical properties of the final residues in peripheral and mid-peripheral relativistic heavy-ion collisions over a broad range of final residue mass.

For this exploratory study the beams of stable nuclei have been chosen as their emittance is smaller than in case of secondary beams, while available intensities are higher. Since in both reactions the target and projectile are the same nuclei, the  $N/Z$  stays homogeneous for all possible impact parameters, despite the small effects coming from the neutron skin. This  $N/Z$  value is determined entirely by the corresponding tin nuclei in the system. The  $N/Z$  ratio of  $^{112}\text{Sn}$  is 1.24, and the one of  $^{124}\text{Sn}$  is 1.48, resulting, for a given  $Z$ , in the largest span in  $N/Z$  values for stable nuclei in this mass range.

A high-resolution magnetic spectrometer, the Fragment Separator (FRS) at GSI, Darmstadt was used to carry out this task. The incident energy is chosen to be very close to the maximum energy achievable with SIS18. Owing to the FRS design, the reaction products have the best conditions for the transmission through the device with energies around  $1\cdot A$  GeV.

In this chapter the experimental complex of GSI with the main focus on the beam delivery system and the Fragment Separator will be introduced. The principles of the high-precision momentum measurements and isotopic identification at the Fragment Separator will be described.

## 2.1 Accelerator facility at GSI

The beams were delivered from the universal linear accelerator (UNILAC) to the SIS18 heavy-ion synchrotron where they were extracted and guided through the target area to the FRagment Separator (FRS) spectrometer. The FRS was then used for the separation and analysis of the reaction products. A scheme of the present GSI accelerator facility is shown in Fig. 2.1, where on the left-hand side the transfer line from UNILAC can be seen, through which the pre-accelerated ions are injected into SIS. The extraction beam line is on the opposite side of the ring connecting the synchrotron to the FRS. The facility includes several experimental areas, which utilize the beam delivered by the accelerator system. The ions used as the beam particles can be generated and

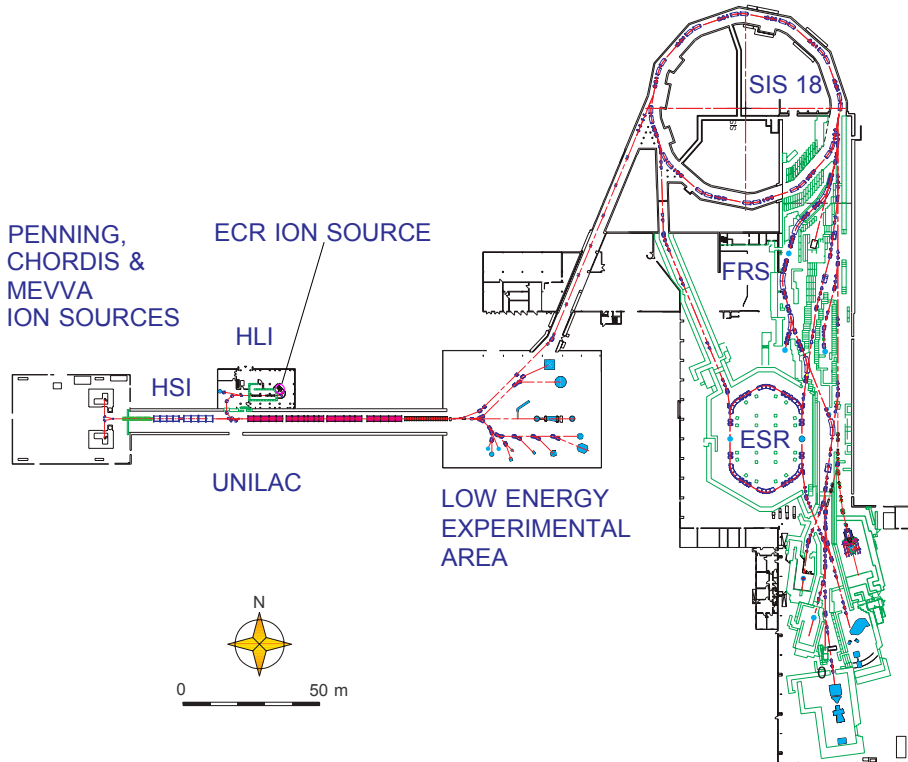


Figure 2.1: A schematic drawing of the GSI facility showing the linear accelerator (UNILAC), synchrotron (SIS), fragment separator (FRS), storage ring (ESR) and several experimental areas designed for different research purposes.

extracted from several ion sources [SBE<sup>+</sup>98]. The  $^{112}\text{Sn}$  ions used as beam particles in the first part of the experiment were generated in an Electron

Cyclotron Resonance ion source (ECR) located in the High Charge Injector (HLI) which injects the ions directly into the second stage of the UNILAC.  $^{124}\text{Sn}$  ions were generated in the Penning Ion Source (PIG) at the South injector, shown in the left side of the Fig. 2.1. The standard injection energy of the ions from UNILAC into the SIS18 is 11.4 A MeV. Both beam particles entered the SIS18 with the charge state +42. The charge state is achieved with a carbon foil stripper, which strips all but the eight innermost electrons off the beam ions, before entry into the SIS18.

### 2.1.1 The heavy-ion synchrotron SIS18

The synchrotron consists of 12 identical cells, each cell comprising two dipoles, a quadrupole triplet and diagnostic and correction elements. Among the latter are the chromaticity sextupoles, divided into two families of six and located in every other period close to horizontally focusing and horizontally defocusing quadrupoles to decouple the effects on the two planes [S<sup>+</sup>92]. The 12 cells are placed along a circumference of 216 meters. SIS18 can deliver any ion beam among all the stable nuclei ranging from hydrogen till uranium. The main beam energy achievable by SIS18 is determined by the maximum bending power of the magnets, which is 18 Tm. For various accelerated beams, this can mean different maximum energy, depending on the injected charge state and the  $N/Z$  ratio. The energy range for protons extends up to 4.7 GeV, while for uranium 73+ it extends to 1.4 GeV. The magnetic rigidity of  $^{124}\text{Sn}$  accelerated to 1.4 GeV with a charge state 42+ is 16.65 Tm and the one for the  $^{112}\text{Sn}$ , with same charge state, is 15.05 Tm.

Ions are accelerated by two radio-frequency structures, situated diametrically on the ring, opposite to each other. The passing ions are then accelerated during each revolution by means of a potential difference of 9 kV. With increasing velocity of the beam after each cycle, the frequency of the structure rises from 800 kHz to 5.6 MHz.

After achieving the energy of 1.4 GeV, the beam particles were extracted from the SIS18 and guided to FRS in spills with varying lengths from 3 s to 10 s. In order to keep the maximum counting rate allowed by the detector limits and the data acquisition system. The maximum beam intensity during the experiments was  $\sim 3 \cdot 10^8$  particles per spill for  $^{124}\text{Sn}$  and slightly lower for  $^{112}\text{Sn}$ .

### 2.1.2 The FRagment Separator

The Fragment Separator is a high-resolution zero-degree in-flight projectile fragment separator [G<sup>+</sup>92]. The FRS is designed for the study of heavy-ion

beams in the magnetic rigidities ranging from 5 Tm to 18 Tm, such that are provided by the SIS. Schematic view of the FRS magnets is presented in Fig. 2.2. The FRS consists of four similar magnetic groups that are each followed by an image plane (S1 - S4). The orbit length through the FRS dipoles results to  $\sim 70$  m. In this experiment FRS was operated in achromatic mode. The system is achromatic when its total dispersion is equal to zero, i.e. the deflection of particles does not depend on their momenta. In achromatic mode, FRS operates in two stages, that are separated with a central image plane S2. The first stage of the FRS i.e. the first two dipoles act as a dispersive element. The dispersion of the two dipoles in the second stage compensate that of the first stage, resulting the whole system to be achromatic from target till S4. The image planes S2 and S4 are both perpendicular to the initial beam direction  $z$ , which is referred as longitudinal direction or collision axis. The coordinate system is given in Fig. 2.2. Transversal directions  $x$  and  $y$  refer to horizontal and vertical directions respectively. Planes S1 and S3 after the first and third dipole are of the lesser interest because dipoles are designed to work as pairs. FRS operates in analogous way to optical achromatic lenses that bring two light waves with different wavelengths into focus in the same plane.

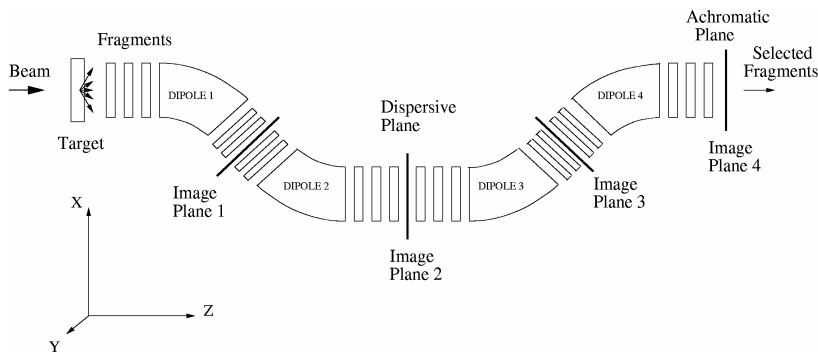


Figure 2.2: A schematic drawing characterizing the ion-optical elements of the FRS.

### Momentum acceptance of the FRS

The trajectories of the ions passing through the dipoles of each part are deflected according to the Lorentz force. Since the magnetic fields inside the dipoles are uniform and perpendicular to the trajectory of the ions, the field curves the flight-path of the ions. The action of the magnetic field upon the charged particle, with ionic charge  $q$  and momentum  $p$ , can be described by

the following equation:

$$B\rho = \frac{p}{q} = \frac{mv}{q} = \frac{m_0\gamma\beta c}{q} = \frac{u}{e} \frac{A}{Z} \beta\gamma c = 3.107 \frac{\beta\gamma A}{Z} [Tm], \quad (2.1)$$

where the product of magnetic field  $B$  and *effective radius* of the particle trajectory  $\rho$  is called the *magnetic rigidity*,  $v$  is the velocity of the ion,  $m = \gamma \cdot m_0$  ( $m_0$  = rest mass of the ion),  $m_0 = A \cdot u$  ( $u$  = atomic mass unit,  $A$  = mass number),  $\gamma = \sqrt{(1 - \beta^2)^{-1}}$ ,  $\beta = v/c$  (with  $c$  velocity of the light),  $q = Z \cdot e$  ( $Z$  = nuclear charge,  $-e$  = electron charge).

The trajectories of the ions in the magnetic fields are circular. In addition to dipole magnets, quadrupole doublets, at image planes S1 and S3, and triplets, at image planes S2 and S4 are used to focus the particles entering the dipoles with different angles. Hexapole magnets are used to correct chromatic aberrations and small steerers are used to deflect the beam in vertical direction. The term "magnetic setting", or simply "setting", refers to a FRS setup where the magnets are set with certain magnetic-field values. The setting thus determines the momentum acceptance of particles with a certain range of magnetic rigidities that are able to pass the FRS.

As stated earlier the first two dipoles act as dispersive elements, this means that two ions entering the FRS with different magnetic rigidities, but under the same angle, will pass through the S2 area (called the dispersive image plane) in different horizontal positions. Their displacement  $\Delta x$  is proportional to their relative difference in magnetic rigidity,  $\Delta B\rho/B\rho$ , through the quantity called *dispersion* defined as follows:

$$D_{S2} = \frac{\Delta x_{S2}}{\Delta B\rho/B\rho} \quad (2.2)$$

In our experiments  $D_{S2}$ , the dispersion at the image plane (S2), was measured to be 6.65 cm/% i.e. a relative difference of 1% in rigidity from that of the central trajectory rigidity will produce a 6.65 cm horizontal shift from the central position at S2. Thus, due to above mentioned ion optical and mechanical constrains of the FRS, if two ions differ in magnetic rigidities too much (i.e. more than 3%), they cannot be transmitted by the device at the same time, i.e. in the same magnetic setting.

When fragments pass through a layer of matter (i.e the scintillator and optionally degrader located at S2) they suffer a loss of energy according to the Bethe-Bloch equation:

$$\frac{dE}{dx} \approx f(v, I, Z_M) \cdot Z^2, \quad (2.3)$$

where  $Z$  and  $v$  are the nuclear charge and the velocity of the fragment,  $I$  and  $Z_M$  are the ionization potential and the nuclear charge of the medium, respectively. As a consequence of the suffered energy loss, every fragment will

reduce its velocity and consequently its magnetic rigidity according to its nuclear charge and velocity. From the FRS point of view this effect causes the magnetic rigidities of the fragments to span out even more and consequently the acceptance of the second part of the FRS will be even narrower compared to the first part. In some settings an additional degrader is added in between the two stages of FRS to make this effect even larger (i.e. decreasing the acceptance). This is beneficial when measuring fragments produced with low yields. In these settings one can increase the intensity of the beam without overloading the detectors at the exit of the FRS with fragments produced with higher counting rates and thus obtain a proper statistics for all the fragments. Fig. 2.3 illustrates the fragment selection criteria of the FRS, determined by one magnetic setting, with respect to the nuclear chart. If we assume that the velocities of the fragments do not differ much, then the magnetic rigidity is mostly governed by the mass-over-charge ratio of the fragments. In this case, the magnetic field of the first two dipoles, i.e. first state of the FRS, selects fragments within a certain range of mass-over-charge ratio. The field of the last two dipoles, i.e. the second state of the FRS, sets an additional condition (interval) on the nuclear charges that are selected from those that passed through the first state. In reality, with a large span in fragment velocities, the selected range in one magnetic setting is even a more restricted area in the nuclear chart.

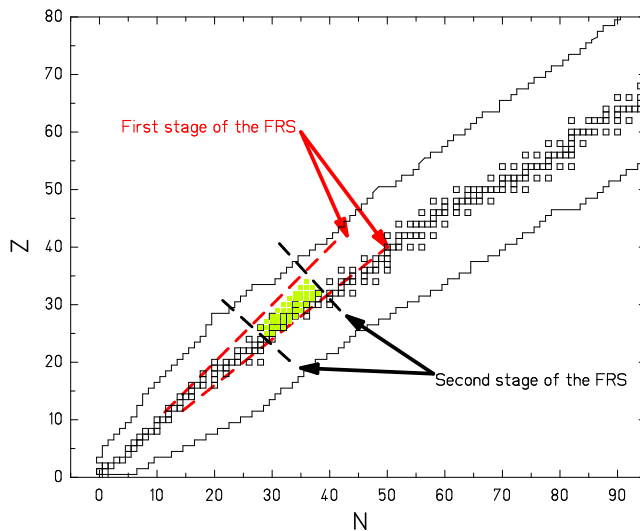


Figure 2.3: Fragment selection criteria of the FRS determined by one magnetic field setting in the first stage of the FRS (red dashed lines) and in the second stage of the FRS (black dashed lines) with respect to the nuclear chart.

To illustrate the momentum-resolving power of the FRS we derive, using equations 2.1 and 2.2, an expression for the relative momentum change:

$$\frac{\Delta p}{p} = \frac{\Delta x_{S2}}{D_{S2}}, \quad (2.4)$$

which shows that the momentum resolving power is governed only by the precision of the  $x$ -position measurement at S2. In other words, the momentum of a particle can be derived from the position at the dispersive image plane. However, in addition to the position resolution of the detectors, one needs to take in to account the momentum spread of the beam, the straggling in the different layers of matter and the beam spot size. Fig. 2.4 represents the horizontal and vertical position distributions of the beam at S2, measured by devoted beam-position detectors (see section 2.2.2). The FWHM of the beam spot in

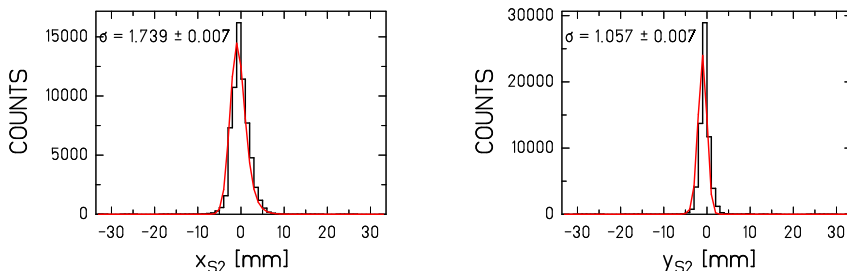


Figure 2.4: Measurements of the  $x$  and  $y$  position of the beam by Multiwire Proportional Counters at the dispersive image plane S2 during the initial calibration measurements.

transversal direction is  $\sim 4$  mm which will, according to Eq. 2.4, result into a momentum resolution of  $\frac{\Delta p}{p} = 6 \cdot 10^{-3}$  when a nominal value of 6.65 cm/% for dispersion is used. This is the feature of the FRS which gives the high-precision nature to these experiments. In chapter 3 it will be shown in detail what is needed to be done in order to measure the momenta of all particles exploiting the transversal position at S2.

### Angular acceptance of the FRS

Fragments satisfying a certain combination of mass  $A$ , nuclear charge  $Z$  and velocity  $v$ , can enter the FRS and travel through the vacuum tube to the final image plane S4, being deflected by the magnetic fields. Ions not satisfying the conditions hit the walls of the vacuum tube and are stopped in the matter of the magnets or in the dedicated slits and collimators.

The limitation for the fragments velocity vector,  $v$ , due to specific geometrical and ion-optical characteristics, is set by the angular acceptance of the FRS. The maximum angle of the fragments velocity vector to be accepted by the apparatus is 15 mrad with respect to the beam axis. Due to the high momenta most of the projectile-like fragments, produced in a collision with a target nucleus, escape the target in forward direction within the 15 mrad cone. However, a larger angular emittance may originate from certain reaction processes, leading to losses of the transmitted fragments, which must then be properly accounted for. In chapter 3 it will be discussed in detail how the limited angular acceptance of the FRS is handled.

## 2.2 Experimental setup

Both tin beams were delivered by the SIS and focused on their production targets located in the front of the first FRS dipole. The kinetic energy of the beam was 1 GeV per nucleon prior to the collision. In Fig. 2.5 the experimental setup is shown with all the detectors used in the experiment. In addition to the FRS detectors, the signal from the beam-current transformer (TRAFO) [HR01] used for the SIS beam monitoring, was used to get the information of the total flux of the beam particles i.e. the number of ions impinging on the target. This is essential information in order to get a normalization for the yields of the measured fragments. TRAFO signal was calibrated using the standard FRS beam monitor, SEETRAM (Secondary Electron TRANSMISSION Monitor) [JCG<sup>+</sup>96, JSB02]. Since TRAFO introduces no matter on beam line, it does not disturb the quality of the beam before it hits the target neither it contributes to the overall fragment production by nuclear interactions of the beam particles with the detectors material itself.

The scintillation detectors were used to acquire the horizontal position of the passing ions and to register the start and the stop time signals for the time-of-flight (*ToF*) measurement. One scintillation detector (SCI21) was placed at the end of the first stage – at the image plane S2 – and another (SCI41) at the end of the second stage – at the final image plane S4. At S4 fragments are also detected by two MUSIC detectors (MUSIC41 and MUSIC42) for the energy loss and horizontal position information. Position information was deduced from the drift time measurements of both MUSIC detectors. With the two position measurements provided by the MUSICS, it was possible to determine the angle of the ions path and to eventually calculate the length of the flight path. In the following sections a detailed description of each detector and its purpose in the experiment is given.

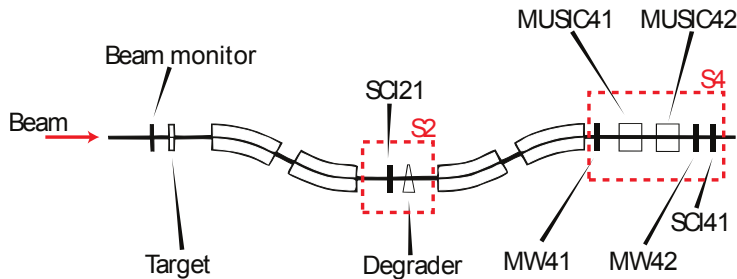


Figure 2.5: Schematic view of the Fragment Separator (FRS) and the associated detector equipment used in this experiment. The notation of different detectors is explained in the text. More technical drawings with accurate detector positions can be found in Appendix B.

### 2.2.1 The Hall probes

The magnetic field inside the dipoles is continuously measured by the Hall probes. They measure the potential difference (Hall voltage) between the two ends of a conductor, through which an electric current is flowing. Magnetic field inflicts a Lorentz force to the charge carriers pushing them to one side of the conductor, producing a measurable voltage between the two sides of the conductor. The magnetic field strength can then be deduced by measuring simultaneously the values of the applied current and the obtained voltage. Since this can be done fairly accurately, the Hall probes are able to return the values of the magnetic field with a relative uncertainty of  $\sim 10^{-4}$ . Although the response of the Hall probes was found to be stable within the experiment, their response can show a long-term drift due to radiation damages. Therefore, they have to be calibrated for each experiment. The calibration of the Hall probes will be discussed in section 3.1.2.

### 2.2.2 Multiwire proportional chambers

During calibration all together six multiwire proportional counters (MWPCs) [Ste91] can be inserted at different positions in the beam line to monitor the position of the passing particles. They are mounted in pockets which can be easily moved in and out of the vacuum tube by air pressure during the experiment. Two of these detectors, MW21 and MW22, are mounted in front of and behind the image plane S2 and other two, MW41 and MW42, are mounted in front of and behind the image plane S4. MW11 and MW31 are mounted at the intermediate image planes S1 and S3. MWPCs are part of the FRS standard detector family used for beam centering and for calibration of

other position sensitive detectors. MWPCs were calibrated by placing thick metal slits with well know horizontal position just before the detector. When particles are blocked by the slits, their physical borders will be seen in the spectra giving the position information. MWPCs are usually not used during data measurements, because they would deteriorate the ion-optical resolution of the FRS due to inhomogeneous matter distribution. Multiwire detectors at S4 (MW41 and MW42) were kept on the beam line throughout the experiments because they were placed after the last magnetic element and therefore would not cause deterioration.

### 2.2.3 Plastic scintillators

The two plastic scintillation detectors, SCI21 and SCI41, were positioned at the dispersive image plane S2 and at the achromatic image plane S4, respectively. The scintillators were produced from a Bicron BC 420 (polyvinyltoluene, 61% Anthracene) plastic material, characterized by a high efficiency of light production, low self-absorption and by a very fast signal rise time ( $\approx 0.5$  ns). The size of the used plastic plates in both scintillators was  $220 \times 45$  mm<sup>2</sup> with a sensitive area of  $195 \times 40$  mm<sup>2</sup>. The nominal thickness of both plates was 2.8 mm. There are two fast Hamamatsu HM2431 photomultipliers mounted on each scintillator, on the left and right side with respect to the axis of the FRS, reading the light signals.

Scintillators were used to determine the horizontal position at image planes S2 and S4 individually, and together they provided the time-of-flight of the ions passing them. With the knowledge of the horizontal positions at S2 and S4 and the strength of the applied magnetic field, it is possible to determine the trajectories of the fragments, which combined with the information on the velocity and charge state of the fragment leads to the determination of the fragments mass.

The time-of-flight ( $ToF$ ) is the difference of the times at which the ion passes through SCI41 (at the time  $t_{S4}$ ) and through SCI21 (at the time  $t_{S2}$ ). Since SCI41 provided the master-trigger for the whole data acquisition system, a time delay,  $\Delta t$ , was added to the SCI21 signal to come after the master trigger ( $t_{S2} + \Delta t > t_{S4}$ ). The delayed SCI21 signal was then used to stop the acquisition. By using this method the dead-time of the data acquisition was reduced considerably compared to the case were the master trigger would have been taken from the first scintillator.

The principle of the scintillator signal treatment is illustrated schematically in Fig. 2.6. The signals coming from the photomultipliers are first treated with the constant-fraction discriminators (CFD) from where they enter the time-to-amplitude converter (TAC) to be used as a start and stop signal. The

analog signal of the TAC's was then read and digitized by the analog-to-digital converter (ADC). The threshold of the CFD's was set to  $\sim 10$  mV in order to discriminate the noise and light particles.

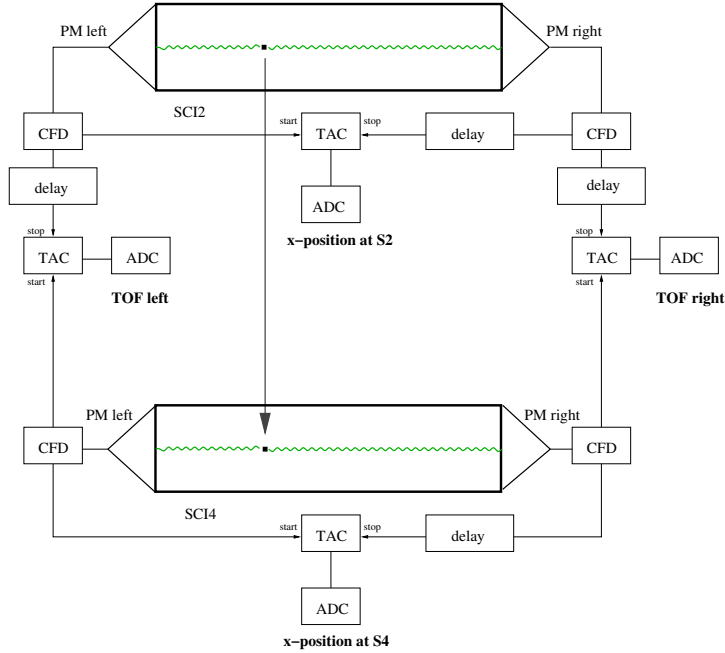


Figure 2.6: A schematic diagram of the treatment of the signals from two scintillators used in the experiment for measuring the  $x$ -positions at S2 and at S4 and of the time-of-flight of the fragment. Photomultiplier's (PM) signals pass by constant-fraction discriminators to impose a lower threshold and to eliminate the pulse-height dependence of the timing signal. The ADC signals are recorded to the DAQ.

The measured time-of-flight ( $ToF^*$ ) was taken as an average of the left and right signals,  $ToF_L^*$  and  $ToF_R^*$ , that were transformed from channels to nanoseconds through the calibration factors  $\alpha_L$  and  $\alpha_R$  so that:

$$ToF^* = \frac{ToF_L^* \cdot \alpha_L + ToF_R^* \cdot \alpha_R}{2} = t_{S2} + \Delta t - t_{S4}. \quad (2.5)$$

By taking the average value the influence of the ions positions and the lights propagation time inside the scintillator to the time-of-flight is eliminated. The actual time-of-flight ( $ToF$ ), which corresponds to the ratio of flight-path  $s_0$  and the fragment velocity  $v$ , was obtained by subtracting the measured time-

of-flight ( $ToF^*$ ) from the time delay:

$$ToF = \Delta t - ToF^* = t_{S4} - t_{S2} = \frac{s_0}{v}. \quad (2.6)$$

Precise calibration of these detectors was especially important for the determination of the fragment velocities and for their identification. The calibration of position and time-of-flight signals as well as the recovery of the position shift of the lightest residues due to the so called "walk effect" of the CFD's will be discussed in chapter 3.

### 2.2.4 Multi-Sampling Ionization Chambers

At the end of the second stage the ions were detected by two multiple-sampling ionization chambers (MUSICs) [PGM<sup>+</sup>94]. The MUSICs provided the energy-loss signals which were used to obtain the information on nuclear charge  $Z$ . Owing to their high velocity, the fragments were completely stripped of electrons with a probability higher than 99% [SGF<sup>+</sup>91], so that the ionic charge of the passing ion,  $q$ , also determines the nuclear charge of the fragment ( $q = Ze$ ). Drift-time signals from the two MUSIC detectors also provided information on the horizontal position and the horizontal angle of the passing ions trajectory. This information was used to determine the length of the ions path between the scintillators which then allowed the determination of the velocity together with the  $ToF$  information.

MUSIC is an ionization chamber filled with P10 gas which consist of 90% Ar and of 10% CH<sub>4</sub> at about room temperature and normal pressure. When an ionizing particle penetrates through the gas, a cloud of electrons and ions is produced. By means of an applied electric field the charged particles drift towards the cathode (positive ions) and to the six-fold segmented anode (electrons). Entrance and exit windows were made of 25  $\mu\text{m}$  Kapton foil covered by an aluminum layer of 40  $\mu\text{g}/\text{cm}^2$ . The active volume of the detector has cross-section of 20 x 20  $\text{cm}^2$  and a length of 40 cm corresponding to a thickness of 60  $\text{mg}/\text{cm}^2$  Ar. A schematic view from the top of the MUSIC ionization chamber used in the experiment is given in Fig. 2.7.

Anodes are shielded by a Frisch grid which is maintained at an intermediate potential between the cathode and the anode. The grid is made to be as transparent as possible to electrons which are initially drawn from the interaction volume toward the grid. The purpose of the grid is to prevent the drift of the ions and electrons causing a signal while they travel in the interaction volume. Signal is only registered during the electrons passage from Frisch grid to the anode.

Using charge sensitive preamplifiers, the charge of the electron cloud arriving

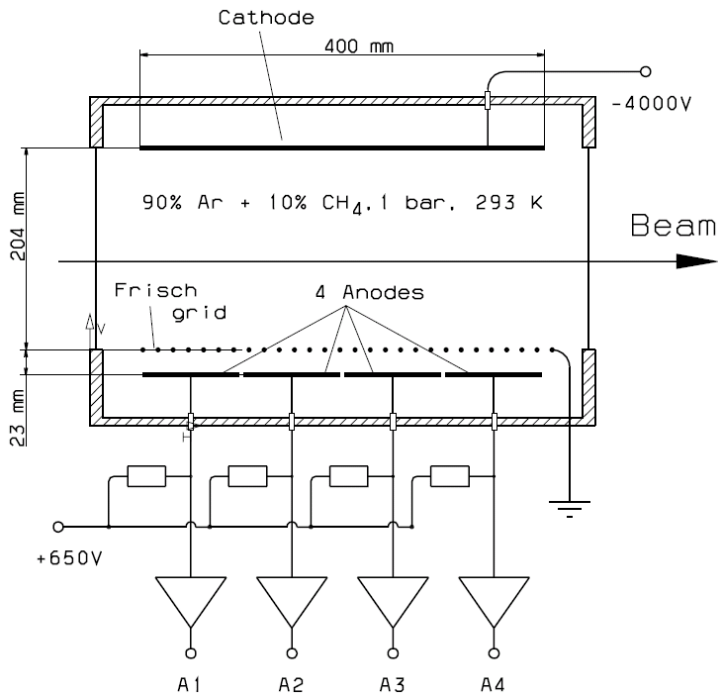


Figure 2.7: A schematic view of the parallel-plate ionization chamber used in the experiment.

at each anode is converted into voltage which is proportional to the number of electrons. Since the number of generated electrons is roughly proportional to the square of the charge of the penetrating particle, the output voltage of the preamplifier is a measure for the nuclear charge of this particle. The preamplifier output signal is amplified and shaped by the main amplifier and digitized by an ADC and further on handled by the data-acquisition system. From six available anodes only the signals of the middle four anodes are used. The first and the last anode serve for homogeneity of the electric field and are only connected to the high voltage. Using an additional fast detector as a start trigger for a TAC, the drift time of the electron cloud provides information of the  $x$ -position of the passing particle. The stop signal for the TAC is derived

from the energy signal of each anode. The calibration of the energy losses will be discussed in section 3.1.5.

Since the amplitude of the energy signal also depends on the atomic density of the gas, which may vary with temperature and pressure of the surroundings, sensors are installed inside MUSIC in order to monitor those parameters.

# Chapter 3

## Data analysis

The aim of this chapter is to describe the necessary procedures to obtain the longitudinal velocities of the fully recognized fragmentation residues and determine their production cross-sections in the reactions  $^{112}\text{Sn} + ^{112}\text{Sn}$  and  $^{124}\text{Sn} + ^{124}\text{Sn}$  at 1.4 GeV. In the first section of this chapter (3.1) the calibration of the used detectors is described. The second section (3.2) will describe all the procedures of the data analysis leading to the identification and determination of the velocity distributions of the fragmentation residues. In the third section (3.3) the procedure to evaluate the formation cross-sections of the measured fragmentation residues will be described. The fourth section (3.4) will be dedicated to the error analysis.

### 3.1 Calibrations

Although the reactions  $^{124}\text{Sn} + ^{124}\text{Sn}$  and  $^{112}\text{Sn} + ^{112}\text{Sn}$  are referred as being separate experiments, they were performed one after the other in a five days period,  $^{124}\text{Sn} + ^{124}\text{Sn}$  being the first. Many of the initial calibrations needed to be performed only in the beginning of the first experiment since many of the detectors at the FRS have no dependence on the utilized target nor on the beam that is used. One exception was in the case of MUSIC detectors where the calibration did depend on the nuclear charge of the beam particles, but since both beams had the same nuclear charge ( $Z=50$ ), only one calibration was needed.

### 3.1.1 Calibration of beam monitor

To be able to determine the particle production cross-sections, as well as the correct normalization factors for combining measured data from settings with various beam intensities, the beam particle flux at the target has to be known at all times.

Usually a standard FRS beam monitor, SEETRAM (Secondary Electron TRANsmission Monitor) [JCG<sup>+</sup>96, JSB02] is used for this purpose. Although SEETRAM has only thin foils, its presence is not desired during precise data measurements because of the slowing down of the ions and because it may act as an additional target causing nuclear reactions. To overcome this problem one normally has to estimate a correction for this effect or by making two consecutive measurements, one with SEETRAM and one without.

In this experiment a different method was used. The normalization to the primary-beam intensity was done by counting the number of the incoming beam particles using the signal from the beam-current transformer (TRAFO) [HR01] used for the SIS beam monitoring. The advantage of using the TRAFO instead of SEETRAM is the fact that there is no layer of matter introduced to the beam line. Another advantage is that TRAFO signal is not as sensitive to changes due to the long-term irradiation. However the SEETRAM output served as an intermediate information to connect the absolute calibration with the scintillator to the TRAFO output. SEETRAM measures the electron current as a function of the number of incident beam particles which was measured with a scintillation detector during the calibration run. Due to the saturation of the scintillation detector output at large particle fluxes the calibration was made up to the particle rate in the order of  $\sim 10^5$  particles per second which is still manageable by the scintillators. The calibration data and a quadratic fit are presented in Fig. 3.1. Since SEETRAM itself does not suffer any sizable saturation at these particle rates, the linear term of the quadratic fit where taken as the calibration factor to compensate the scintillator saturation. TRAFO could not measure the low intensity particle flux used in the SEETRAM calibration, so TRAFO was calibrated with higher beam intensity against the calibrated SEETRAM output. The linear calibration fit of TRAFO is presented in Fig. 3.2.

### 3.1.2 Determination of the parameters for magnetic deflection

As introduced in the Eq. 2.1 in chapter 2, the magnetic rigidity  $B\rho$  is determined by the radius  $\rho$  of the fragment trajectory in a magnetic field of given strength  $B$ . The strength of the magnetic field was measured by the Hall probes

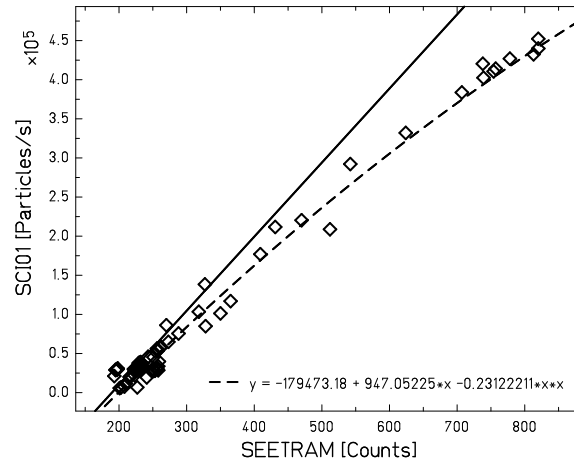


Figure 3.1: Determination of the calibration factor of SEETRAM output. Dashed line shows the quadratic calibration curve fitted to the data showing scintillator counts versus the SEETRAM output. Solid line shows the linear part of the fit.

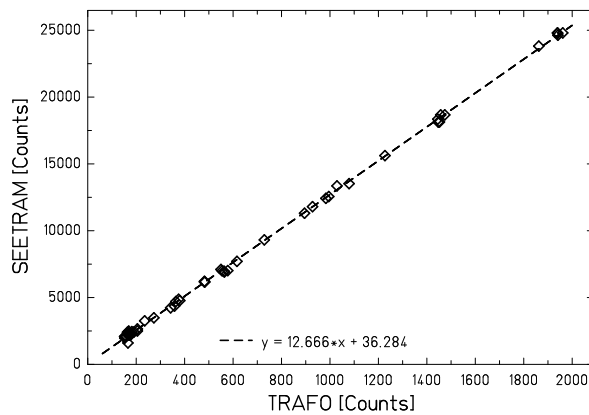


Figure 3.2: Determination of the calibration factor for TRAFO counts. Dashed line represents the linear calibration fit to the data showing the SEETRAM output versus the TRAFO output.

as described in section 2.2.1. There was no need to perform an absolute calibration for the Hall probes since only the product  $B\rho$  enters into the analysis. Instead, the determination of the so called effective radius of the dipoles was performed with the primary beam, which has a well known magnetic rigidity given by the revolution frequency of the SIS accelerator. When the beam was horizontally centered according to MW22 and MW42 detectors, the effective radii for both stages of the FRS was determined by requiring that the product with the magnetic field strength given by the Hall probes was equal to the magnetic rigidity of the beam, i.e.:

$$\begin{aligned}\rho_{S2}^{\text{eff}} &= \frac{(B\rho)_{\text{Beam}}}{B_{12}} \\ \rho_{S4}^{\text{eff}} &= \frac{(B\rho)_{\text{Beam}}}{B_{34}},\end{aligned}\tag{3.1}$$

where  $B_{12}$  is the average value of the magnetic fields measured by the Hall probes of the first and the second dipole. Likewise  $B_{34}$  represents the average value given by the third and fourth Hall probes located in the second state of the FRS. This is reasonable since by the operating principle of the FRS in the achromatic mode, the magnets operate as pairs with identical magnet fields. In this way, the determination of the effective radii included the calibration of the Hall probes.

To determine the magnetic rigidity for fragments with unknown energy we can exploit the information of ions horizontal position according to the dispersion introduced in Eq. 2.2. The so called dispersion relation for the first and the second part of the FRS are thus given by the equations:

$$\begin{aligned}(B\rho)_{S2} &= B_{12}\rho_{S2}^{\text{eff}}\left(1 + \frac{x_{S2}}{D_{S2}}\right) \\ (B\rho)_{S4} &= B_{34}\rho_{S4}^{\text{eff}}\left(1 + \frac{x_{S4}}{D_{S4}}\right),\end{aligned}\tag{3.2}$$

where  $x_{S2}$  and  $x_{S4}$  are the fragment positions at S2 and S4 respectively and  $D_{S2}$  and  $D_{S4}$  are the dispersions of the first and the second part of FRS respectively. The obtained resolution for the measured magnetic rigidity in these experiments was about  $5 \cdot 10^{-4}$ .

The determination of the values for dispersions was done with the  $^{124}\text{Sn}$  beam which was known to have a magnetic rigidity of  $(B\rho)_{\text{Beam}} = 13.9966 \text{ Tm}$ , when fully stripped i.e. with charge state +50. After centering the beam throughout the FRS, the magnetic fields of the dipoles were changed by small steps (0.3 %) while measuring the position of the beam for each magnetic setting with scintillators SCI21 and SCI41. Since the bending power of the dipoles is changed and the magnetic rigidity of the beam remains unchanged, we see a horizontal shift in the position of the beam. After measuring the beam positions in different settings the dispersion could be deduced by requiring that

the beam has the same magnetic rigidity in every setting. For example when the beams position at S2 is measured in two different settings i.e. in two different magnetic fields ( $B_{12}$  and  $B'_{12}$ ), one obtains from Eq. 3.2 the following relation:

$$B_{12}\left(1 + \frac{x_{S2}}{D_{S2}}\right) = B'_{12}\left(1 + \frac{x'_{S2}}{D_{S2}}\right). \quad (3.3)$$

The results of the measurement of the dispersion at S2 is presented in Fig. 3.3. The plotted data represents the beam position as function of relative change of magnetic field with respect to  $B_{12}^0$ , which is the magnetic field when beam is in central trajectory. Beam positions represents the centroids of the Gaussian functions that were fitted to the beam position data obtained from scintillator SCI21. The calibration of the scintillators is presented in the next section. The dispersion of the first stage of the FRS could be determined from the slope of the linear fit made to the data points:

$$D_{S2} = \frac{\Delta x_{S2}}{\Delta B_{12}/B_{12}^0} = 6.65 \pm 0.02 \text{ cm}/\%. \quad (3.4)$$

A similar procedure was used to determine the dispersion of the second stage of the FRS:

$$D_{S4} = \frac{\Delta x_{S4}}{\Delta B_{34}/B_{34}^0} = -7.64 \pm 0.02 \text{ cm}/\%. \quad (3.5)$$

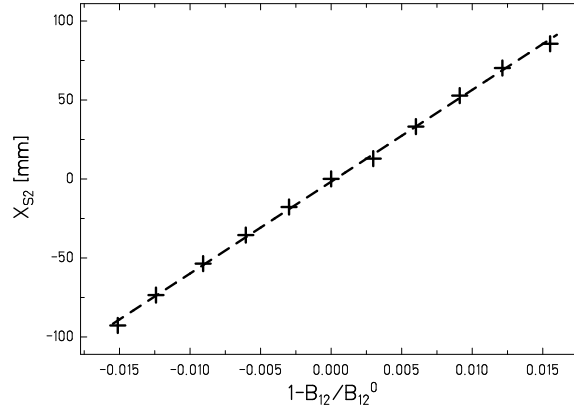


Figure 3.3: Measurement of the dispersion at S2 and a linear fit of the measured values. Slope of the fit determines the dispersion.

### 3.1.3 Calibration of the scintillators

Before the scintillator output could be calibrated it was first necessary to look at the working principle of the constant fraction discriminators (CFD), which were used to discriminate the output signals from the left and right side of the scintillator's photomultipliers.

Use of the CFD has the advantage over the normal leading edge discriminator that the timing does not depend on the input pulse amplitude like in the "normal" leading edge discriminator that produces a logic output pulses at the time when the input pulse crosses a given threshold voltage. If the amplitude is changed, but the rise time of the input pulse remains the same, then a larger pulse will cross the threshold at an earlier time than a lower pulse. Thus, the timing of the output pulse is shifted by this change in amplitude. This so called "time walk" can be avoided with the use of CFD's.

CFD produces output signal that is relative to the input signal. If the cable delay is too short, the unit will work as a normal discriminator for signals with a low amplitude because then the output of the normal discriminator fires later than the CFD part. This can happen when the particle passing the scintillator has small charge state. As a consequence the SCI21 response becomes sensitive to the charge state of the passing fragment. In the left side of Fig. 3.4 scintillator output is shown for different energy losses measured by the MUSIC before any corrections were made. First of all one can see the physical borders of the sensitive area of the scintillator plastic which are known to be from -100 mm to 100 mm. One can see that the signals from lightest residues are suffering a shift due to the walk of the CFD's. The failure could be recovered by applying a correction factor in a way that the borders are seen at the same channels for all measured energy losses. The corrected signal can be seen in panel (b) in Fig. 3.4.

After the signal from the scintillator was corrected for the CFD-walk, its position calibration could be performed. The measurement for the determination of the dispersion (3.3) was also used for the position calibration of scintillator SCI21 since the full sensitive range was populated during the measurement. The position calibration was performed with the detector MW21 which was inserted to the beam line right before the scintillator SCI21 (see Appendix B). Fig. 3.5 displays the data used for the calibration of the scintillator SCI21 performed with the MW21. Figure also shows the fitted, third degree polynomial, calibration curve. The resolution of the position determination of the scintillators was determined to be 3 mm (FWHM).

Thin plastic scintillators are vulnerable to radiation damages and therefore the performance of the SCI21 scintillator had to be monitored during the course of the experiment to assure that the detector response had not changed. Radiation

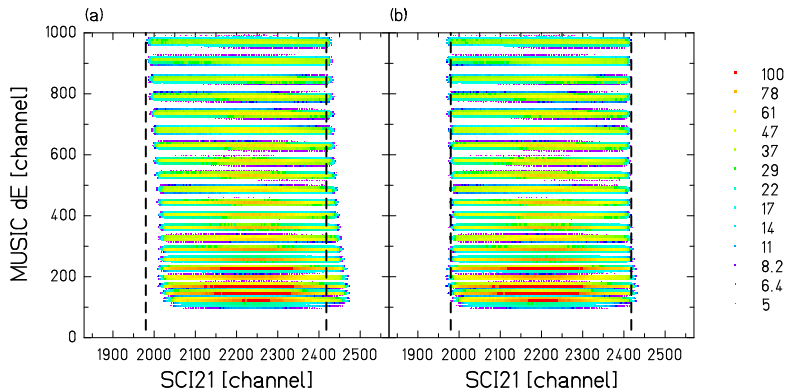


Figure 3.4: (a) 2-dimensional plot showing the uncorrected scintillator signal versus the energy loss measured by the MUSIC detectors. (b) Same plot after the correction for the walk of the CFD-units. The effect of the correction is seen especially for the lower energy loss signals corresponding to ion charge states from 10 to 28. The dashed lines corresponds to the physical borders of the scintillator plane. The color scale representing the bin count is logarithmic.

damages may appear when the scintillator is directly hit by a beam of high intensity. When ever necessary, the scintillator was protected with slits (see Appendix B) from the primary beam which could have damaged it.

### 3.1.4 Time-of-flight calibration

The time-of-flight ( $ToF$ ) of the fragments is the time interval taken by a fragment to travel from the central dispersive plane to the final achromatic image plane. Scintillators located in before mentioned locations are used to provide the start and stop signals for the  $ToF$  measurement. Signals from scintillators are first processed by the time-analog-converters (TAC). The analog signal is then digitized by the amplitude-to-digital converter (ADC) and finally processed by the data acquisition (DAQ). The output of the ADC's first needed to be calibrated in order to be able to tell relation between channels and real time. This was done using a pulse generator, which provided signals with a time period of 10 ns. In Fig. 3.6 the pulse generator signals for the left and right sides of the SCI21 and SCI41 are presented. The full time range of the TAC was adjusted to be  $\sim 80$  ns which was large enough to cover the fragments velocities over a broad range.

The  $ToF$  delay and the effective flight-path are determined by passing the beam through the FRS with different kinetic energies (i.e. with different velocities)

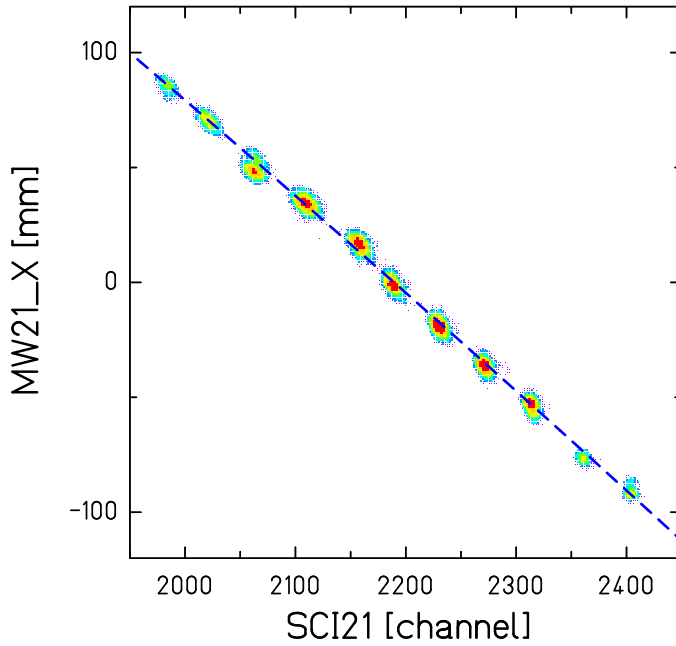


Figure 3.5: Position information of MW21 plotted against the SCI21 data during the measurements used for dispersion determination as described in section 3.1.2. The fitted curve represent the obtained calibration curve of the SCI21.

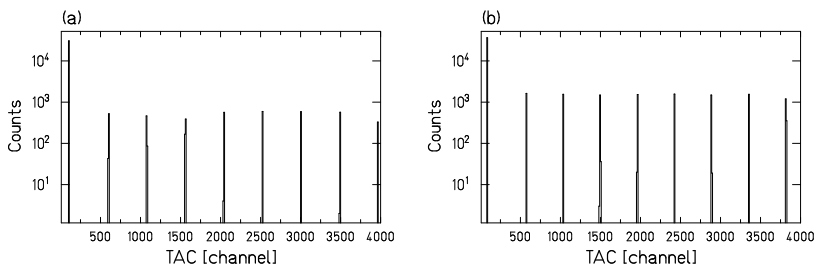


Figure 3.6: Calibration of the TAC units with a pulse generator for the *ToF* measurements: (a) signals from the left sides of the scintillators SCI21 and SCI41. (b) signals from the right sides of the scintillators SCI21 and SCI41. The distance between two peaks corresponds to a time of 10 ns.

and measuring the corresponding  $ToF$ . For this measurement the primary beam was attenuated with 4 different layers of material with different thicknesses. The materials and corresponding results of the measurements are summarized in Tab. 3.1. By calculating the velocity,  $v$ , of the beam after passing through the various layers of matter at S2 using the code AMADEUS [Sch], and by measuring the  $ToF^*$  (Eq. 2.5), one could establish following dependence of  $1/v$ :

$$\frac{1}{v} = \frac{ToF}{s_0} = \frac{\Delta t - ToF^*}{s_0} = \frac{\Delta t}{s_0} - \frac{ToF^*}{s_0} = A + B \cdot ToF^*, \quad (3.6)$$

where  $A = \Delta t/s_0$  and  $B = -1/s_0$ , and  $ToF^*$  is the time provided by the calibration of TAC, as defined in Eq. 2.5. The results of the measured  $ToF_L^*$

material(s)	Thickness [mg·cm <sup>-2</sup> ]	1/v [ns/cm]	$ToF_L^*$ [ns]	$ToF_R^*$ [ns]
Be + degrader	6347 + (737.1 ± 0.1)	0.041041	30.4811	37.9729
Al + degrader	1022 + (737.1 ± 0.1)	0.038700	39.0565	46.5211
<sup>112</sup> Sn	126 ± 0.1	0.038229	40.7676	48.2886
<sup>124</sup> Sn + degrader	142 + (737.1 ± 0.1)	0.038396	39.9555	47.8275

Table 3.1: Summary of time-of-flight calibration measurement.

and  $ToF_R^*$  and the corresponding calculated beam velocities are illustrated in Fig. 3.7. From the linear fits to the left and right side time-of-flights one obtains average values for the  $ToF$  offset,  $\Delta t = 184.2 \pm 0.5$  ns, and for the flight-path,  $s_0 = 36.5 \pm 0.1$  m.

### 3.1.5 Corrections of the energy-loss signals

To measure the nuclear charges of the produced fragments, the two Multi-Sampling Ionization Chambers located in the final focal plane were used as described in section 2.2.4. In order to obtain the nuclear charge of the residue with a high resolution, several corrections must be applied to the measured energy loss signal. Strength of the registered signal tells the magnitude of the energy loss of the initial ionizing particle according to the formula 2.3. It can be seen that the energy loss of the residue is inversely proportional to the square of its velocity. This causes a broadening of the peaks in the energy-loss spectra since particles with same nuclear charge may have different velocities. In order to improve the nuclear charge resolution, a correction was performed with the use of the AMADEUS program [Sch], which calculates the energy loss of a given residue. For the calculation, a reference velocity of ions corresponding to the energy of 1·A GeV was selected to obtain a correction function  $f(v)$ . The velocity-corrected energy loss is then calculated as:

$$\Delta E_{v-corr} = \Delta E_{meas} \cdot f(v). \quad (3.7)$$

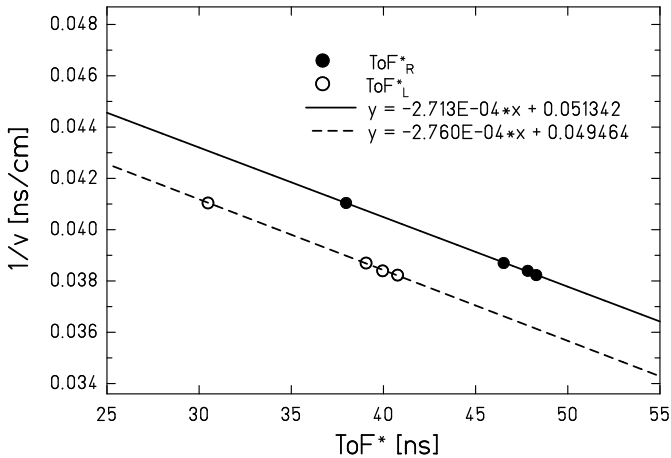


Figure 3.7: Time-of-flight calibration: Lines are linear fits of the measured values. Fits define the time delay  $\Delta t$  and the total flight path  $s_0$  according to the equation 3.6.

Additionally energy loss signals needed to be corrected for the distance of the ions track from the anode, i.e. the  $x_{S4}$  position. This arises from the fact that electrons produced along the track of the charged fragment may undergo subsequent recombination during their drift towards the anodes. This leads to a weaker signal compared to an electron cloud produced by the same ion passing by the anodes in closer horizontal distance. The electron recombination follows an absorption law, which means that the amount of recombined electrons have an exponential dependence on the distance of the fragment from the anodes. The dependence of the energy-loss signal on the fragment position in the MUSIC may thus be described by an exponential function. The position-correction was applied to the velocity-corrected energy-loss signal in the following way:

$$\Delta E_{corr} = \Delta E_{v-corr} \cdot \frac{1}{e^{(-\lambda x_{s4})}}, \quad (3.8)$$

where the absorption coefficient  $\lambda$  was determined by fitting the measured energy loss as a function of the horizontal position. The value of  $\lambda$  was determined for each value of energy loss signal separately to be  $(6 \pm 2) \cdot 10^{-4} \text{ mm}^{-1}$ . This corresponds to a rather large variation of signal strength over the range of 200 mm and improves the nuclear charge resolution considerably. Fig. 3.8 displays the nuclear charge resolution determined from the average energy loss in the MUSIC detectors before and after the corrections. The obtained final nuclear charge resolution was determined to be  $\Delta Z = 0.4$  units (FWHM). Velocity and

position corrections could have been applied also in reverse order i.e. the order of executions does not influence the final result.

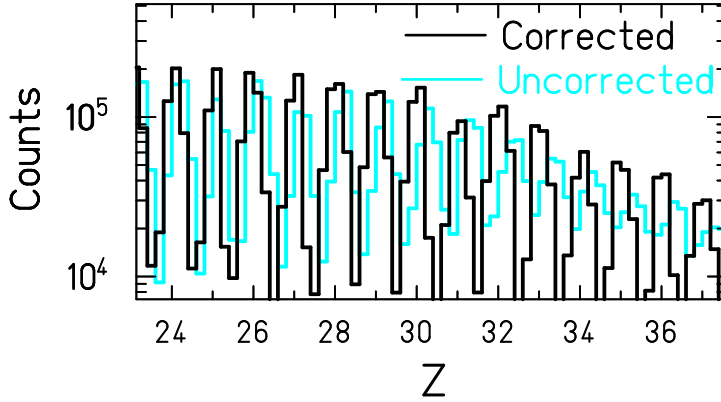


Figure 3.8: Nuclear charge resolution determined from the average energy loss in the MUSIC detectors before (light blue) and after the correction for the position at S4 and for the velocity of the passing fragments (black).

### 3.1.6 Mass and nuclear charge identification

The complete isotopic identification is achieved by measuring both the nuclear charge, and the mass-over-charge ratio of each nucleus. The measurement is done in-flight in a time less than 300 ns, allowing to observe the primary production prior to beta-decay or any other radioactive decay.

The ionic charge state of the passing ion were obtained from the energy loss in the two ionization chambers (MUSICs) as described in previous section. Nuclear charge,  $Z$ , can be determined from the ionic charge if the charge state of the ion is zero, which is the case of  $^{112,124}\text{Sn}$  at 1-A GeV [SBA<sup>+</sup>98]. The resolution of the used MUSICs allows nuclear charge separation sharply approximately in the range from  $Z=5$  to  $Z=95$ .

The mass-over-charge ratio of the residues is determined on the basis of magnetic rigidity and time-of-flight measurements. The magnetic rigidity of ions is obtained from their deflection in the magnetic fields while passing through FRS. The deflection is determined by position measurements at two stages of FRS as described earlier in section 3.1.2.

According to the formula 2.1 the mass-over-charge ratio of a fragment can be

written:

$$\frac{A}{Z} = \frac{1}{c} \cdot \frac{e}{m_0 + \delta m} \cdot \frac{(B\rho)_{S4}}{\beta\gamma(TOF)}, \quad (3.9)$$

where  $(B\rho)_{S4}$  is the magnetic rigidity of a particle,  $c$  is the velocity of light,  $e$  the elementary charge,  $m_0$  the nuclear mass unit,  $\delta m = dM/A$  the mass excess per nucleon. For the calculation of the mass excess a generalized empirical mass formula [MS66] was used, which provided sufficient accuracy for the  $A/Z$  calculation. It is then enough to measure its magnetic rigidity,  $(B\rho)_{S4}$ , and its velocity from the time-of-flight. The magnetic rigidity,  $(B\rho)_{S4}$ , of the second part of the FRS is used since the time-of-flight is measured in the second half of the spectrometer.

To improve the identification plot one still needs to do few corrections for the flight path of the fragments. The fragment can acquire transversal momentum in a nuclear reaction, or caused by the straggling in the scintillator SCI21, and enter the second stage of the FRS with an angle  $\alpha_x$ . Correction is needed because length of the fragments flight path depends on its entering angle. Flight path also depends on the horizontal position at S2: fragments with different rigidities than the one corresponding to the central trajectory enter the second section at different S2-position and thus follow a different path along the FRS. In Fig. 3.9 the effect of the angle correction to  $A/Z$  ratio is shown.

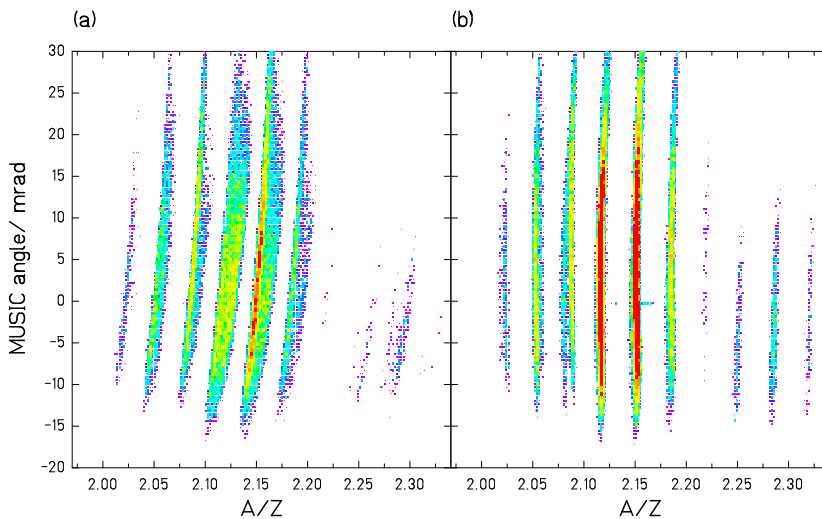


Figure 3.9: Angle of the fragments flight path through the FRS measured with the MUSIC detectors plotted as a function of the  $A/Z$  ratio: (a) before the angle correction and (b) after the angle correction. Data was measured during the experiment  $^{124}\text{Sn} + ^{124}\text{Sn}$ .

In Fig. 3.10, in the middle panel, a part of the recognition pattern of fragments formed in  $^{112}\text{Sn} + ^{112}\text{Sn}$  reactions is presented. Recognition pattern is a two dimensional histogram of nuclear charges as a function of the mass-over-charge ratio. In the upper panel the projection of the plot on the mass-over-charge ratio axis for three isotopes,  $^{58}\text{Co}$ ,  $^{59}\text{Co}$  and  $^{60}\text{Co}$ , is shown. The mass resolution values for these selected isotopes are  $\Delta A/A = 0.49$  (*FWHM*), which are typical for this mass range. Data is measured in setting 9 (see Tab. C.2 in Appendix C), centered approximately at  $^{67}\text{Zn}$ . In the same figure (left panel) we show the projection of the plot on the nuclear charge axis after the corrections for energy loss measurements. Fig. 3.10, the middle panel, shows also the line segments drawn around the recognized isotopes. These line segments define conditions that are used in the further analysis for the accumulation of the velocity distributions for specific isotopes. The color scale of the 2-dimension recognition pattern is logarithmic. Fully corrected recognition patterns in the full measured range of isotopes, formed by plotting the  $A/Z$  ratio versus the nuclear charge of the fragments produced in both experiments are presented in Fig. 3.11 and 3.12. Settings dedicated for the measurement of light residues, i.e. with degrader, are given separately (left panel) from the heavy residue recognition plots measured without the degrader (right panel).

## 3.2 Measuring the velocity distributions

In previous chapter we obtained the identification plot by determining the charge and the mass-over-charge ratio for each event. To obtain the mass-over-charge ratio one uses the time-of-flight and  $B\rho$  measurements, according to the Eq. 3.9, in the second half of the spectrometer. Instead of determining also the velocity of fragments from the time-of-flight measurement, one may use another more accurate method. As already demonstrated in section 3.1.2, the velocity of individual fragments may be determined by measuring the transversal position at the intermediate focal plane, given by the scintillator SCI21, and by the magnetic fields in the first stage of the FRS. The resolution of  $10^{-4}$  of the momentum based on this method is roughly a factor of five better than what is achieved by the time-of-flight method. Therefore, all the velocities of the reaction products given in this thesis are deduced from the measured magnetic rigidities in the first half of the spectrometer. The information obtained from the second half gives the identification of the fragments.

When the fragment mass number  $A$  and nuclear charge  $Z$  are defined after the identification, the longitudinal velocities of the fragments can be calculated from the following equation:

$$\beta\gamma = \frac{1}{c} \cdot \frac{e}{m_0 + \delta m} \cdot \frac{(B\rho)_{A0} \cdot \left(1 + \frac{\Delta(B\rho)_{A0}}{(B\rho)_{A0}}\right) + \Delta(B\rho)_{Target}}{A/Z}, \quad (3.10)$$

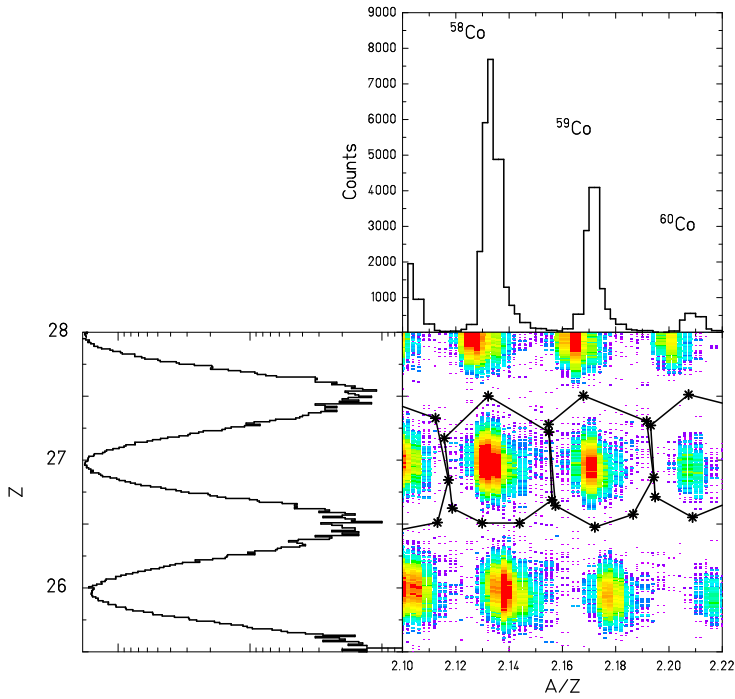


Figure 3.10: A close-up of the recognition pattern of fragments  $^{58}\text{Co}$ ,  $^{59}\text{Co}$  and  $^{60}\text{Co}$  formed in  $^{124}\text{Sn} + ^{124}\text{Sn}$  reactions. Recognized isotopes are enclosed with black line segments, that are used as conditions in further analysis. Projections to both dimensions of the 2-dimensional histogram are shown. Limits used in the plot and in the projections are the following:  $Z \in [25.5, 28]$  and  $A/Z \in [2.27, 2.33]$ .

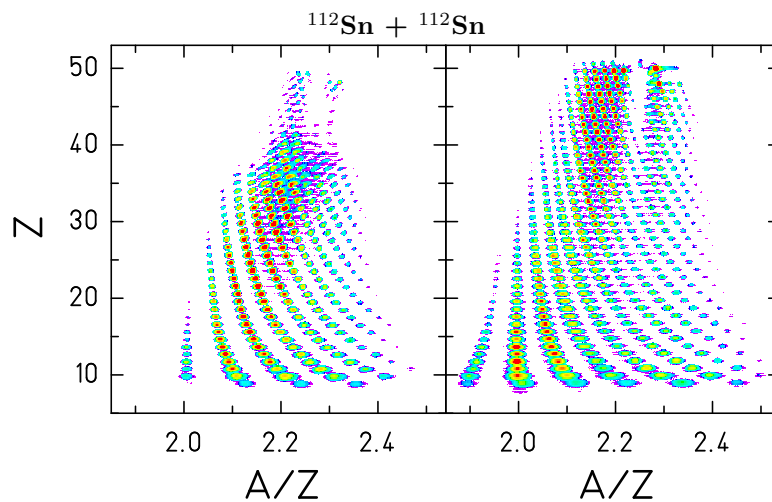


Figure 3.11: Recognition patterns of fragments formed in  $^{112}\text{Sn} + ^{112}\text{Sn}$  reactions. Settings measured with degrader (left) are shown separately from those obtained without degrader (right).

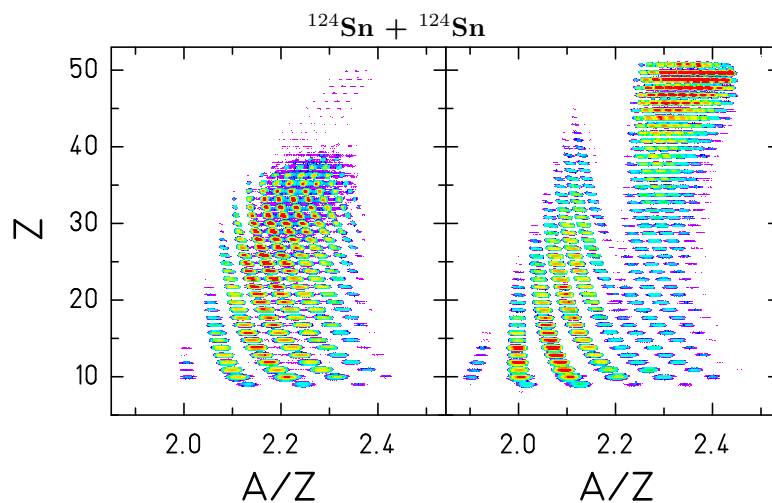


Figure 3.12: Recognition patterns of fragments formed in  $^{124}\text{Sn} + ^{124}\text{Sn}$  reactions. Settings measured with degrader (left) are shown separately from those obtained without degrader (right).

where  $c$  is the velocity of light,  $e$  is the elementary charge,  $m_0$  is atomic mass unit,  $\delta m = dM/A$  is the mass excess per nucleon,  $\gamma = \sqrt{(1 - \beta^2)^{-1}}$  and  $(B\rho)_{A0}$  is the magnetic rigidity of the ions in the central trajectory. This value is calculated by directly measuring the magnetic field measured with the Hall probes with a precision of about  $10^{-4}$ . The deviation of magnetic rigidity from the central value is calculated through the position displacement at S2:

$$\frac{\Delta(B\rho)_{A0}}{(B\rho)_{A0}} = \frac{x_{S2}}{D_{S2}}. \quad (3.11)$$

$\Delta(B\rho)_{Target}$  is due to fragments energy loss in the target. For the calculation of the mass excess a generalized empirical mass formula was used [MS66], which provided sufficient accuracy.

The velocities obtained by applying formula 3.10 were accumulated for each identified fragment with nuclear charge  $Z$ , and mass number  $A$ , into a longitudinal velocity distribution,  $Y_{i,meas}^{Z,A}(v_{\parallel})$ , i.e. a yield of the produced fragment with a longitudinal velocity  $v_{\parallel}$  obtained in a measurement with a magnetic setting  $i$ . Magnetic settings used in the measurements are listed in the Appendix C.

In the following three sections, 3.2.1, 3.2.2 and 3.2.3, it will be described what corrections were needed to apply to these distributions in order to reconstruct the full velocity distribution for every fragment. The procedure of reconstruction of the longitudinal velocity distributions is given section 3.2.4.

### 3.2.1 Correction for the beam dose

In order to compare the measurements from different settings, the data had to be normalized to the yield of the beam particles. The beam dose varied because of the measuring time was different depending on the purpose of the measurement and also because of the beam intensity was adjusted to optimize the data acquisition. In every setting, the number of beam projectiles in each spill, was measured by the current transformer (TRAFO), as described in subsection 3.1.1.

### 3.2.2 Dead time determination

Due to the high intensity of the fragments at the S2, the applicability of the scintillator SCI21 was limited by the dead-time of electronics. Dead-time corresponds to the processing time when the system is not able to register other events. This time was several orders of magnitude longer than the processing time of any individual detector itself. During the experiment, the dead-time

of the data-acquisition system was varying, depending on the counting rate, between 2% and 50%. The dead-time could be constantly monitored from the counters. If it surpassed 50%, then the beam intensity had to be lowered. For each setting, the dead-time values have been registered, and measured counting rates consequently corrected. Counting rates of the accepted events were of the order of  $\sim 10^3$  particles per second. The dead time in this experiment was determined by the processing time taken by each of one accepted event by the DAQ in the following way:

$$t_{Dead} = 1 - \frac{T_{Accepted}}{T_{Free}}, \quad (3.12)$$

where  $T_{Free}$  is the number of the free triggers and  $T_{Accepted}$  is the number of the accepted triggers registered by the DAQ.

Due to an error in the DAQ only the second word (16 bits) of the 32 bit integer value corresponding to trigger counts were recorded. This meant that the trigger counts could be read only in the accuracy  $2^{16} = 65536$ . Fortunately the trigger counts were large integer numbers exceeding this interval many times during data runs. What was recorded in the data was a step function showing closely the correct trigger count value when ever the first word was spilled. In Fig. 3.13 the values of the trigger counts at the moment of the spill are plotted as function of accepted trigger counts, which was fortunately recorded normally by the DAQ. The relative uncertainty of the dead time values were estimated to be 10%.

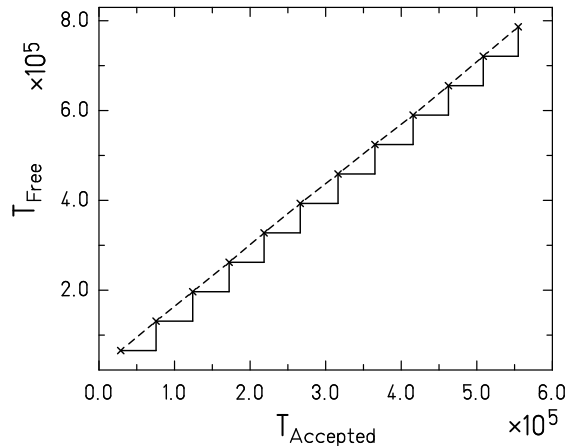


Figure 3.13: Dead time determination by comparing accepted triggers to actual recorded events.

### 3.2.3 Correction for the reduced FRS angular transmission

As stated earlier the angular acceptance of the FRS is limited to 15 mrad around the beam axis. However, inside this 15 mrad cone, the transmission of ions is not uniformly 100% but varies slightly as a function of the ion's magnetic rigidities in the first and second half of the FRS. Velocity distributions needed to be corrected for this variation of the angular transmission. While the heavy residues are produced with rather narrow angular distributions and they are fully transmitted through the FRS, the angular distributions of light residues are rather broad, and the angular transmission of these residues may be as low as 10%. The angular transmission of the FRS has been under intense investigation in many experiments in the past in case of fission and fragmentation processes. A detailed description of the transmission of each ion species through the magnetic fields of FRS is given in reference [BPCS02]. In the same work, an algorithm for correcting for the transmission losses is given. This algorithm has been adapted in this work. Since the ion's magnetic rigidity depends on their horizontal positions at the intermediate ( $x_2$ ) and final focal planes ( $x_4$ ) the ion optical calculation resulted in a certain transmission coefficient for every  $x_2$  and  $x_4$  position. The results are presented in Fig. 3.14, where the transmission reduction coefficient,  $T(x_2, x_4)$ , is plotted as function of the  $x_2$  and  $x_4$  positions of the ion. To correct for the lost counts the yields were multiplied with a weighting factor which was the inverse of the plotted reduction factor.

After this correction the velocity distributions closely represent the distributions inside the before mentioned angular acceptance of the spectrometer (15 mrad around the beam axis). The applied transmission correction factors were assumed to have a relative uncertainty of 15%.

### 3.2.4 Reconstruction of the velocity distributions

Each of the before mentioned corrections were applied to the measured velocity distributions. Data obtained from different settings were normalized to the primary-beam intensity, and corrected for the reduced angular acceptance and dead-time of the data-acquisition system before being merged. The corrected yield for each detected fragment in a magnetic setting  $i$  is given by the equation:

$$Y_i^{Z,A}(v_{\parallel}) = Y_{i,\text{meas}}^{Z,A}(v_{\parallel}) \cdot \frac{1}{N_{\text{beam}}} \cdot \frac{1}{t_{\text{Dead}}} \cdot \frac{1}{T(x_{S2}, x_{S4})}, \quad (3.13)$$

where  $N_{\text{beam}}$  is the yield of the beam particles that passed through the target during the measured setting,  $t_{\text{Dead}}$  is the dead time determined individually

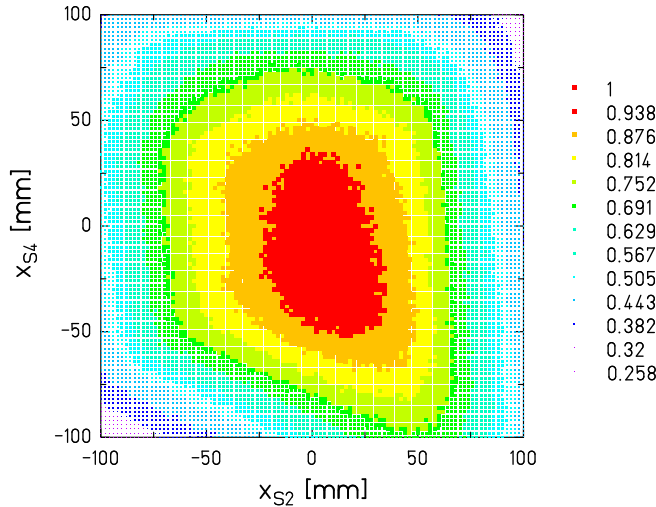


Figure 3.14: Transmission matrix used in the experiments to compensate the losses due to the reduced transmission inside the angular acceptance of the FRS. Matrix is obtained from the ion optical calculation described in the reference [BPCS02]. The color coding corresponds to penetration factor of the ion through the FRS determined completely by the fragments horizontal position at S2 and S4.

for each data file in each setting as described in section 3.2.2 and  $T(x_{S2}, x_{S4})$  is the transmission coefficient, introduced in section 3.2.3.

Due to the before mentioned narrow momentum acceptance of the FRS it is necessary to combine data from several measurements with different magnetic rigidities to cover the full range of velocities of each fragment. In case of the residues far away from the projectile, the velocity distributions are generally always wider than what one can measure in one setting. FRS momentum acceptance in each setting is 3% so the magnetic fields on dipoles were scaled by steps of 1.5% to assure a sufficient overlap of the velocity distributions measured in the neighboring settings. Because of the border effects stemming from the angular acceptance, a rather large overlap was desired to ensure the correct shape of the full velocity distribution. The full velocity distribution,  $Y_{\text{tot}}^{Z,A}(v_{\parallel})$ , for each fragment was obtained by joining of the yields with following rule:

$$Y_{\text{tot}}^{Z,A}(v_{\parallel}) = \text{MAX}(Y_i^{Z,A}(v_{\parallel}), Y_{i+1}^{Z,A}(v_{\parallel})), \quad (3.14)$$

where the  $\text{MAX}()$  function takes the largest value of each overlapping bin of the two neighboring velocity distributions. The panel (a) of Fig. 3.15 illustrates

the velocity distributions obtained from 14 measured settings shown in different colors in the figure. The panel (b) shows the full velocity distribution obtained by applying Eq. 3.14.

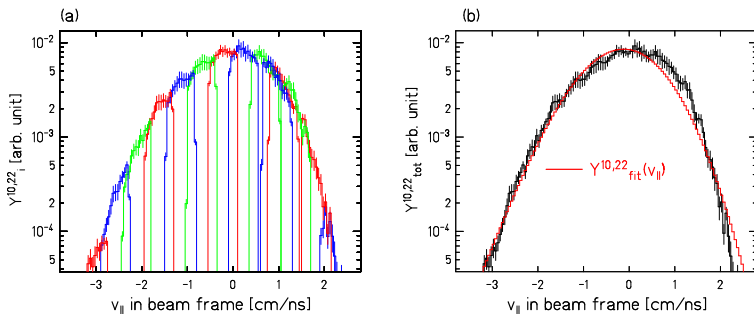


Figure 3.15: (a) Velocity distributions of the isotope  $^{22}\text{Ne}$  ( $Z=10, A=22$ ) measured in the  $^{124}\text{Sn} + ^{124}\text{Sn}$  experiment in total of 14 different magnetic field settings that are shown separated. (b) The full velocity distribution of  $^{22}\text{Ne}$  after the joining described by the Eq. 3.14. The error bars are shown for each bin of the velocity distribution. Certain periodic structure due to imperfectness of the joining and due to imperfect correction for the reduced angular transmission can be seen.

For the sake of more quantitative analysis, the joined longitudinal velocity distributions  $Y_{\text{tot}}^{Z,A}(v_{\parallel})$  were fitted with a function consisting of one Gaussian with an exponential tail:

$$Y_{\text{fit}}^{Z,A}(v_{\parallel}, N, \mu, \sigma, \tau) = N \cdot \left[ \frac{1}{\sqrt{2\pi}\sigma^2} e^{-\frac{(v_{\parallel} - (\mu - \tau))^2}{2\sigma^2}} + \frac{1}{\tau} e^{-\frac{v_{\parallel}}{\tau}} \right], \quad (3.15)$$

where the  $N$  is the normalization factor,  $\mu$  and  $\sigma$  are the mean value and standard deviation, respectively, and  $\tau \in [-\infty, 0]$  is the decay constant of the exponential tail. In Fig. 3.15 in panel (b) the fitted function,  $Y_{\text{fit}}^{10,21}(v_{\parallel})$ , is presented. This fitting function was chosen because it resembled the experimental data sufficiently well. Advantage of the fitting was to get rid of some unwanted features of the distributions that were introduced only due to experimental limitations. Fitting smoothed out the periodic distortion, visible in the joined distribution, caused by the imperfect joining and the imperfect transmission correction.

From the fitted function to the final velocity distribution, the width and the mean value of the velocity distributions were determined. The integral of the fitted function serves as a basis for its production cross-section. This is described in more detail in the next section.

### 3.3 Evaluation of the formation cross-sections

The number of interactions between the projectile and target that led to the formation of the given fragment is obtained, roughly, from the integral of the fitted function to the fully reconstructed longitudinal velocity distribution for that fragment:

$$Y_{\text{tot}}^{Z,A} = \int_v Y_{\text{fit}}^{Z,A}(v_{\parallel}) dv_{\parallel} \quad (3.16)$$

By using this method one ensures that there is no double counting due to the overlap of the neighboring magnetic-field settings. To define the production cross-section for each fragment we still need to determine the following three quantities:

1. Density of the target nuclides where the beam is passing
2. Losses due to limited acceptance of the FRS
3. Amount of fragments produced in secondary reactions

The first quantity is used to normalize the yield obtained from the integral. We may note that the total yield,  $Y_{\text{tot}}^{Z,A}$ , is already normalized for the yield of beam particles,  $N_{\text{beam}}$ , that passed through the target during the measured production yield of the fragment, as described earlier in section 3.1.1. The following two quantities are needed to be corrected for in order to obtain the production cross section for each measured fragment. Finally we may write the formula for determine the production cross section:

$$\sigma_{\text{tot}}^{Z,A} = Y_{\text{tot}}^{Z,A} \cdot \frac{1}{N_{Sn}} \cdot T(\sigma_{\theta}) \cdot \alpha(A), \quad (3.17)$$

where  $N_{Sn}$  is the number of target nuclides.  $T(\sigma_{\theta})$  is the correction for the limited FRS angular acceptance and  $\alpha(A)$  is the correction factor for the secondary reactions. We may note that these three quantities have no clear dependence to the velocity of the fragment and therefore affect only the total yield of the fragment. In other words the moments of the velocity distribution remain unchanged. In the following sections it will presented how these three quantities were determined.

#### 3.3.1 Target thickness

The density of the target nuclides can be calculated by first considering the number density (number of individual scattering centers per unit volume),  $n$ , of the target:

$$n = \frac{\rho \cdot N_{Av}}{A}, \quad (3.18)$$

where  $N_{Av} = 6.022 \cdot 10^{23} \text{ mol}^{-1}$  is Avogadro's number,  $A$  is the atomic weight of the material given in  $\text{mg} \cdot \text{mol}^{-1}$  and  $\rho$  is the density of the material given in  $\text{mg} \cdot \text{cm}^{-3}$ .

The number of target nuclei over unit the area  $N_{Sn}$  is equal to the number of individual scattering centers per unit volume,  $n$ , times the thickness,  $x$ , of the target:

$$N_{Sn} = n \cdot x = \frac{\rho \cdot N_{Av}}{M} \cdot \frac{T}{\rho} = \frac{N_{Av} \cdot T}{M}, \quad (3.19)$$

where  $T$  is the density thickness of the target in  $\text{mg} \cdot \text{cm}^{-2}$   $M$  the atomic weight of the target material [ $\text{mg} \cdot \text{mol}^{-1}$ ]. Numerical values for the quantities in the equation 3.19 are given in Tab. 3.2 for both tin targets used in the experiment. Target thicknesses are the balanced result of maximum production rate while keeping the rate of secondary reactions low. More information about the used targets can be found from Appendix A.

target	$T$ [ $\text{mg} \cdot \text{cm}^{-2}$ ]	$M$ [ $\text{g} \cdot \text{mol}^{-1}$ ]	Enrichment [%]
$^{112}\text{Sn}$	$126.7 \pm 0.6$	$112.4 \pm 0.2$	$99.5 \pm 0.2$
$^{124}\text{Sn}$	$141.8 \pm 0.7$	$123.9 \pm 0.2$	$97.5 \pm 0.2$

Table 3.2: Numerical values used in the equation 3.19.

### 3.3.2 Correction for the limited angular acceptance

For the evaluations of the production cross-sections, the part of the velocity distributions outside the angular acceptance needed to be estimated. The estimation was based on the isotropy assumption from which it follows that the overall velocity distributions in three-dimensional space have the same standard deviation as the reconstructed longitudinal velocity distributions inside the angular acceptance of the spectrometer. This procedure is especially reliable for the narrow distributions of the heavy residues but the cross-sections of the light residues ( $Z \lesssim 14$ ) may have been somewhat underestimated due to the shape asymmetries in their velocity distributions.

In the same work [BPCS02], analytical formulae that quantify the transmission losses due to the limited angular acceptance are given and are shortly reported here below.

The transmission of a residue having an angular distribution of standard deviation  $\sigma_\theta$  in the laboratory frame may be expressed as follows:

$$T(\sigma_\theta) = 1 - \exp\left(-\frac{\alpha_{eff}^2}{2\sigma_\theta^2}\right) \quad (3.20)$$

where  $\alpha_{eff}^2$  ( $\approx 0.015$  rad) denotes the effective angular acceptance of the FRS in millirads. The use of the effective angular acceptance accounts for a non-spherical cross-section of the FRS tube, which is defined by the shape of the quadrupoles. The value represents the radius of a circular aperture of the same area as the cross-section of the FRS tube.  $\sigma_\theta$  is the standard deviation of the Gaussian describing the angular spread in the laboratory frame, which is correlated to the standard deviation of the observed velocity distribution by the equation:

$$\sigma_\theta = \frac{\sigma_{v_{frag}}}{v_{beam}} \sqrt{1 - \beta_{beam}^2}. \quad (3.21)$$

The  $\sigma_{v_{frag}}$  was estimated to be equal to the width obtained from the fit to the longitudinal velocity distribution. For the lightest ( $Z \approx 10$ ) fragmentation residues presented in this thesis, the transmission is around 35%. At around  $Z \gtrsim 36$  the full velocity distributions of the residues become narrow enough to be fully transmitted through the FRS ( $T(\sigma_\theta) = 100\%$ ).

Uncertainties related to the determination of the production cross-sections will be discussed in the section 3.4.

### 3.3.3 Correction for secondary reactions

Both projectiles and reaction products may interact with the material inserted in the beam line deteriorating the yields of the fragments formed in the target by the primary beam. Depending on the thickness and the nuclear charge of the material this reaction probability may not be very small. Therefore a correction function  $\alpha(A)$  was determined for each of the measurement setups according to the materials present. The function  $\alpha(A)$  was determined by using a program AMADEUS [Sch], which gives the percentage of nuclear reactions in matter for a given fragment. Correction factors calculated for different atomic masses with AMADEUS are shown in Fig. 3.16 in case of two different experimental setups corresponding to different layers of material in beam line. Correction function  $\alpha(A)$  was obtained by fitting a function to these calculated points. The obtained function represent the total correction factor as function of fragment mass number to recover the losses due to secondary reactions in the scintillator or in the combination of scintillator and degrader. In these experiments thin targets were used, for which the probability of two sequential reactions is negligible. Therefore the influence of the targets was neglected from the calculation.

Finally, to ensure that each count in the distribution corresponding to given  $A$  and  $Z$  in the identification plot indeed represents this isotope and does not come from products of ionic charge-changing processes and secondary reactions in the detector materials and degrader in the beam line, all spectra were accumulated under the condition that each measured fragment had the same ratio  $A/Q$

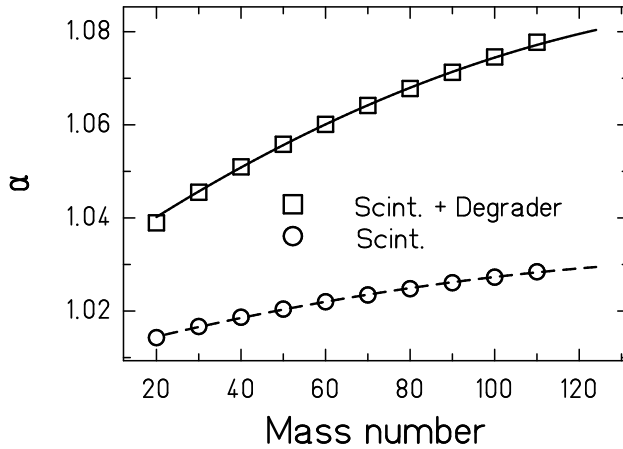


Figure 3.16: Secondary-reaction correction factor in different layers of matter obtained from AMADEUS [Sch] calculation.

in both stages of the FRS. Due to this constraint on the  $A/Q$  ratio the ions which undergo ionic charge-changing processes and which are responsible for the most of the contaminants can be suppressed efficiently. The amount of remaining contaminants from background of secondary-reaction products which were transmitted to the final image plane and fulfilled the constraint on the  $A/Q$  and on the energy loss in the ionization chamber, was estimated to be less than 1%. More details can be found in ref. [EAB<sup>+</sup>02]. We assume a relative uncertainty of 10% for the correction factors for secondary reactions.

### 3.4 Error analysis

This section discusses the certainty of the experimental results presented in this thesis. The results consist of first two moments of the velocity distributions and the production cross-sections of the detected fragmentation residues. Contribution of each individual experimental source of uncertainty to the overall uncertainty is presented.

### 3.4.1 Uncertainty of the velocity distribution

Experimental uncertainties (random errors) can be revealed by repeating the exact same measurement several times. In this case each value in the velocity distribution represent the velocity of different fragment, although with same mass number and nuclear charge, they represent a result from different measurement. Each of the fragments can have very different evolution and due to physics they emerge in different velocities. To be able to study quantitatively the variation of the velocities due to physical reasons it is very important to be able to tell the amount of the velocity variation due to experimental reasons.

In section 2.1.2, the momentum resolving power of the FRS was demonstrated to be able to separate momentum with a relative precision of  $6 \cdot 10^{-3}$ . In this calculation the position measurement were performed with MW-chambers, being able to measure position with 4 mm (FWHM) precision. However, in the data measurements the horizontal position was measured with the scintillators, at S2 and S4, each having the absolute uncertainty of 3 mm (FWHM). Also the uncertainties in dispersion and in magnetic rigidity were not taken into account.

In order to realistically estimate the uncertainty of individual velocity measurement of one detected fragment, one needs to propagate the uncertainties of  $B\rho$ ,  $x$  and  $D$  measurements, which are the quantities directly used to obtain the velocity as shown in the equation 2.1. The fractional error in the magnetic rigidity,  $B\rho$ , was estimated to be  $5 \cdot 10^{-4}$ . The value of the dispersion,  $D_{S2}$ , was determined with fractional uncertainty of  $3 \cdot 10^{-4}$ . Effect of these uncertainties to the uncertainty in momentum can be calculated through the law of error propagation:

$$\Delta |\vec{P}_{Lab}| = \sqrt{\left(\frac{\partial |\vec{P}_{Lab}|}{\partial(B\rho)} \Delta(B\rho)\right)^2 + \left(\frac{\partial |\vec{P}_{Lab}|}{\partial x_{S2}} \Delta x_{S2}\right)^2 + \left(\frac{\partial |\vec{P}_{Lab}|}{\partial D_{S2}} \Delta D_{S2}\right)^2}. \quad (3.22)$$

Substituting the numerical values into the equation for typical settings measured in the experiment one finds the relative error for momentum to be:

$$\Delta |\vec{P}_{Lab}| = \sqrt{(5 \cdot 10^{-4})^2 + (5 \cdot 10^{-4})^2 + (3 \cdot 10^{-4})^2} = 7.7 \cdot 10^{-4}. \quad (3.23)$$

Unfortunately this is not sufficient error analysis when one is determining properties of the whole distribution of measured velocities. One has to also estimate the amount of those fragments that were not detected because the count losses can have drastic consequences on the shape of the distributions. As it was discussed earlier in section 3.2.3, the FRS transmission is known not to be 100% for all of the horizontal trajectories, but the transmission coefficients has been found to be a function of horizontal positions at S2 and S4. The systematic

error in the transmission coefficients was estimated according to the following formula:

$$\delta T(x_{S2}, x_{S4}) = (1.0 - T(x_{S2}, x_{S4})) \cdot 0.1, \quad (3.24)$$

which describes the error of the transmission coefficient to be 10% of the value by which the factor deviates from 1. In Tab. 3.3 two extreme cases of transmission factors are illustrated together with their uncertainties. The final error

$x_{S2}, x_{S4}$ position [cm]	$T_{12}$	absolute error [cm]	fractional error
0.5, 0.5	0.974	0.0026	0.0031
4.5, -5.5	0.864	0.0136	0.0818

Table 3.3: Examples of the transmission coefficients and their estimated uncertainties for two different trajectories passing the focal planes at  $x_{S2}$  and  $x_{S4}$ .

for each bin in the momentum distributions were calculated by combining in quadrature the statistical uncertainties and the estimated systematic uncertainties of the applied correction factors. The systematic error in the correction factor for transmission gives the largest contribution for the error of the bin counts in many cases but not always since it is position dependent.

The width and the mean value of the longitudinal velocity distributions were determined from the fitted curve as described in section 3.2.4. Area of the fitted curve also served as the basis for the calculation of production cross sections. The fitting procedure took into account the errors assigned to each bin and found the best fitted curve by minimizing the RMS of the bin counts. Fitting routine gave directly uncertainties for the width and the mean value of the longitudinal momentum distributions. The uncertainty introduced by the fitting procedure itself is typically of the order of 2% for each extracted parameter. This uncertainty is overwhelmed by the uncertainties stemming from the bin content uncertainty, thus justifying the use of the chosen fit function. The uncertainty of the production cross section needed some extra considerations and is discussed in the next section.

### 3.4.2 Uncertainty of the production cross section

The area, given by the fit routine, represents the total measured yield of the fragments inside the FRS angular acceptance. Fitting routine also gave the uncertainty for the area which served as a basis for the cross section uncertainty. The estimation of the parts outside of the FRS acceptance, as presented in section 3.3.2, introduced additional uncertainty for the production cross sections. The correction factors  $T(\sigma_\theta)$  were estimated to have a relative uncertainty of 10%. Another source for losses of detected fragments comes from the secondary

reactions as described earlier in section 3.3.3. The systematic uncertainty of the secondary reaction correction factors were estimated to be 10%.

The final error for the production cross section were calculated by combining in quadrature the error for the measured yield of the produced fragment, given by the fitting routine, and uncertainties of the applied correction factors:

$$\delta\sigma_{\text{tot}}^{Z,A} = \sqrt{\left(\delta Y_{\text{tot}}^{Z,A}\right)^2 + (\delta T(\sigma_{\theta}))^2 + (\delta\alpha(A))^2} \quad (3.25)$$

Other systematic errors that might have not been considered have no meaningful contribution, when combined in quadrature with estimated ones, if they are in total less than 3%.

In the next chapter the experimental results together with their uncertainties are presented.



# Chapter 4

## Experimental results

With the method described in the previous chapter we obtained the longitudinal velocity distributions of the projectile residues – fully identified in mass and nuclear charge – in the reactions  $^{112}\text{Sn} + ^{112}\text{Sn}$  and  $^{124}\text{Sn} + ^{124}\text{Sn}$  at an incident beam energy  $1.4\text{ GeV}$ .

In the section 4.1 the features of the velocity distributions will be analyzed and their width and the mean value will be presented. The production cross-sections were determined, and will be presented in section 4.2.

### 4.1 Velocity distributions and their moments

In Fig. 4.1 and in Fig. 4.2 some examples of the measured distributions of longitudinal velocity inside an angular acceptance range of  $15\text{ mrad}$  around the beam direction in the frame of the projectile are presented for few selected nuclides. By observing the velocity distributions and without going into details of different reaction mechanisms, one can explain the general features in the frame of abrasion-ablation model [GS91]. In this model the heaviest fragments shown in Figs. 4.1 and 4.2 are produced in peripheral collisions with small overlap between the projectile and the target nucleus. This results in a formation of slightly excited prefragments, which then de-excite via evaporation of neutrons, light charged particles and light clusters. As the number of abraded nucleons is small, the fluctuations in the velocity distribution of the created prefragments are also small [Gol74], and as a consequence the evaporation stage only slightly increases the width of the velocity distribution. Thus, these residues show narrow velocity distributions with the mean value only

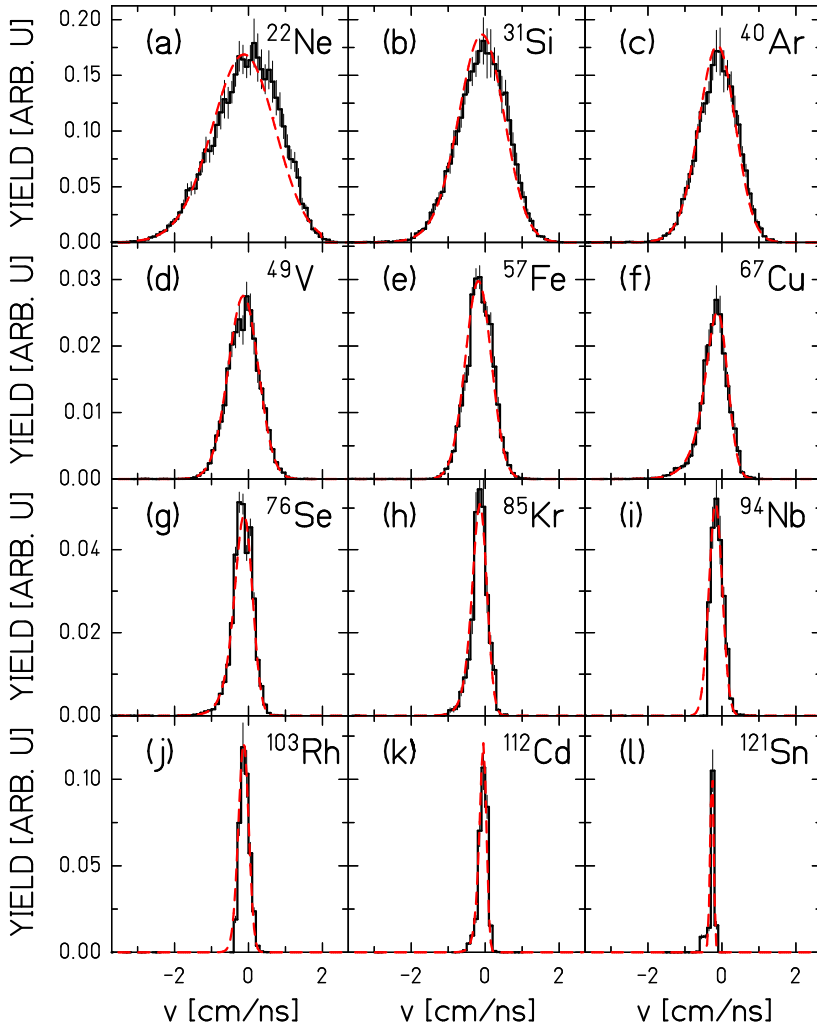


Figure 4.1: Velocity distributions in the rest frame of the projectile for several nuclides measured in the reaction  $^{124}\text{Sn} + ^{124}\text{Sn}$ . The fitted functions are shown as dotted lines.

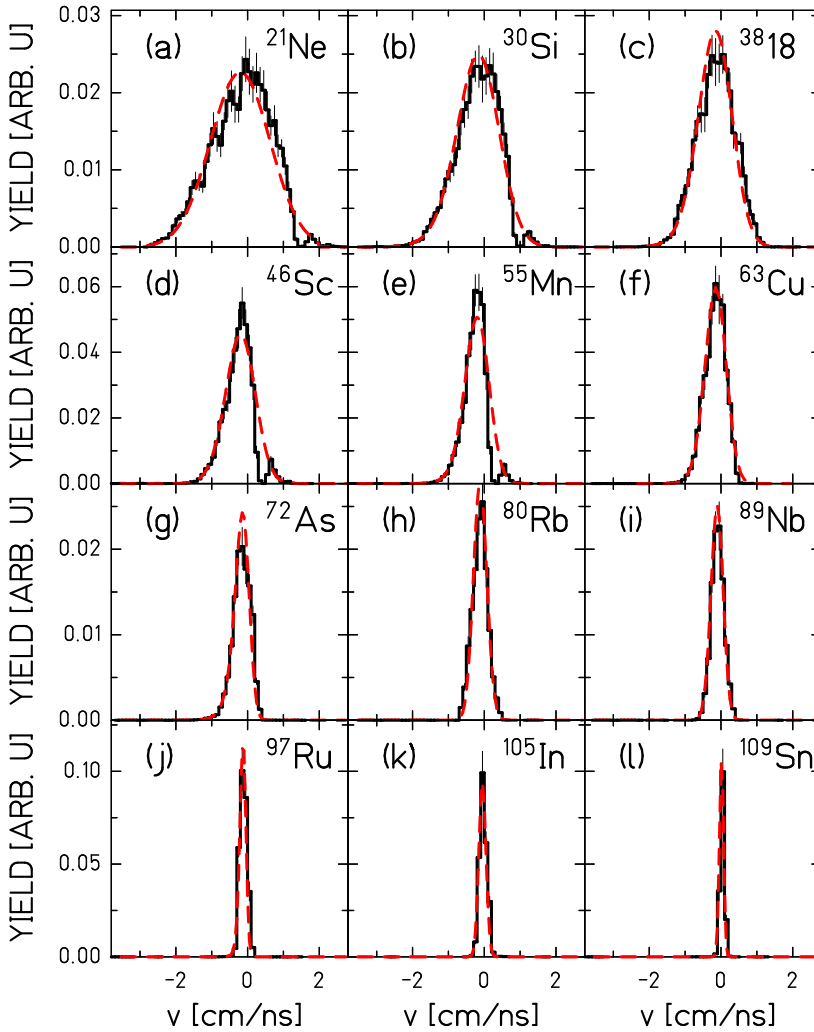


Figure 4.2: Velocity distributions in the rest frame of the projectile for several nuclides measured in the reaction  $^{112}\text{Sn} + ^{112}\text{Sn}$ . The fitted functions are shown as dotted lines.

slightly lower than that of the beam particles. Lighter residues are presumably produced at less peripheral collisions, where the introduced excitation energy can be high enough for thermal instabilities to set in [BMBB<sup>+</sup>95, SKW<sup>+</sup>96]. These residues portray wider velocity distributions, indicating a larger number of abraded and evaporated nucleons. For all the residues, the longitudinal velocity distributions show Gaussian-like shape with slightly enhanced tails in the slower side in case of the lighter residues. This asymmetry in the shape of velocity distributions of the lightest residues shows, as discussed in references [R<sup>+</sup>06, NSB<sup>+</sup>04, HSR<sup>+</sup>08, NSTG11] that these fragments have been produced via different reaction mechanisms like e.g. simultaneous and/or sequential decay. The de-excitation scenario will be discussed in more detail in chapter 6 in the frame of statistical multifragmentation code [GS91].

Figs. 4.1 and 4.2 show the measured data and the fitted curve as introduced in section 3.2.4. Some of the measured velocity distributions show, especially in the case of  $^{112}\text{Sn} + ^{112}\text{Sn}$ , cuts caused by the slits, which were inserted to protect the detectors from the primary beam and its first two charge states; see e.g.  $^{21}\text{Ne}$ ,  $^{30}\text{Si}$ ,  $^{46}\text{Sc}$  or  $^{55}\text{Mn}$  in Fig. 4.2. The fitting procedure could, thus, recover some of the incompletely measured velocity distributions.

A survey of the longitudinal velocity distributions in the reference frame of the primary beam for both systems is shown in Fig. 4.3. It displays two-dimensional cluster plots of the longitudinal velocities as function of fragment's nuclear charge. Velocities are accumulated from all the velocity distributions of the fragments with same nuclear charge. This figure shows the gradual broadening of the velocity distributions with decreasing fragment's nuclear charge. The color scale is logarithmic and represents the relative abundances of the velocity for each mass number of the fragment. The analysis of the spectra shows that the peak of the total velocity distribution, i.e. in sum of all components, for all fragments, lies in the range from  $v_{proj}$  down to  $\sim 0.947v_{proj}$ . The widths are also small compared to the beam velocity: slowest measured fragment had a velocity of  $\sim 0.874v_{proj}$  and the fastest  $\sim 1.12v_{proj}$ . These two moments are further discussed in the following sections.

### 4.1.1 Width of the velocity distributions

In Fig. 4.4 the width, standard deviation  $\sigma_{\parallel}$  of the fitted Gaussian function with exponential tail (see Eq. 3.15), is given for the longitudinal momentum distributions for all fragments measured in two reactions.

From this figure we see that the width of the measured longitudinal momentum distributions first increase with decreasing mass of the final residue. The maximum is reached for the final-fragment mass close to half the mass of the projectile. For lower masses, the width starts, as expected, to decrease.

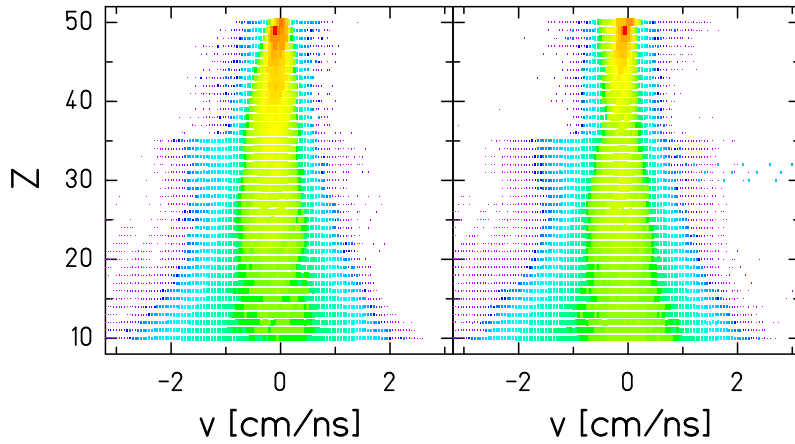


Figure 4.3: Left: Longitudinal velocity distributions in the rest frame of the projectile as function of the fragment’s nuclear charge measured in the reaction  $^{112}\text{Sn} + ^{112}\text{Sn}$ . Right: Same plot for the fragments measured in the reaction  $^{124}\text{Sn} + ^{124}\text{Sn}$ . The color scale is logarithmic and represents the relative abundances of the velocity  $v$  for each mass number of the fragment.

An often used description of the momentum width is based on the empirical approach of Morrissey [Mor89]. Although this approach describes sufficiently well the width of the momentum distribution close to the projectile, it fails severely for the masses smaller than half the projectile mass, see Fig. 4.4.

According to the statistical model of Goldhaber [Gol74], the longitudinal momentum fluctuations of the projectile-like fragments after the first reaction stage are determined by the intrinsic Fermi motion of the constituent nucleons which are removed from the projectile during the abrasion process. In this model the individual nucleons within the projectile have their own momenta that sum up to zero in the rest frame of the projectile. The abrasion stage then removes nucleons with no preference with respect to their momentum, and the momenta of the remaining nucleons in the prefragment may not sum up to zero anymore. Due to the momentum conservation, the sum of momenta of abraded nucleons, has to be opposite to the momentum of the prefragment. More nucleons are removed in abrasion more fluctuations of the remaining total momentum may occur, and the maximum is reached for masses equal the half of the mass of the projectile. By this model, the projectile remnants end up with a three-dimensional Gaussian-shape momentum distributions, whose widths are determined by the number of removed nucleons. The Gaussian shape follows from statistical arguments, when a large number ( $>3$ ) of nucleons is abraded.

Evaporation residues experience an additional broadening of the momentum

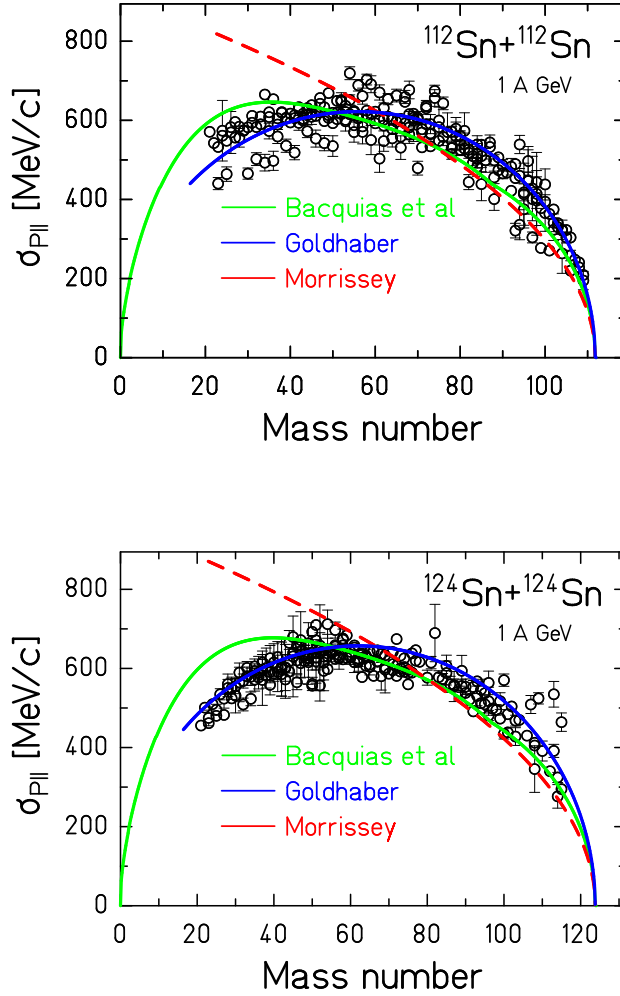


Figure 4.4: Standard deviation of the Gaussian part of the fitted functions to the fragment momentum distributions for both systems;  $^{112}\text{Sn}(1\text{A GeV})+^{112}\text{Sn}$  (upper diagram) and  $^{124}\text{Sn}(1\text{A GeV})+^{124}\text{Sn}$  (lower diagram). Given curves represent the prediction of Bacquias *et al* [BFH<sup>+</sup>11] (green), model of Goldhaber [Gol74] (blue) and the empirical parametrization by Morrissey [Mor89] (red).

distribution due to the recoil of the evaporated particles and light charged particles. But this contribution is small compared to the above-mentioned width introduced in the abrasion. Multifragmentation produces additional broadening of the momenta, mostly by the Coulomb explosion of the source (Coulomb repulsion between all fragments after break-up). But again, this contribution is smaller than the momentum width due to abrasion.

The impact of all the before mentioned de-excitation processes to the development of the momentum width were recently combined with the initial momentum description, provided by Goldhaber [Gol74]. This procedure is described in more detail in the work of Bacquias *et al.* [BFH<sup>+</sup>11]. In Fig. 4.4 the experimentally obtained widths of the momentum distributions as function of the residue mass are shown together with the predictions. The predictions include the cut due to FRS limited angular acceptance. The size of the additional fluctuations of momenta due to decay stages, given by Bacquias *et al.*, can be seen in Fig. 4.4 by comparing it to the prediction of the original Goldhaber model, which only includes the determination of residue width due to Fermi momenta of remaining nucleons.

The predictions suggest that the width of the momentum distributions has a very well established physics behind it.

### 4.1.2 Mean value of the velocity distributions

Another characteristic of the velocity distribution is the mean value. In Fig. 4.5 we present the average longitudinal mean velocity in the frame of the projectile i.e as deviations from the projectile velocity for each mass number of the fragmentation residues ( $A_{frag}$ ) produced in the peripheral and mid-peripheral collisions induced by  $^{124}\text{Sn}$  and  $^{112}\text{Sn}$ , as a function of their relative mass loss defined as  $(A_{frag} - A_{proj})/A_{proj}$ . The data points represent the weighted average values of the different isobars. Uncertainties for the mean values were determined and are shown in the figure if they are larger than the symbol size. In this figure the dotted line shows the expected mean velocities according to the systematics of Morrissey [Mor89]. The mean value represents the overall velocity shift induced in these reactions. A similar pattern is observed in both systems. Residues close to the projectile show a clear decrease of the mean velocity with their mass loss which closely follows the systematics of Morrissey [Mor89]. For this region, there are also no differences between the mean velocities in the two systems. The Morrissey systematics does not contain any interpretation about the reaction mechanism, it is just a fit made to the available data at that time. Nevertheless, this behavior can be explained by simple two-body interaction, namely friction, between the projectile and target nuclei in peripheral heavy-ion collisions. Friction appears as a consequence of interactions between the projectile and target matter in the overlapping region,

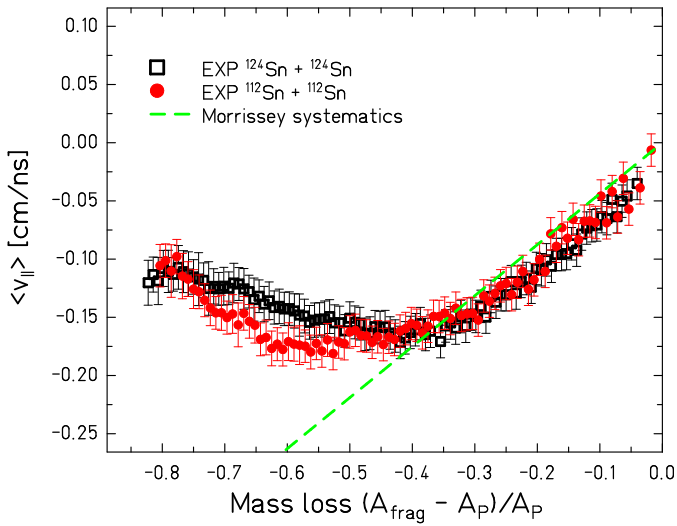


Figure 4.5: Mean value of the longitudinal velocity distributions in the frame of the projectile of residues produced in peripheral and mid-peripheral collisions for the systems  $^{124}\text{Sn}$  ( $1\cdot A$  GeV) +  $^{124}\text{Sn}$  (open squares) and  $^{112}\text{Sn}$  ( $1\cdot A$  GeV) +  $^{112}\text{Sn}$  (filled circles) as a function of their relative mass loss. The data points are weighted averages of the mean values of the different isobars. The mean values represent the mean velocities inside an angular range of 15 mrad.

and leads to a conversion of relative kinetic energy into excitation energy of projectile and target spectators. Due to this loss in kinetic energy, the velocity of the spectator residues is slightly shifted towards the velocity of the reaction partner, i.e. projectile residues are slowed down [AMHS76, WDD<sup>+</sup>94].

However, in less peripheral collisions, the two-body kinematics is no longer applicable since there occurs a formation of participant zone and the projectile and target spectators emit particles. In Fig. 4.5 at relative mass losses around 0.4, corresponding to  $A \approx 67$  and  $A \approx 74$  in  $^{112}\text{Sn} + ^{112}\text{Sn}$  and in  $^{124}\text{Sn} + ^{124}\text{Sn}$ , respectively, the mean velocity levels off, and for large mass losses the mean velocity starts to rise again. This is in clear contrast with the friction picture, according to which one would expect more kinetic-energy dissipation as the mass of the residue is decreasing and, thus, lower velocity. For the lowest masses with more than 0.5 relative mass loss the data suggest that there is also a small deviation between the two systems. The discussion of this re-acceleration effect and comparison with theoretical predictions is a topic of the next chapters.

## 4.2 Production cross-sections

As already discussed, the velocity distributions served also to determine the production cross-sections of the measured fragments. An overview of the measured production cross-sections presented on the chart of nuclides is shown in Fig. 4.6. For several isotopes the cross-sections could not be determined due to lack of statistics or because of severe cuts in the velocity distributions, or simply because of the limited range of the magnetic rigidity that was measured. The nuclide production cross-sections are plotted in Figs. 4.7, 4.8 and 4.9, and also given, together with their uncertainties in the Appendix D. Figs. 4.7, 4.8 and 4.9 also show the cross sections obtained from the EPAX parametrization [SB00]. EPAX is a semi-empirical parametrization of the cross-sections of heavy residues from fragmentation reactions based on the idea that fragmentation products result from long, sequential evaporation chains, at the end of which the so called evaporation attractor line is reached. Fragment cross-sections obtained in both experiments agree with the EPAX parametrization reasonably well.

In Fig. 4.10 the mean  $N/Z$ -ratio obtained from the isotopic distributions of the elements produced in these reactions are presented as a function of the charge of the element. Only the elements for which the maximum of the isotopic distribution was determined were considered when extracting the mean  $N/Z$ -ratio. The fragment cross sections obtained in the reaction  $^{124}\text{Sn} + ^{124}\text{Sn}$  show larger mean neutron number for each element than the fragments obtained from the reaction  $^{112}\text{Sn} + ^{112}\text{Sn}$ . This behavior corresponds to the idea of

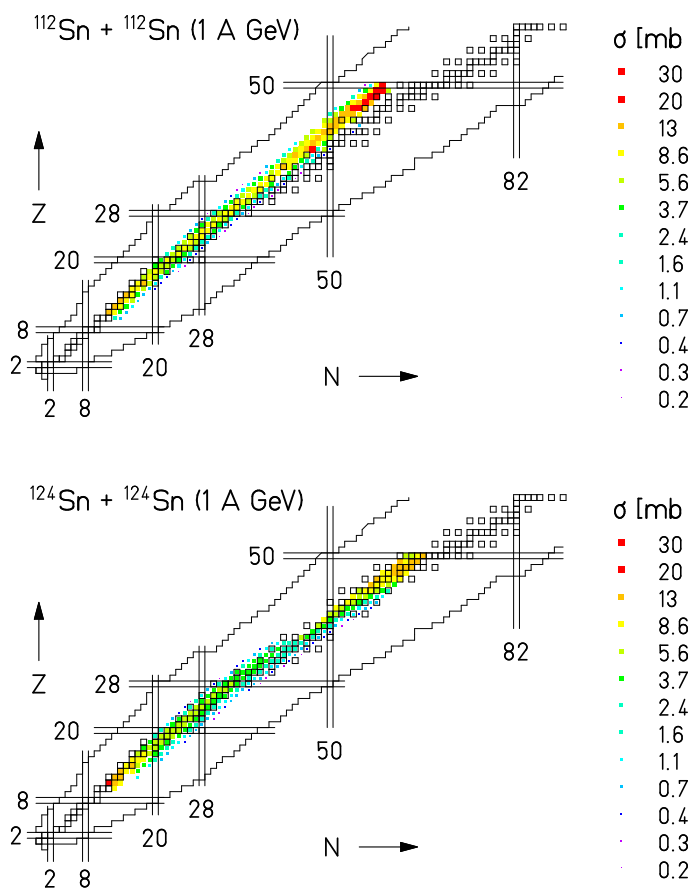


Figure 4.6: Cross-sections for both systems;  $^{112}\text{Sn}(1 \cdot A \text{ GeV}) + ^{112}\text{Sn}$  (upper diagram) and  $^{124}\text{Sn}(1 \cdot A \text{ GeV}) + ^{124}\text{Sn}$  (lower diagram).

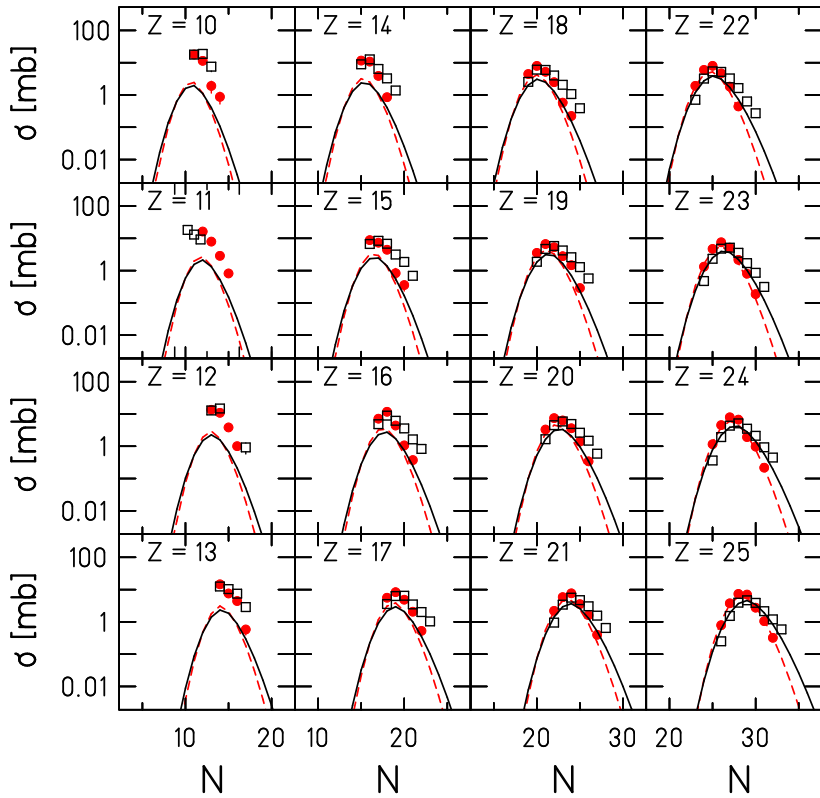


Figure 4.7: Isotopic cross-sections of the measured fragments with nuclear charge  $Z=10$  to  $Z=25$  in the reaction  $^{112}\text{Sn} + ^{112}\text{Sn}$  @ 1.4 GeV (filled dots) and in  $^{124}\text{Sn} + ^{124}\text{Sn}$  @ 1.4 GeV (open squares). Dashed lines represent the prediction of EPAX [SB00] for  $^{112}\text{Sn} + ^{112}\text{Sn}$  and solid lines for  $^{124}\text{Sn} + ^{124}\text{Sn}$ .

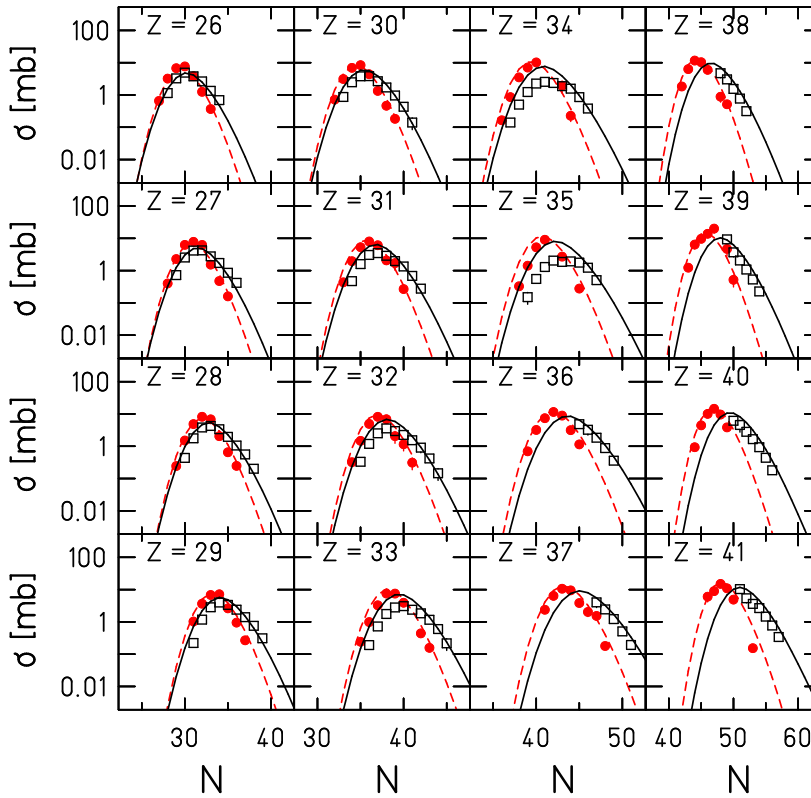


Figure 4.8: Isotopic cross-sections of the measured fragments with nuclear charge  $Z=26$  to  $Z=41$  in the reaction  $^{112}\text{Sn} + ^{112}\text{Sn}$  @  $1\cdot A$  GeV (filled dots) and in  $^{124}\text{Sn} + ^{124}\text{Sn}$  @  $1\cdot A$  GeV (open squares). Dashed lines represent the prediction of EPAX [SB00] for  $^{112}\text{Sn} + ^{112}\text{Sn}$  and solid lines for  $^{124}\text{Sn} + ^{124}\text{Sn}$ .

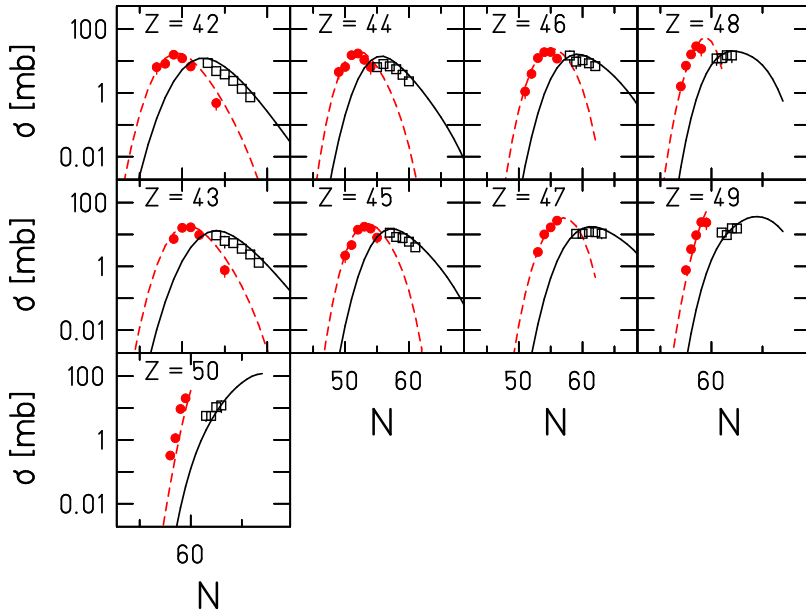


Figure 4.9: Isotopic cross-sections of the measured fragments with nuclear charge  $Z=42$  to  $Z=50$  in the reaction  $^{112}\text{Sn} + ^{112}\text{Sn}$  @  $1\cdot A$  GeV (filled dots) and in  $^{124}\text{Sn} + ^{124}\text{Sn}$  @  $1\cdot A$  GeV (open squares). Dashed lines represent the prediction of EPAX [SB00] for  $^{112}\text{Sn} + ^{112}\text{Sn}$  and solid lines for  $^{124}\text{Sn} + ^{124}\text{Sn}$ .

the so called *memory effect* in which the final residues keep a memory on the isotopic composition of its projectile, i.e. the isotopic distributions of fragments produced by the more neutron-rich  $^{124}\text{Sn}$  projectiles are shifted towards more neutron rich isotopes than in the case of  $^{112}\text{Sn}$  projectiles. The lighter residues, produced consequently after long evaporation chains and having high initial excitation energy, the memory is gradually reduced during the evaporation steps, and the mean neutron numbers shift towards the evaporation attractor line [Cha98]. Fig. 4.10 also exhibits the mean  $N/Z$ -ratio obtained from the EPAX predictions which shows good agreement with the experimental data in both reactions.

However, it has been shown [SRBE02, HSR<sup>+</sup>08] that the mean  $\langle N \rangle/Z$  ratio of the lightest residues produced in more violent collisions preserves a sensitivity to the  $N/Z$  of the initial system even at the end of the evaporation cascade. This gave rise to a method called the isotopic thermometer [SRBE02] for determining the excitation energy at the beginning of the evaporation cascade from the neutron excess observed in the isotopic distributions of the lightest final residues. Applying the method one could determine the so-called freeze-out

temperature, which corresponds to the stage in which the pre-fragments start to cool down by means of a sequential evaporation of nucleons and light clusters. An agreement with the data was found with the freeze-out temperature value of 5 to 6 MeV [SRBE02, HSR<sup>+</sup>08]. Please note, that due to different experimental cuts, these lightest residues have not been fully measured in the present work and are thus not shown in the Fig. 4.10. Following this line, one can also investigate correlations between the fragment isotopic content and kinematical properties, trying to get a deeper insight into the reaction path and to improve the understanding of the underlying mechanisms. This topic is treated in chapter 6.

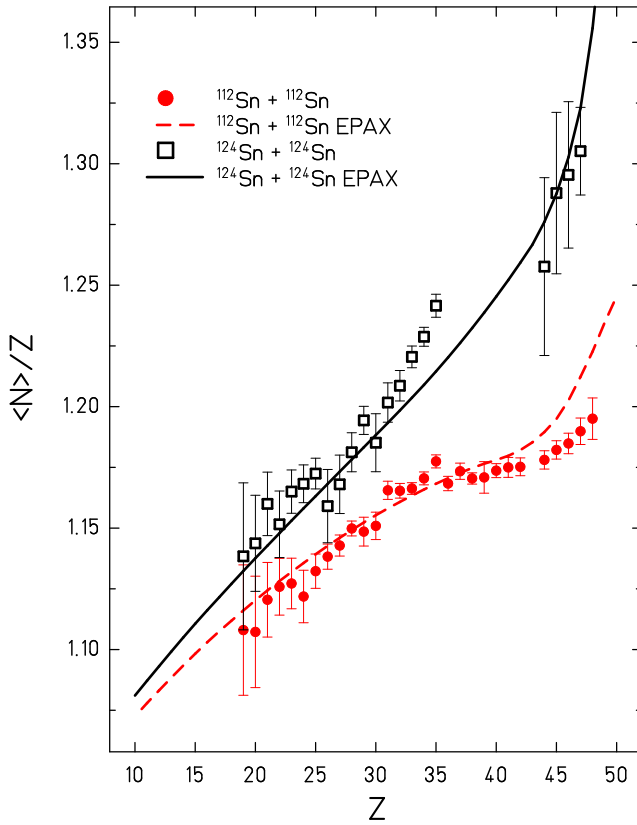


Figure 4.10: Mean neutron-to-proton ratio found in the isotopic distributions of  $^{112}\text{Sn} + ^{112}\text{Sn}$  and in  $^{124}\text{Sn} + ^{124}\text{Sn}$  at  $1\text{-}A$  GeV. Dashed lines represent the prediction of EPAX [SB00] for  $^{112}\text{Sn} + ^{112}\text{Sn}$  and solid lines for  $^{124}\text{Sn} + ^{124}\text{Sn}$ .



# Chapter 5

## Theoretical models

### 5.1 Projectile fragmentation in non-central heavy-ion collisions

Non-central collisions between heavy-ions have been often considered as a two-stage process. In the first collision stage, the thermalization of the excitation energy in the intrinsic degrees of freedom is established, and the equilibrated prefragment is formed. In the second stage the resulting equilibrated system de-excites by the evaporation of neutrons, protons and light nuclei as well as by fission and emission of gamma rays. This division is based on the physical nature of the interaction. The first stage involves hard collisions between nucleons which take place in a rather short time  $10^{-22}$  s. This stage is clearly a dynamical process by its nature, having key emphasis on the velocities of the interactive pieces and on the geometry which is governed by the impact parameter and the sizes of the nuclei. The second stage of the fragmentation process, the ablation, is more statistical by its nature meaning that there are several decay channels each having finite probability to occur. Particle emission times may be as long as  $10^{-16}$  s.

In case of mid-peripheral collisions, an additional stage - break-up stage, can occur. If the excitation energy acquired during the first, collision, stage is high enough, the nucleus can enter the spinodal region [CCR04] characterized by negative incompressibility. In this region, an increase in the system volume due to expansion is connected with the increase in pressure, and, consequently, any local fluctuation in density is strongly amplified leading to a mixed phase consisting of droplets represented by a small amount of light nuclei at normal nuclear density, and the nuclear gas represented by individual nucleons. The

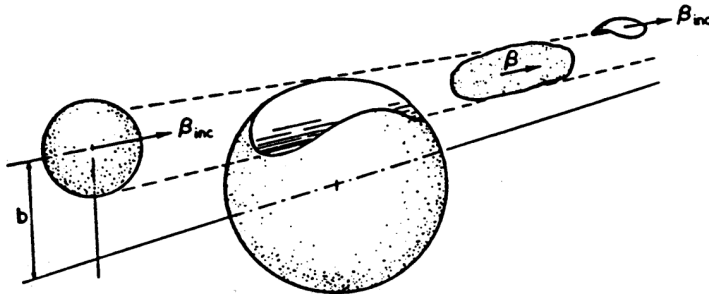


Figure 5.1: Schematic view of a relativistic heavy-ion collision: a neon nucleus collides with an incident velocity  $\beta_{inc}$  on the uranium nucleus in the laboratory frame with an impact parameter 5 fm. The swept-out nucleons from the projectile and target are called the fireball, and their center of mass has the velocity  $\beta$  in the laboratory frame. The figure is reprinted from Ref. [WGJ<sup>+</sup>76].

fragments formed in this process undergo de-excitation process and cool down. In the following, these different stages will be discussed in more details.

## 5.2 Collision stage

One of the first models describing the collision stage of the relativistic heavy-ion collisions is abrasion model introduced by Bowman, Swiatecki and Tsang [BST73]. It is based on the following very simple idea: when two relativistic heavy ions pass each other so closely that part of their volumes overlap, the elements in the overlapping volume are sharply scraped off (abrasion). The number of abraded nucleons is proportional to the volume of the overlap region. In this overlap zone, also called as the participant zone or the fireball, many nucleon-nucleon collisions take place. Due to high relative velocity of the reaction partners, the non-overlapping projectile matter, also called as the spectator matter, continues its path essentially undisturbed. Schematic view of the abrasion process is shown in Fig. 5.1. The geometrical abrasion model is based on the equation describing the probability of finding a number of nucleon-nucleon collision in the overlap of projectile and target densities when they pass at a distance  $b$  from each other. It can be calculated by a numerical integration of the overlap volume [LL90] or by using an approximate analytical formula [GGM<sup>+</sup>77]. In addition to the impact parameter, this model needs as an input the probability for individual nucleon-nucleon collision, namely the nucleon-nucleon cross section ( $\sigma_{NN}$ ).

The excitation energy induced to the prefragment during the abrasion can be easily recognized as one of the key parameters describing the projectile fragmentation process. Unfortunately this parameter has proved to be very difficult to determine experimentally. In the original geometrical concept of the abrasion model, the excitation energy of the prefragment is given by the excess of the surface of the deformed prefragment with respect to a sphere of equal volume [BST73, GGM<sup>+</sup>77]. Predictive accuracy of the abrasion-ablation models has been mainly hampered by the lack of realistic estimate of the prefragment excitation energy. Various improvements were developed like the use realistic nuclear-matter distributions [MS83], deduced from the droplet model [MS74] including the diffuseness.

Further on the abrasion-ablation model was formulated quantum mechanically by Hüfner [HSS75] who based his calculations on the Glauber multiple scattering theory [19559, GM70]. Beside the somewhat successful description on the fragmentation cross-sections this model deviates from the original ideas of Bowman *et al.* in the calculation of the projectile excitation energy by taking in account the additional amount of excitation energy induced by the nucleons of the abrasion zone scattering into the prefragments and depositing part of their kinetic energy. This idea was further considered by the authors who called it as *frictional spectator interaction* (FSI) [ODR79] which includes the excitation energy induced by means of friction between the abraded nucleons and the spectator, as the name suggests. These models with the improvements on determining excitation energy became known as the extended abrasion models.

In the abrasion-ablation model developed by Gaimard and Schmidt [GS91] the excitation energy induced to the prefragment by abrasion was treated in the frame of the statistical hole-energy model where the excitation energy is the sum of the energy levels freed by abraded nucleons. This model suggests an average excitation energy around 13 MeV per created hole. This was the first time the excitation energy was treated on the basis of essential, quantum-mechanical, properties of the nucleons in the nucleus.

Final-state interactions, induced by the particles emitted from the hot fireball zone, proposed new problems with the division of the nucleons into participants and spectators. Not only FSI changes the fragment's excitation energy, but it may also influence the ionic charge and mass by abrading other nucleons in the prefragment zone. There occurred deviations among the predictions obtained from the calculations which were attributed to the estimation of excitation energy of the prefragments [Har92, SBC<sup>+</sup>93, Car95]. These publications report a need to much higher excitation energy due to abrasion than 5 to 15 MeV per abraded nucleon reported earlier [HSS75, GS91]. Harvey [Har92] reported the need of 25 MeV per abraded nucleon to reproduce the data with his own Monte-Carlo simulation code [HCLC89].

Schmidt *et al.* [SBC<sup>+</sup>93] developed a now called isospin-thermometer method to determine the excitation energy induced in the heaviest elements produced in very peripheral collisions of  $^{197}\text{Au}$  (1.4 GeV) + Al. This method relates the loss of neutron excess observed in the isotopic distributions of the produced elements with the excitation energy at the beginning of the evaporation cascade. The average value of excitation energy, obtained by this study, lays around 27 MeV per abraded nucleon. Similar value was reported by Hubele *et al.* [HKL<sup>+</sup>92].

There was also a method developed to determine the excitation energy from the experimental data, without relying on a reaction model [CKP94]. The asymptotic value in this study for the excitation energy was found to be  $E_x/A = 23$  MeV.

In last decades, due to the development of microprocessors, it became possible to use also the so-called semi-classical models. The operation of the existing codes is based on various different principles like the Chapman-Enskog method with its correction on the viscous fluid dynamics, nuclear cascade models like ISABEL [YF79], nuclear cascade models with a mean field like the Boltzmann-Uehling-Uhlenbeck (BUU) [BG88], Vlasov-Uehling-Uhlenbeck (VUU) [UU33] or Landau-Vlasov (LV) [GRS<sup>+</sup>87] approaches, molecular dynamics approaches which consider each particle-particle interaction separately, like the Quantum Molecular Dynamics (QMD) [APB<sup>+</sup>88] approach or an antisymmetrized version of the QMD, called AMD [OHMO92]. These codes could be used to obtain a more accurate description of the abrasion of nucleons and deposition of energy occurring in the first step of heavy ion collision where we face a dynamical non-equilibrium system.

In the last 25 years transport models have been a successful tool for the theoretical investigation of heavy-ion collisions. At present very different multifragmentation models exist, a fact which reflects the diversity of this phenomenon.

### 5.3 Break-up stage

As already mentioned above, if excitation energy introduced in the collision stage is high enough, i.e. larger than 3 MeV per nucleon [BBI<sup>+</sup>95], the projectile remnant can disintegrate into several pieces. This is often referred as break-up or multifragmentation process. Such high excitation energies, leading to multifragmentation, are expected to occur in more central collisions where higher compression values and nuclear temperatures are reached. The modeling of the multifragmentation has been developed by Bondorf *et al.* [BBI<sup>+</sup>95] to offer a treatment in the de-excitation phase of the prefragments obtained after abrasion in a heavy-ion collision.

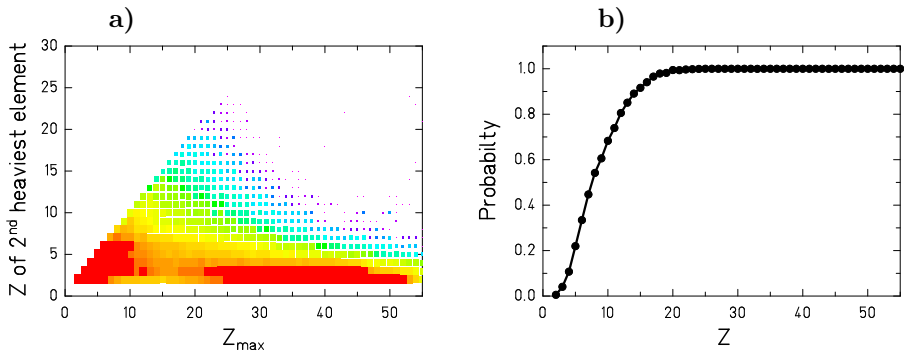


Figure 5.2: Second largest atomic number as a function of the largest atomic number  $Z_{max}$  observed in an ALADIN experiment for the reaction  $^{136}\text{Xe}$  ( $600\text{-}A$  MeV) + Al (panel a). Colors depict the relative cross-sections, in logarithmic scale. Panel b shows the probability of observed fragment with nuclear charge  $Z$  being the heaviest fragment produced in the event.

Multifragmentation has been observed in full acceptance experiments, like the ones performed with the large-acceptance spectrometer ALADIN, where higher multiplicities of relatively heavy products are seen. The ALADIN collaboration mostly exploits this information to study phase-transition effects in nuclear matter. Also the centrality, i.e. the impact parameter, in relativistic nucleus-nucleus collisions may be obtained through the monotonous correlation between multiplicity and impact parameter. The multiplicity dependence of the measured cross section is interpreted as an impact-parameter dependence of the geometrical reaction cross section. The reliability of this method has been verified at lower and higher energies [CDG<sup>+</sup>90].

In Fig. 5.2 the products of the reaction  $^{136}\text{Xe}$  ( $600\text{-}A$  MeV) + Al, detected in the ALADIN experiment, are shown in a two-dimensional cluster plot which maps the number of events in correspondence of which the two heaviest fragments were produced. The events populate the region limited by the lines  $Z_{max2}=Z_{max}$  and  $Z_{max2}=54-Z_{max}$ . The upper corner represents the fission events, which produces fragments of intermediate mass. The events on the flat distribution are presumably produced in peripheral collisions leading to a single large prefragment which evaporate only few light clusters. On the left corner one can see the multifragmentation products which have also undergone an evaporation stage as their final process. Fig. 5.2 panel b shows the probability of observed fragment with nuclear charge  $Z$  being the heaviest fragment produced in the event. Single protons and neutrons are excluded from these plots. In conclusion, all the collected data seem to indicate that there are several clear evidences of a transition between fragmentation (with one dominant large fragment) and multifragmentation (forming more than one intermediate

mass fragments with similar size). These signatures seem to indicate that the transition from a purely two-step fragmentation model to a multifragmentation picture is not sharp but continuous.

The second point that has been deduced from a number of observations from the full-acceptance experiments [OABB<sup>+</sup>91, HKA<sup>+</sup>91, KABB<sup>+</sup>93], is the invariance of isotopic composition of the (multi-)fragmentation products of excited spectator nuclei with respect to the chosen target. The mean number of projectile fragments produced as well as other observables characterizing the populated partition space were found to be the same for different targets, ranging from carbon to lead. The observed target invariance hence suggests that statistical equilibrium is attained prior to the fragmentation stages of the reaction [SKW<sup>+</sup>96].

## 5.4 Ablation stage

Excited projectile remnants finally de-excite via sequential evaporation of nucleons and light nuclei, and in case of heavy nuclei, fission. The probability of evaporating one or another particle is usually calculated using either Weisskopf-Ewing [WE40] or Hauser-Feschbach model [HF52]. While in the former a direct consideration of angular momentum and parity is neglected, in the latter approach they are explicitly taken into account. Many different de-excitation codes based on these two approaches have been developed. They mostly differ according to different descriptions of the physics concepts involved, e.g. level density, nuclear potential, nuclear viscosity or number of considered decay channels.

Among different available models, for the study performed in the present work we have chosen the abrasion-ablation model ABRABLA [GS91] and BUU model [BG88].

## Chapter 6

# Data interpretation

In this chapter, it will be demonstrated, with the help of more or less sophisticated numerical statistical-model, ABRABLA [GS91], how the longitudinal velocity distributions of the final residues, containing the kinematic as well as the production cross section information, as presented in chapter 4, can be used to identify and quantify the relative shares of the decay processes, binary decay and multifragmentation, which lead to the production of intermediate-mass fragments. The velocity spectra as a function of residue mass, which we get at the FRS is a rather complex information. As discussed earlier the measured mass is the one after the de-excitation process. To be able to interpret the obtained data correctly one has to take into account these processes in the most realistic way. One simple way to test the validity of the assumptions made on the course of de-excitation process is to try to reproduce the data with a simulation code. For this task a modern version of the abrasion-ablation model, ABRABLA [GS91], was chosen. ABRABLA is a statistical model consisting from two parts; ABRA-part describing the abrasion and the ABLA-part [JdJC<sup>+</sup>98, KRS09], that contains the treatment of de-excitation. Other possible choice for this task would have been the SMM code [BBI<sup>+</sup>95], which is able to treat multifragmentation in a way which is consistent to a rather high degree with the available data. Another often-used model for the de-excitation stage, is the sequential-emission code GEMINI [CMW<sup>+</sup>88], but it is not suitable for the use in the present work since the data includes also mid-peripheral collisions, where higher excitation energies occur, and the multifragmentation becomes energetically possible in both systems [BMP<sup>+</sup>91, BBB<sup>+</sup>93].

The de-excitation stage is well described in ABRABLA and it also contains all the physics which is behind the broadening of the velocity distribution in abrasion and multifragmentation. Thus, the shapes of the Gaussian velocity clouds from abrasion-evaporation and from multifragmentation are quantitatively pre-

dicted. It models in a realistic way the Coulomb repulsion in binary decay and the shapes of the Coulomb spheres of the intermediate-mass fragments (IMF) are quantitatively predicted on the basis of well defined physics.

The objective is to show quantitatively that within the assumptions on the course of de-excitation, the simulated global distribution of produced residues can lead to very similar shapes to what is actually measured in the FRS. In Fig. 6.1 results from the simulation code ABRABLA are shown for the reactions  $^{124}\text{Sn} + ^{124}\text{Sn}$  (left panels) and for  $^{112}\text{Sn} + ^{112}\text{Sn}$  (right panels). The simulations include the cut due to FRS limited angular acceptance. The expected spectra from different reaction processes are shown separately. In the upper row, panels (a) and (e), the longitudinal velocity of the residues, that have undergone sequential evaporation, is plotted as a function residue mass. The residues very close to the projectile are produced through this process. The sequential evaporation starts to be less dominant process for the residues with less than about the half of projectile mass. On the second row, panels (b) and (f), the residues produced in the multifragmentation process are shown. Multifragmentation is the dominant process for the residues starting with slightly more than about the half of projectile mass. The change from evaporation to multifragmentation being the dominant process is gradual. On the third row, panels (c) and (g), the residues produced in symmetric binary decays (symmetric fission) are shown. This process is giving contribution to the velocity distributions, especially due to population of extreme velocities, but in terms of cross section, this process never becomes more abundant than the multifragmentation process in case of the studied reactions. In the last row, panels (d) and (h), the sum of all three processes is shown. By comparing the prediction i.e. the sum of all the residues, shown in panel d and h, to the plot corresponding to the experimental data presented in Fig. 4.3, in a general way it seems that the predicted broadening of the velocity distributions is rather close to the data. One may also observe that the range of reaction products from the lightest fragments up to the projectile is continuously populated. If looked in detail, it can be also noticed that the ABRABLA calculation reproduces correctly the mean values ( $\langle N \rangle / Z$ -ratio) of the isotopic distributions and the production cross sections of the residues in both measured systems.

ABRABLA also closely reproduces the observed behavior of the mean value of the longitudinal velocity distributions in the studied systems, however, this behavior was adjusted to the observed features from previous experiments by a parametrization. In the next sections the kinematical aspects, extracted from the experimental data, are analyzed in more detailed way with the help of ABRABLA predictions providing the link to the underlying physical processes.

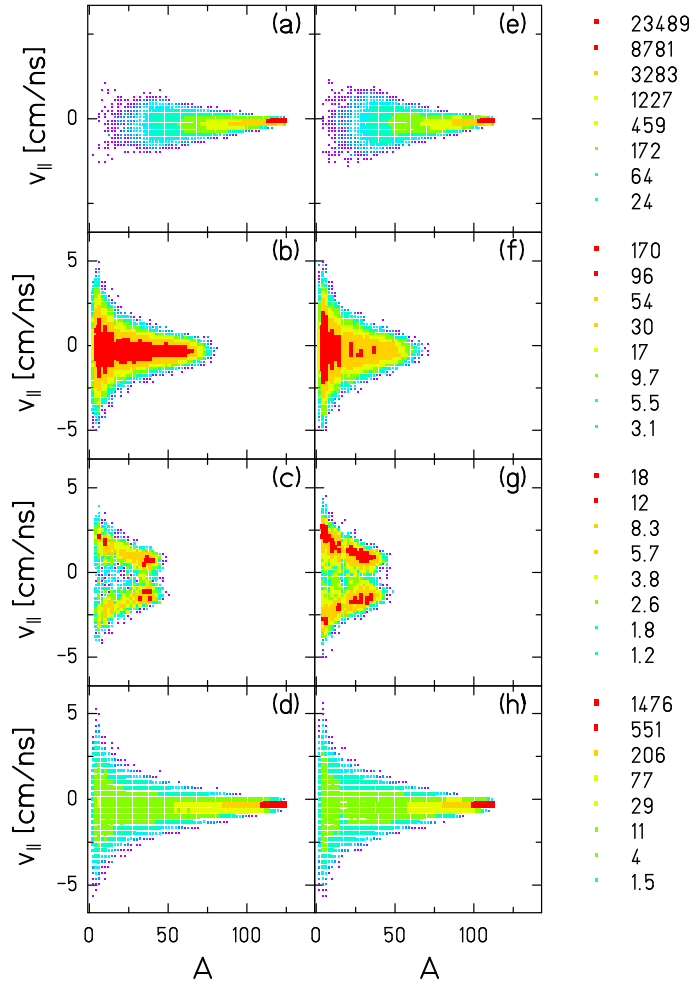


Figure 6.1: Longitudinal velocity distribution in the beam frame of the various reaction products (see text for details) according to ABRABLA [GS91] simulation, as a function of mass number in reactions  $^{124}\text{Sn} + ^{124}\text{Sn}$  (left panels) and  $^{112}\text{Sn} + ^{112}\text{Sn}$  (right panels). See the text for details. Both reactions have the initial projectile energy of  $1 \cdot A$  GeV. In total one million reactions were simulated to accumulate the spectra. The cut due to the FRS angular acceptance is applied [BPCS02].

## 6.1 Asymmetry of the measured velocity distributions

According to the prediction of ABRABLA presented in Fig. 6.1, we find that the velocity distributions of final residues in the light mass region are in fact superposition of two distributions: a Gaussian shaped cloud of multifragments and a double-humped distribution, from the two components of the Coulomb sphere, which fall into the FRS angular acceptance. This is best illustrated in Fig. 6.2 where the longitudinal velocity distribution in the beam frame of three different fragments produced in the reaction  $^{136}\text{Xe}(1.4 \text{ GeV}) + \text{p}$  [NSTG<sup>+</sup>07] are shown. The shape of the longitudinal velocity spectra shows clearly three peaks which can be understood as a superposition of the two main production mechanisms: multifragmentation and binary decay. As it can be seen from the data measured in the present work, presented in Figs. 4.1 and 4.2, representing the velocity distributions in a wide range of final residue mass, the triple peak structure is not clearly seen in any of the distributions. Although the  $^{136}\text{Xe}$  beam has the same energy and is in the same mass range than the projectiles studied in the present work, the excitation energy induced by the spallation process is much lower than with a tin target nucleus. The geometry of the interaction scheme is also very different. The direct consequence is that multifragmentation is less likely to occur in spallation than in the collision with heavy target. Nevertheless, very light fragments (IMFs) are observed for which the binary decay, with a strong Coulomb repulsion at play, are then the dominant production mechanisms. Due to the higher excitation energies achieved in the reactions studied in the present work, the binary peaks are almost completely superposed with the abundant multifragmentation products in the velocity spectrum. The triple peak structure, suggested by the model, is not obviously extractable from the data. It has also been found in other FRS experiments studying heavy systems [Hen05, HSR<sup>+</sup>08], performed with the same projectile energy 1.4 GeV, that the multifragmentation gives much larger component than the binary decay for the intermediate mass fragments.

As illustrated earlier in section 3.2.4 the data could be reproduced sufficiently well with the Eq. 3.15 i.e. with just one Gaussian peak with exponential tail. Even with the knowledge about the relative position of the binary peaks with respect to each other, given by the well known Coulomb force, and with the known cut due to experimental conditions (see section 3.3.2), the fit routine could not extract the triple peaked structure in the longitudinal velocity distributions of IMFs. On the other hand the measured data doesn't contradict this picture but on the contrary it supports it by showing a slight but quantifiable asymmetry. To illustrate the situation more clearly, the measured longitudinal velocity distribution of  $^{31}\text{P}$ , was fitted with three Gaussians corresponding to the two main de-excitation processes: the binary decay (two Gaussians) and multifragmentation (one Gaussian). The result of this procedure is shown in

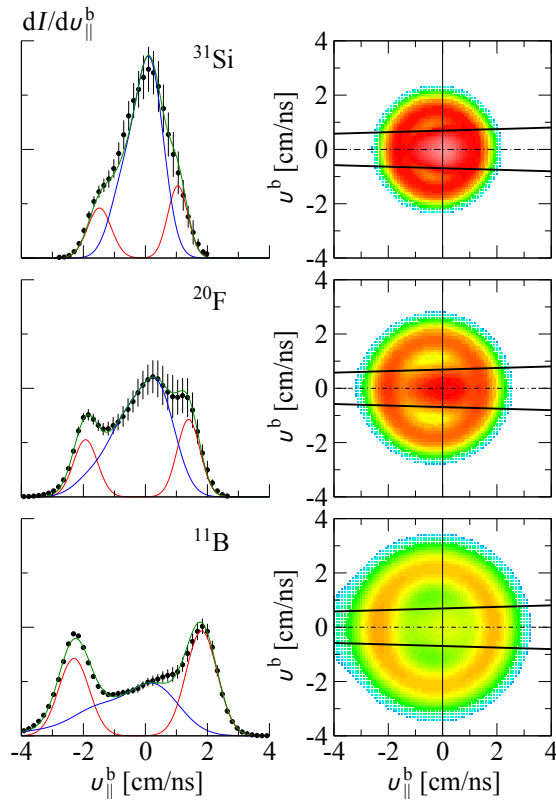


Figure 6.2: Longitudinal velocity distribution in the beam frame of three different fragments produced in the reaction  $^{136}\text{Xe}(1\cdot A \text{ GeV}) + \text{p}$ . The corresponding (expected) global distributions in the  $(v_{\parallel}; v_{\perp})$  plane and the limits of the FRS acceptance are displayed on the right. Taken from [NSTG<sup>+</sup>07].

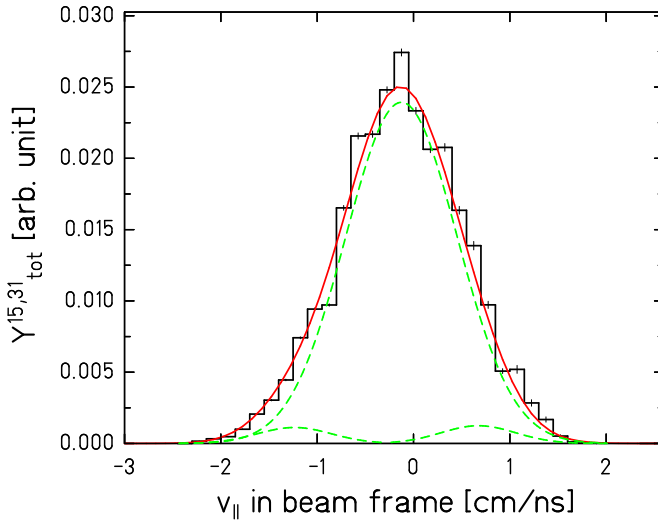


Figure 6.3: Longitudinal velocity distribution of fragment  $^{31}\text{P}$  (histogram) together with the 3 Gaussian fit functions, revised with ABRABLA calculation (green), and a sum of them (red) reproducing the data.

Fig. 6.3. The red line shows the resulting fit function as sum of the three Gaussians (green). Fitting routine was given the relative sizes i.e. the yields of the fragments emerging from the two processes as an input from ABRABLA calculation. In addition to this the relative separation of the two binary components, under the influence of the FRS angular acceptance, is predicted correctly by ABRABLA and was used as input to the fitting routine. The mean values of all three Gaussians were left undetermined as well as the absolute yields of the components. This study illustrates that the measured data can be reproduced as a superposition of these two processes.

The idea of fragments of same size emerging from two different kind of reactions was found to be supported by the experimental evidence obtained from the full acceptance experiments (see Fig. 5.2). The FRS data reveal that these two groups have different mean velocities. They are characterized by different shapes of their velocity distributions under the angular cut of the FRS: a single humped (Gaussian) component centered at slightly slower than the beam velocity and a double humped (two Gaussians) component centered slightly at the slower velocity with respect to the larger single Gaussian component, leading into asymmetric sum of velocity distributions which we observe. The limited angular acceptance of the FRS turns to be an important tool to disentangle the different reaction mechanisms, as was found in the previous FRS experiments

[NSB<sup>+</sup>04, NSTG<sup>+</sup>07].

A very asymmetric binary decay populates the same mass range of IMFs (masses up to  $\sim 35$ ) as multifragmentation. However, the impact-parameter range is very different: Binary decay (also very asymmetric one) comes from much more peripheral collisions than multifragmentation. Therefore, the velocity spectra in the IMF range, measured at the FRS, is a mixture of two processes. The FRS cannot measure the multiplicity of an event. But the FRS still provides an observable, which is able to disentangle these two contributions: Multifragmentation, which is dominated by the Fermi momenta in the abrasion, is characterized by a Gaussian (three-dimensional) velocity cloud, while IMFs from binary decay have received a push from the heavier remnant due Coulomb repulsion, and thus are situated in a Coulomb shell. Thus, the velocity distributions of the FRS can be considered as a kind of multiplicity filter. A more detailed discussion on these aspects of the FRS data is given in reference [NSTG11].

So far we have learned that the observed asymmetry in the longitudinal velocity distributions is due to two different processes and also we know that these processes occur in different impact parameter ranges. This gives reason to believe that the asymmetry i.e. the relative shift between the mean values of the two components, is likely to be a remnant from the abrasion stage, which we know is strongly governed by the impact parameter. In the next section this aspect is discussed in more detail.

## 6.2 Mean longitudinal velocity

The sequential decay of the compound nucleus formed after the abrasion stage affects obviously the observed fragmentation patterns and also the width of the fragment velocity distributions, but do not so much affect the mean value. In fact the mean value is completely governed by the formed prefragment because the sequential emission in the second stage is forward-backward symmetric along the collision axis and thus is not capable of affecting the mean longitudinal velocity of the emitting source with biased recoil effects [dJIS97].

As has already been mentioned in the beginning of this chapter, the current understanding of the development of excitation energy relies on the solid basis of the friction model. However there has been less focus on the impact of friction to the spectator velocities. This is partly due to lack of precise enough measurements.

The most important advantage of the full-acceptance set-ups is the possibility of exclusive measurements i.e. the detection of all fragments produced within

one reaction event. Some full-acceptance spectrometers, like ALADIN, are capable of measuring the full 3-dimensional velocity distribution of the produced fragments. This means that the IMFs emerging from the binary splits populate the so-called Coulomb sphere which is fully observed. The resulting observed velocity distributions do not necessarily reveal any unique characteristics that could be used to distinguish them from the multifragmentation products unless a multiplicity filter applied. The velocity measurements just for the multifragment products or for the binary decay products, in full acceptance experiments, could be obtained by applying a multiplicity filter for example by putting conditions on the velocities based on the areas seen in Fig. 5.2. However, the disadvantage of such experiments is the resolution which may not allow the observation of the small fluctuations in the mean values of the velocity distributions.

As it was seen in Fig. 4.5, for more central collisions the velocity deviates from the universal friction behavior: a re-acceleration process adds up. This re-acceleration seems to grow with a much higher power of the final mass (2 or higher). Therefore, it is not noticed in very peripheral collisions. However, it becomes dominant for more central collisions. The re-acceleration phenomenon becomes stronger with higher beam energy and with more massive systems [Hen05]. Eventually larger than beam velocities are also observed experimentally in heavy systems like  $^{238}\text{U} + \text{Ti}$  [REP<sup>+</sup>03] and in  $^{238}\text{U} + \text{Pb}$  [E<sup>+</sup>99] both at the projectile energy of  $1.4 \text{ GeV}$  as shown in Fig. 1.2.

This behavior is qualitatively similar to the "spectators response to the participant blast" postulated by Shi *et al.* [SDL01]. The idea for this blast stemmed from the flow analysis of the fireball. The so-called elliptical-flow pattern of the participant matter was found to be affected (shadowed) by the presence of cold spectators [Dan00, YHG<sup>+</sup>09]. When nucleons are de-accelerated in the participant region, the longitudinal kinetic energy associated with the initial colliding nuclei is converted into thermal and potential compression energy. In a subsequent rapid expansion (or explosion), collective transverse energy develops [Dan00, YHG<sup>+</sup>09], and many particles from the participant region get emitted into transverse directions. The particles emitted towards the reaction plane can encounter cold spectator pieces, and hence they get redirected. In contrast, the particles emitted essentially perpendicular to the reaction plane are largely unhindered by the spectators. Thus, for beam energies leading to a rapid expansion in the vicinity of the spectators, elliptical flow, directed out of the reaction plane (squeeze-out), is expected. This squeeze-out is related to the pace at which the expansion develops. The flow pattern of light particles shows lower intensities in the directions of the spectators. This would mean that the hottest (fastest) particles from the explosion of the fireball hit the spectators and are absorbed. This leads to an anisotropy in the velocity distribution of the spectator due to the geometry. In other words the velocities would be enhanced in the longitudinal direction leading to the observed re-acceleration.

The shadowing effect has been seen also by looking at the experimental data directly. Influence of the spectator matter to fireball explosion has been reported in Ref. [WMO<sup>+</sup>00]. Shadowing is deduced by comparing the in-plane pion emission to the yield of pions emitted perpendicular to the reaction plane. The latter pions are expected to be much less affected by shadowing or re-scattering by spectator matter and hence provide a nearly undisturbed view onto the pion source. In near-central collisions the spectator fragments are small and hence shadowing effects are strongly reduced. This has been also seen in the pion flows [WMO<sup>+</sup>00].

The influence of the shadowing effect on the spectator velocities has been studied with the BUU code [SDL01] and the code's predictions have been tested against the experimental data before [Hen05]. This study has led to the conclusion that re-acceleration reaches down to lower beam velocities and to less massive systems. There is a dependence on the size of the target nuclei to the re-acceleration of the fragmentation residues. In this study the comparison between the predictions and the experimental data, obtained from FRS, was based on the idea of one-to-one correspondence between the impact parameter and the final residue mass. This may have led to ambiguous conclusion. Also, perhaps partly due to this reason, the prediction not only failed to reproduce the experimentally observed re-acceleration of the lighter residues, but there was no correspondence found even in the vicinity of the projectile masses where only the deceleration, which is attributed to the friction process, is seen.

In the pioneering calculations for the spectator velocity [SDL01], consequently the same system,  $^{124}\text{Sn} + ^{124}\text{Sn}$ , as in the present work was studied, except with slightly smaller projectile energy of  $800 \cdot A$  MeV. Calculations were also restricted to more central collisions  $b \leq 8$  fm. The effect of NN cross section and momentum dependence was found to enhance the spectator forward velocities. In case of small impact parameters in a heavy system, spectators were found to be capable of emerging from the reaction with a higher net average momentum per nucleon than the original momentum. These larger than beam velocities are also observed experimentally in heavy systems [REP<sup>+</sup>03, E<sup>+</sup>99] at the projectile energy of  $1 \cdot A$  GeV.

Driven by these promising results, the same BUU code was used to obtain the spectator momentum starting from the most peripheral collisions ( $b \approx 14$  fm) of  $^{124}\text{Sn} + ^{124}\text{Sn}$  and  $^{112}\text{Sn} + ^{112}\text{Sn}$  systems that were also studied experimentally. BUU code is only used to calculate the collision stage of the reaction, which is not directly observable in the experiments. The residues observed in the experiment have undergone the statistical decay. Therefore, the result of BUU, presented in the impact parameters space, are coupled to the ABRABLA calculations in order to account for the decay stage and to provide a comparison to the measured data, presented as function of final residue mass.

In the following chapter the code (section 7.1) and its predictions (section 7.1.1) will be presented in more detail. In section 7.2 the coupling of the two codes is introduced and the results obtained this way are compared to experimental results.

# Chapter 7

## Calculations

As mentioned also in the previous chapter, the theoretical predictions obtained through transport models have been a successful tool providing a link to many experimental observables arising for example in heavy ion collisions. With the help of simulations the intuitive understanding of the physical processes is possible.

In this chapter the BUU transport model based on the Boltzmann-Uehling-Uhlenbeck equation is introduced and the calculations of the prefragment velocity, in the reactions  $^{124}\text{Sn} + ^{124}\text{Sn}$  and  $^{112}\text{Sn} + ^{112}\text{Sn}$ , after the interaction state are presented. We consider some of the parameters of the model and their impact on the prefragment velocity in a similar manner that was performed in the work of Shi *et al.* [SDL01], and expanding the studied range of impact parameters to include very peripheral collisions.

### 7.1 Boltzmann-Uehling-Uhlenbeck (BUU) transport model

The Boltzmann-Uehling-Uhlenbeck (BUU) formalism [BG88] calculates the time evolution of the colliding system using a self-consistent mean field. The code solves a set of coupled Boltzmann equations for particles in energetic heavy-ion reactions. The description of the code and physics within may be found in Refs. [Dan00, DB91, BDoPGB04].

In this approach the colliding system is described by one-body phase space distribution function  $f_i = f(\vec{r}, \vec{p}_1, t)$  where each particle have definite momen-

tum and energy. These particles move within the mean field (MF) produced by other particles. The time-evolution of the distribution function follows the equation:

$$\frac{\partial f_X}{\partial t} + \frac{\partial \epsilon_X}{\partial \mathbf{p}} \frac{\partial f_X}{\partial \mathbf{r}} - \frac{\partial \epsilon_X}{\partial \mathbf{r}} \frac{\partial f_X}{\partial \mathbf{p}} = \kappa_X^< (1 \mp f_X) - \kappa_X^> f_X. \quad (7.1)$$

The l.h.s of the equation the total time derivative of the distribution function which accounts for the changes in the distribution function due to the mean field. The collision integral in the r.h.s, takes into account the nuclear scattering inside the nuclear medium e.g changes on the distribution due to collisions. Factors  $\kappa^<$  and  $\kappa^>$  on the r.h.s. of Eq. 7.1 are the feeding and removal rates respectively. The occupation  $f_X$  and vacancy  $1 \mp f_X$  takes in to account the Pauli blocking since the colliding systems consist of nucleons for which the Pauli principle states that no nucleon can scatter into phase space already occupied by another nucleon. This modification was added to the equation by Uehling and Uhlenbeck [UU33].

The single-particle energies  $\epsilon_X$  are variational derivatives of the total system energy with respect to the phase-space distribution. In the calculations a strongly momentum-dependent (MD) and momentum-independent (MI) mean fields are utilized. In the case of the MI mean field, the energy density in the system is

$$e = \sum_X g_X \int \frac{d\mathbf{p}}{(2\pi)^3} f_X(\mathbf{p}) \sqrt{p^2 + m_X^2(\rho_s)} + \int_0^{\rho_s} d\rho'_s U(\rho'_s) - \rho_s U(\rho_s) \quad (7.2)$$

where  $m_X(\rho_s) = m_X + A_X U(\rho_s)$ ,  $A_X$  is baryon number and  $\rho_s$  is scalar baryon density. The single-particle energy is then

$$e_X(p, \rho_s) = \sqrt{p^2 + m_X^2(\rho_s)} \quad (7.3)$$

Basic ingredients for the equation 7.1 are the mean field  $U$  and the nucleus-nucleus cross section  $\sigma_{NN}$ . In these calculations, as well as in many other calculations, the Skyrme-type mean field is used

$$U(\rho_s) = \frac{-a\left(\frac{\rho_s}{\rho_0}\right) + b\left(\frac{\rho_s}{\rho_0}\right)^\nu}{1 + \left(\frac{\rho_s}{2.5\rho_0}\right)^{\nu-1}}, \quad (7.4)$$

where  $\rho_0$  is the normal density and  $a$ ,  $b$  and  $\nu$  are parameters. The parameters for the mean fields used in the calculations within the present work are given in Tab. 7.1.

In the calculations with MD mean fields, the energy density is represented in the local baryon frame as

$$e = \sum_X g_X \int \frac{d\mathbf{p}}{(2\pi)^3} f_X(\mathbf{p}) \left( m_x + \int_0^p dp' v_X^*(p', \rho) \right) + \int_0^{\rho_s} d\rho'_s U(\rho'_s). \quad (7.5)$$

The adopted form for  $U(\rho)$  is the same as in Eq. 7.4 and the local particle velocity is parametrized with

$$v_X^*(p', \rho) = \frac{p}{\sqrt{p^2 + \frac{m_X^2}{\left(1 + c \frac{m_N}{m_X} \frac{A_x(\rho, \rho_0)}{(1 + \lambda p^2/m_X^2)^2}\right)^2}}}. \quad (7.6)$$

With the above, the single-particle energy in the local frame is:

$$e_X(p, \rho_s) = m_x + \int_0^p dp' v_X^* + A_X \left[ \rho \left\langle \int_0^{p_1} dp' \frac{\partial v_X^*}{\partial \rho} \right\rangle + U(\rho) \right]. \quad (7.7)$$

The parameters for the MFs are given in Tab. 7.1. Detailed discussion on how to deduce the numerical values of these parameters, the initialization of nuclei and the lattice Hamiltonian method for integrating the equations, can be found in Ref. [Dan00].

EqS	$a$	$b$	$\nu$	$c$	$\lambda$	$m^*/m$	$K$
S	187.24	102.623	1.6340	-	-	0.98	200
SM	209.79	69.757	1.4623	0.6457	0.9546	0.70	200
H	121.258	52.102	2.4624	-	-	0.98	380
HM	122.785	20.427	2.7059	0.6457	0.9546	0.70	380

Table 7.1: Values for the parameters in the mean field used in the calculations. First three parameters  $a$ ,  $b$  and  $\nu$  refer to Eq. 7.4 and the next two to Eq. 7.6.  $m^*/m$  is the Landau effective mass in normal matter at Fermi momentum. The last column gives the incompressibility of nuclear matter.

An important ingredient for the calculations is the incompressibility  $K$  of nuclear matter. Simulations have been performed with two different incompressibilities, *hard*:  $K = 380$  MeV and *soft*:  $K = 200$  MeV. It refers to the curvature of the energy  $E$  of nuclear matter with respect to the density, at normal density,

$$K = 9\rho^2 \frac{\partial^2}{\partial \rho^2} \left( \frac{E}{A} \right) \Big|_{\rho=\rho_0}. \quad (7.8)$$

The incompressibility is an important quantity in astrophysics. In fact, the mechanism of supernova explosions is strongly depending on the value of  $K$  [SLM94]. Supernova models might not lead to explosions depending on the value of  $K$ . The central collisions of heavy nuclei are one of the few probes of this quantity in the laboratory. The sensitivity of reaction simulations to  $K$  stems from the fact that  $K$  affects pressures reached in the reactions and the pressure affects the collective flow. The effects of the pressure compete, though, with the effect of momentum dependence of single-particle energies encoded in Eqs. 7.6 and 7.7. Similar outcomes for observables may often be reached combining high

incompressibility with no momentum dependence in interactions as combining low incompressibility with strong momentum dependence [GBDG87].

An additional investigation with the model, was the influence of the values used as nucleon-nucleon cross section. Among other things this parameter determines the value of the mean-free-path  $\lambda$ . If  $\sigma_{NN}$  is reduced, the  $\lambda$  increases and the excitation energy decreases since we reduce the number of abraded particles. The increase in the  $\sigma_{NN}$  produces the opposite effect. Two types of cross sections were explored: the free cross sections and the cross-sections reduced in such a manner that their radii are limited by the inter-particle distance

$$\sigma = \sigma_0 \tanh(\sigma_{Free}/\sigma_0), \quad (7.9)$$

where  $\sigma_0 = \rho^{-2/3}$ . The reduction is only applied to the elastic cross sections, in order to maintain the detailed balance relations in the medium. The in-medium cross section is about 60% lower than the free cross section in case of the studied systems.

The simulations are carried out with the relativistic lattice Hamiltonian method together with Monte Carlo test-particle method, generating positions and momentum of particles in successive time steps. In order to have a good approximation of the exact continuous distribution function and to be able to obtain a variety of observables for reactions, the number of test particles per nucleon should be large enough. In case of large nucleus, this may require lots of CPU time.

The original code introduced here was not designed for delicate studies on the prefragment velocities, but certain modifications were needed to be done. With the unmodified version of the code, the prefragment velocities did not converge into beam velocity as a function of increasing impact parameter, but velocities were about 2% higher which is the same magnitude as the observed re-acceleration phenomena. The code was specifically tailored for these calculations to provide more accuracy on the velocities near the beam velocity [Dan09]. This was done by modifying the codes intrinsic frame of reference, where the calculations were performed, into the frame of projectile, when originally performed in the center of mass coordinate system of the target and projectile. This discrepancy was due to the fact that the velocities calculated in this reference frame are large compared to the observed fragments deviation from the beam velocity and the effect was lost in the relative numerical accuracy of the calculations.

In the following section the results of the calculations will be presented and the convergence to the beam velocity is observed at about impact parameter  $b \gtrsim 13$  fm. This is very intuitively and essential requirement, since if the impact parameter is increased to the point where there is no interaction between the projectile and target, then there should be no change in the projectile velocity.

### 7.1.1 Results from the BUU calculations

Calculations were performed for the  $^{112}\text{Sn} + ^{112}\text{Sn}$  and  $^{124}\text{Sn} + ^{124}\text{Sn}$  systems at 1.4 GeV. There were seven sets of calculations performed within the mid-peripheral and peripheral impact parameters ranging from  $b = 3.5$  fm to 14 fm. Each set of calculations had different parameters that are summarized in Tab. 7.2. The varied parameters were momentum dependence of mean field,

#	$^{124}\text{Sn}$	$^{112}\text{Sn}$	MO-DEP	FREE NN XS	SOFT $K$
1	x		x	x	x
2	x		x		x
3	x			x	x
4	x		x	x	
5		x	x	x	x
6		x	x		x
7		x		x	x

Table 7.2: Summary of the BUU calculations performed with different parameters.

incompressibility coefficient  $K$  and nucleon-nucleon cross section  $\sigma_{NN}$ . According to previous findings [Hen05, SDL01] also other parameters like the mass of the target nucleus and the beam energy have a strong influence. The influence of these two parameters however was not studied with the code but only the cases corresponding to the performed experiments were used. One additional set of calculations was performed to study the fluctuations in the results given by the code in the studied impact parameter range. This was performed with the parameters in the third set for  $^{124}\text{Sn}$  system, which were estimated to give largest fluctuations although the fluctuations are assumed to be rather independent of the parameters. For this study 12 calculations were performed for two impact parameters  $b=5.5$  and  $b=11.5$  to estimate the numerical uncertainty of the calculations.

We employed ensembles of 500 test particles per calculation and we followed the dynamical propagation of each ensemble for an elapsed time of 160 fm/c. At this late time, the projectile and target residues can be cleanly separated and the output quantities exhibit saturation. In the present work we adopt the original operational definition of spectator matter as introduced by Shi in Ref. [SDL01]. The nucleons are assigned to the projectile residue in a region where the density exceeds  $0.05\rho_0$  and in addition the nucleon must have center of mass velocity more than half that of the beam.

In Fig.7.1 time evolution of the propagation calculation is presented for mid-peripheral collision at impact parameter  $b=7$  fm in  $^{124}\text{Sn} + ^{124}\text{Sn}$  collision at 1.4 GeV obtained from BUU calculation. Each contour plot corresponds the

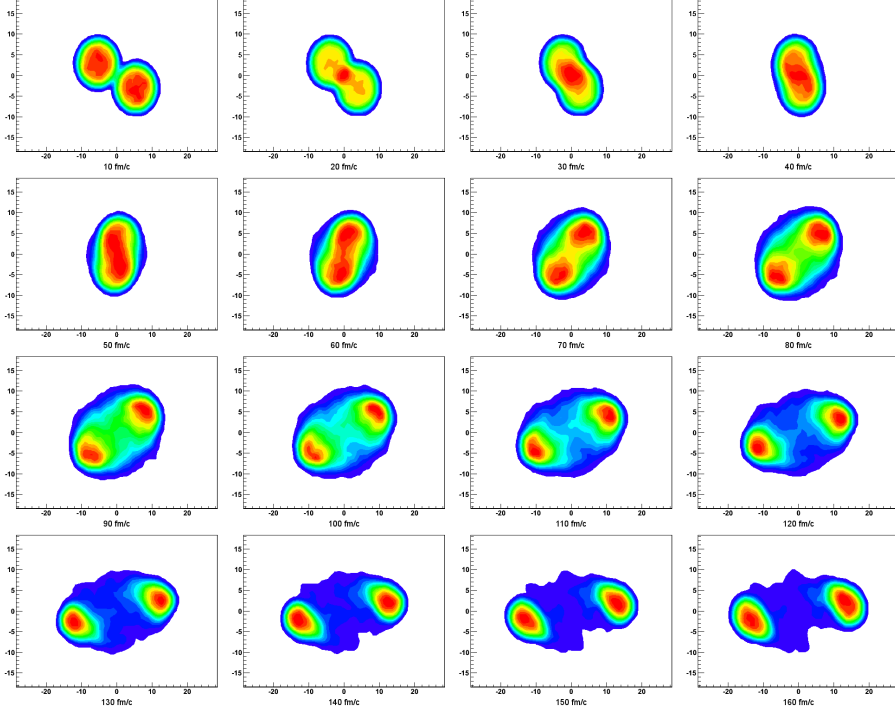


Figure 7.1: Contour plots of the system-frame baryon density at several time steps projected to the reaction plane in BUU simulation of  $^{124}\text{Sn} + ^{124}\text{Sn}$  at  $1\text{-}A$  GeV and  $b = 7$  fm. The time steps are written on each panel. Right bottom corner representing time 160 fm/c. The calculations have been carried out employing the soft momentum-dependent EOS. The contour lines for the densities correspond to the values, relative to the normal density.

systems baryon density projected on the reaction plane at different times from 10 fm/c to 160 fm/c with 10 fm/c steps between each panel starting from the top left corner. The times are written on each panel. The contour lines for the densities correspond to the values, relative to the normal density  $\rho_0$ .

Driven by these isodensity plots one can identify quite generally three main stages of the collision:

1. **the early collision phase** during the first  $\sim 50$  fm/c, compression occurs and the density in the central region can reach values around 1.2-1.3 times the normal density.
2. **the expansion phase** up to  $\sim 110$  fm/c, brings the system to a low-density state. During this time a rather significant reorganization in the

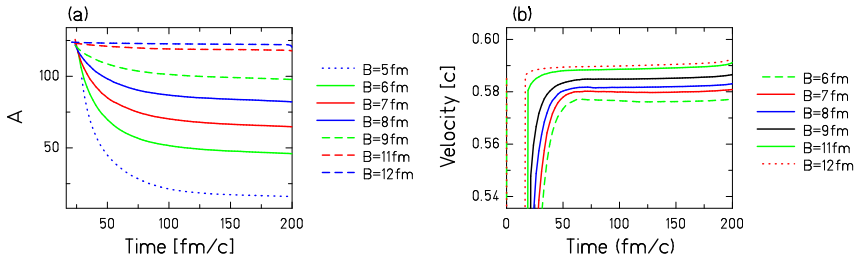


Figure 7.2: Time development of the prefragment mass (a) and the velocity in the center of mass frame (b). BUU simulation is carried out with the momentum independent (MI) mean field, SOFT EoS and In-medium cross section for different impact parameters in the collision of  $^{124}\text{Sn} + ^{124}\text{Sn}$  at 1.4 GeV. Both quantities display saturation well at the time 160 fm/c, which is the chosen time step to use as input for the evaporation code ABRABLA [GS91].

phase space occurs i.e system is thermalized.

3. **the separation phase** at  $\gtrsim 110$  fm/c, shows well separated spectator pieces and absence of the fireball cluster in the central region.

At peripheral collisions, at impact parameters  $b > 11$  fm, the size of the fireball is smaller than the projectile prefragment and the momentum transfer is insignificant compared to the friction which solely determines the velocity of the prefragment at these peripheral collisions. At about impact parameter  $b = 7$  fm this behavior stops and the velocity starts showing leveling off. Now, depending on the parameters, some calculations show a change of sign in the derivative, leading to re-acceleration. The re-acceleration of the projectile remnant at lower impact parameters may be understood in terms of the explosion of the participant zone. The explosion acts more on the rear of the spectator piece than on the front, and if the explosion is strong enough, the spectator acquires longitudinal momenta enough to overcompensate the friction effects.

In all cases, the asymptotic values of excitation energy, fragment mass and velocity are well reached till time 160 fm/c, when different clusters become separated and cease exchanging particles with the projectile prefragment, as illustrated by the time evolution plots presented in Fig. 7.2 for the  $^{124}\text{Sn} + ^{124}\text{Sn}$  system. During the early collision stage, up to time 120 fm/c, clusters may fuse if their relative energy is too small, so the clusters formed previously may disappear. Secondly clusters feel the two-body potential of several other clusters (including the target matter) leading to a large modification in the kinetic energy space during the first instants of the propagation. These two effects are thus crucial and lead to important reorganization in mass and kinetic energy of the spectator before the separation stage and de-excitation.

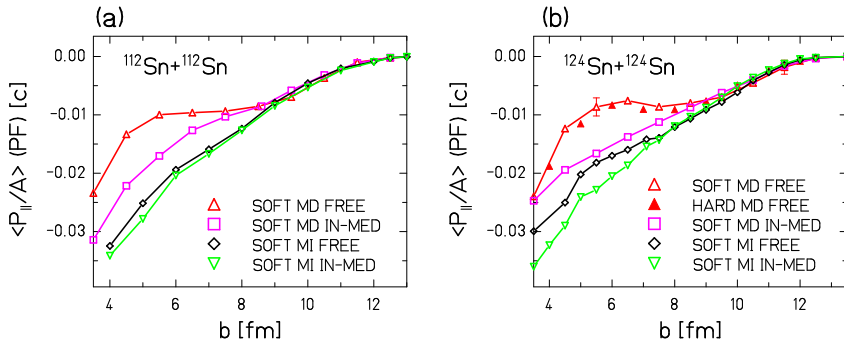


Figure 7.3: Results of the BUU simulation for the average momentum per mass of the projectile prefragment as function of impact parameter formed in the reaction  $^{112}\text{Sn} + ^{112}\text{Sn}$  at 1.4 GeV (panel a) and in  $^{124}\text{Sn} + ^{124}\text{Sn}$  at 1.4 GeV (panel b). Varied parameters are: momentum dependence of the mean field (MD/MI), nucleon-nucleon cross section (FREE/IN-MED), and to lesser extend the incompressibility of nuclear matter (SOFT/HARD). Numerical fluctuations are shown as error bars in the studied cases at  $b=5.5$  and  $b=11.5$ .

The time 160 fm/c may be taken as the definition of the freeze-out which corresponds to the end of the pre-equilibrium stage and the de-excitation step may begin. The remaining fluctuation of the presented quantities is accounted for the inaccuracies of numerical calculations. Inaccuracies cannot be fully avoided because of the Monte-Carlo nature of the code itself. In the statistical BUU calculations every output quantity is an average value calculated from the test particles. The results for the individual collision events cannot be obtained. As a results some quantities are calculated from already averaged values which may lead to unwanted consequences and to loss of information on the size of the fluctuations.

Fig.7.3 displays the results of the calculated mean longitudinal-momentum per nucleon  $\langle P_{||}/A \rangle$  of the projectile spectator residues in the both studied Sn + Sn reactions at 1.4 GeV, as the function of the impact parameter. Results are given in the projectile frame reference frame. As a general conclusion of the Fig. 7.3 it can be seen that independently of the used parameters, calculations produce the same momentum for the prefragment in most peripheral collisions at impact parameters  $b > 9$  fm. Prefragment momentum-enhancement at impact parameters  $b \lesssim 7.5$  fm can be attributed to the momentum dependent mean field and to non-reduced in-medium cross section, as was also found in the study of Shi *et al.* [SDL01]. In case of both of these momentum-enhancing parameters being applied at the same time for the  $^{124}\text{Sn} + ^{124}\text{Sn}$  calculation, the momentum of the prefragment shows local minimum i.e actual re-accelerated velocities for the smaller prefragments.

Like in the pioneering calculations presented in Ref. [SDL01], also in these simulations it was found that the hardness of the equation of state does not significantly impact the re-acceleration. Therefore only one set of calculations were devoted to the study of influence in the change of incompressibility, from soft to hard, keeping the other parameters unchanged.

## 7.2 Coupling with ABRABLA

Since we have such a good understanding of the evaporation physics, one would eagerly want to establish a connection between the observed fragment mass and the impact parameter to be able to compare the experimental data with the obtained calculations. However due to a variety of de-excitation processes, a prefragment with definite mass, may not always end up having the same mass loss. In other words de-excitation processes cause dispersion in the final mass and therefore comparison with experimental data is challenging because final masses observed in the experiment are not necessarily originated from the prefragment of same mass. In other words there is no one-to-one correlation between the two quantities due to evaporation and multifragmentation, which especially on the IMF range, where the re-acceleration is observed, are comparable. One could of course obtain this correlation by force by looking at the average prefragment mass as a function of impact parameter but this would be dangerous for two reasons: one should always keep in mind that the mean value shift is small in comparison to the widths of the velocity distributions which further are small fluctuations around the beam velocity. Any ambiguity in the correlation would increase the uncertainty in the comparison and the small deviation would be lost. Although the binary components given by the ABRABLA calculation shown in Fig. 6.3 are only 17% of the fragmentation peak, this is large enough to cause significant change in the mean value of the full measured velocity distributions. Other reason is that there is slightly larger forward velocity acceptance of the FRS. One needs to remember that the measured velocities are longitudinal velocities inside the FRS angular acceptance, which has varying impact on the observed velocity distributions depending on the width of the full velocity space populated in the reaction.

In panel a) in Fig. 7.4 the final residue mass is plotted as function of impact parameter and in panel b) as function of prefragment mass as calculated by the ABRABLA. From these plots one may easily see that one selected final mass, which is the quantity obtained from the experiments, is in fact populated from rather large variety of impact parameters or prefragment masses. One should expect the bulk experimental data to be produced in the reactions within the range of impact parameters from 5 to 14 fm. This range includes the so called friction area where the influence of different parameters were found to be small and also the re-acceleration area where the discrepancies between different

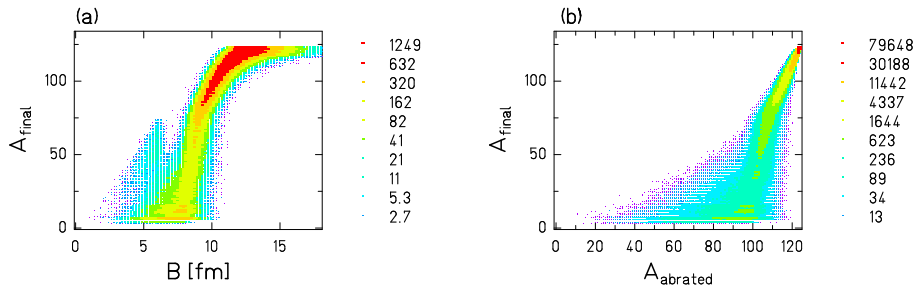


Figure 7.4: Results of the evaporation code ABRABLA for the reaction  $^{124}\text{Sn} + ^{124}\text{Sn}$  at 1.4 GeV. Calculations reveal the dispersion in the final residue mass due to the de-excitation processes as function of initial impact parameter (panel a) or as function of prefragment mass (panel b).

parameters is seen. However, in order to establish a connection between the calculations and the experimental data one does not need to establish the before discussed one-to-one correlation with impact parameter and final residue mass. Instead, the obtained velocities for the prefragments from the BUU calculations could be used as an input data to ABRABLA, and to extract the velocity distributions after the complex de-excitation processes and that after the cut due the FRS acceptance is applied to the full distributions. In other words ABRABLA is used to conform the physics to be comparable with experiment. This way, by reproducing the full velocity distributions, one is able correct also for the slightly larger forward acceptance of the FRS.

Coupling of the two codes was done in following way: from the BUU calculations a correlation between the prefragment velocity and initial impact parameter was obtained. This correlation, namely the data presented in Fig. 7.3, were fitted with a polynomial of 5th degree multiplied with a Gaussian and the obtained function was introduced to ABRABLA code. ABRABLA calculation was then performed in a usual Monte Carlo way by calculating few million de-excitations of the prefragments which each had the velocity assigned according to the impact parameter and the correlation obtained from the BUU calculation. Impact parameter was found to be good joining parameter to combine the calculations since in both codes they are well defined and considered the starting point for any further calculation. This way the codes were allowed to run rather independently and only the necessary input, the prefragment velocity, was adopted from the microscopic calculation.

The course of de-excitation has no dependence to the velocity of the prefragment. In other words the equilibrated hot prefragment, after the initial abrasion stage and pre-equilibrium emission, will go though the de-excitation process regardless of it velocity. Input from the microscopic calculations for the correc-

tions of excitation energy and angular momentum of the prefragment are out of the scope of the present work. Moreover the existing framework describing the de-excitation of the prefragment is found to have good predictive power in this energy regime and thus trusted to contain necessary accuracy.

The coupled calculations with BUU + ABRABLA were performed for both systems with two different BUU predictions producing the lowest (MI,IN-MED) and the highest (MD,FREE) residue velocities according to Fig. 7.3. The results for the mean value of the longitudinal velocity distributions obtained from these coupled calculations are shown in Fig. 7.5 together with the experimental results for both systems. The impact parameters used in the BUU calculations ranged from 4 fm to 14 fm as this range covered well the mass range measured experimentally. Complete longitudinal velocity distributions after the de-excitation and the application of the cut due the FRS angular acceptance were calculated with ABRABLA for the reactions  $^{112}\text{Sn} + ^{112}\text{Sn}$  and  $^{124}\text{Sn} + ^{124}\text{Sn}$  at 1-A GeV. From these calculated distributions the mean value was extracted with the same fitting function that was used for the experimental data. These results are discussed in the next section.

## 7.3 Discussion

These results verify that the coupled calculation is able to produce the experimental data quantitatively very well for the heavier masses. The calculated  $^{124}\text{Sn}$  projectile remnants shows slightly higher re-acceleration than the ones from  $^{112}\text{Sn}$ , which is in qualitative agreement with data. Calculations performed with set of parameters producing the smallest re-acceleration, an enhancement is still seen in the velocities of the lightest residues, in comparison to Morrissey systematics. The enhancement and eventual re-acceleration of the mean longitudinal velocities can be attributed to the interaction between the participant and spectator matter during the participant blast scenario.

In the studied systems, with the help of the ABRABLA prediction presented earlier in Fig. 6.1, one may establish a certain link between the observed mean longitudinal velocities and reaction mechanisms. In peripheral collisions at impact parameters  $b > 8$  fm, reaction mechanism manifests the features of bulk fragmentation and evaporation. The fireball size is still small and the emission from this zone towards the large spectator zone is not enough to give the spectator enough momentum to overcome the friction it suffered during the abrasion. It is also not enough to give the spectator sufficient excitation energy to enter into multifragmentation. However at about  $b = 7$  fm the systems starts populating the multifragmentation portion and at about the same impact parameter we see the final fragment velocities level off (Fig. 7.3). It is known that the multifragmentation occurs due to the increase in excitation

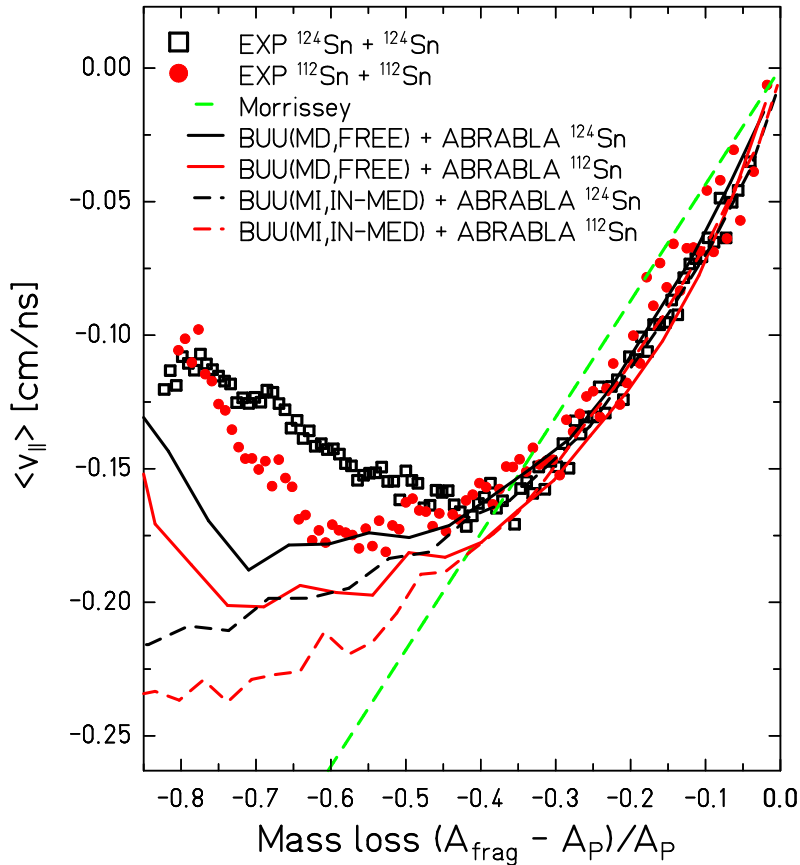


Figure 7.5: Mean values of the longitudinal velocity distributions of the final residues as measured in  $^{112}\text{Sn} + ^{112}\text{Sn}$  and in  $^{124}\text{Sn} + ^{124}\text{Sn}$  at 1.4 GeV together with the coupled calculations performed with BUU + ABRABLA. Experimental data is shown in symbols and model calculations in solid lines. Experimental error bars are not plotted for clarity. (MI,IN-MED) corresponds to the momentum independent mean field and reduced nucleon-nucleon cross section and (MD,FREE) corresponds to the momentum dependent mean field and free nucleon-nucleon cross section. All simulations are performed with the soft EOS. Calculations with these two different parameter configurations are shown for both systems because they produce the lowest (MI,IN-MED) and the highest (MD,FREE) residue velocities according to Fig. 7.3.

energy, and some of this excitation energy may be attributed to the participant blast, which would also be the cause for the enhanced forward velocities. Towards the even smaller impact parameters, down till  $b \sim 5$  fm, the scenario of multifragmentation keeps occurring while the size of the exploding participant zone increases. At the same time the spectator pieces become smaller and gain momentum from the emitted matter in the explosion that is strong enough to cause re-acceleration. At the impact parameter  $b = 5$ , the multifragmentation products will have an average mass of about 30. Due to the superposition of binary events that populate the final mass range below 30, there is a hint in the data that the re-acceleration starts to diminish. Unfortunately the range of measured data ends at  $A = 20$  but especially in the case of  $^{124}\text{Sn}$  residues there seems to be local maximum just reached at lightest measured masses. This finding supports the idea that the binary residues, which are emerging from rather peripheral collision and thus are mostly only slowed down, will cause the mean value of the superposed velocity distribution to decrease again.



# Chapter 8

## Conclusion

The high-resolving-power magnetic spectrometer, FRS, was used to measure the longitudinal velocity of the residues produced in the peripheral and mid-peripheral collisions of  $^{124}\text{Sn} + ^{124}\text{Sn}$  and  $^{112}\text{Sn} + ^{112}\text{Sn}$  at 1.4 GeV with a relative uncertainty of  $\sim 1 \times 10^{-4}$ . This precision makes it possible to investigate the mechanisms responsible for fragment formations. The production cross sections were determined from the reconstructed velocity distributions, too. The cross sections range over several orders of magnitude from  $\sim 100 \mu\text{b}$  to  $\sim 30 \text{ mb}$  with a relative uncertainty corresponding to around 20% in most cases.

The width of the longitudinal velocity distributions shows to deviate from the earlier empirical prediction by Morrissey [Mor89] and is better reproduced for broader range of data by the modified Goldhaber model [BFH<sup>+</sup>11] which includes additional corrections to the momentum distributions due to different stages of decay.

The mean value of the longitudinal velocity distributions of the heavier projectile-like residues show a decreasing trend in the mean value with increasing mass loss, which is what one would expect on the basis of the friction picture in heavy-ion collisions. However the lighter projectile-like residues show an opposite behavior, overall they appear to gain velocity with increasing mass loss. A minimum in the residue velocities is seen in the relative mass loss of  $\sim 0.4$  in both studied systems.

We have shown that within the already established theoretical framework, namely the dynamical transport code BUU coupled with a statistical abrasion-evaporation code ABRABLA, we can explain the behavior of the mean longitudinal velocity of all the produced projectile fragments. A quantitative com-

parison between the measured data and the model calculations are found to be in very good agreement with the data at the relative mass losses  $> 0.5$ , which corresponds to peripheral collisions. In this mass range the predicted final residue velocities show no variation within the studied model parameters. In mid-peripheral collisions, populating the final residues with mass losses  $< 0.5$ , the simulations show that the rapidly expanding participant zone interacts with the spectator matter giving substantial enhancement on the longitudinal velocity. The comparison with measured data seems to favor the enhancement of the explosion of the fireball due to strong momentum dependence of the nuclear mean field and due to free NN cross section. However, even the strongest obtained forward velocity enhancement in the calculations fails to quantitatively reproduce the mean velocities of the measured distributions in the lower final mass area. This discrepancy seen in this mass range was found to be about the same size as the enhancement obtained by changing the model parameters. These findings imply that the remaining deviation could be explained within the uncertainties of these parameters. Another strong indication of the models success is that the final residue velocities start to show sensitivity to the model parameters, namely the momentum dependence of the nuclear mean field and NN cross section, at the same final-mass range where the measured data shows re-acceleration.

It was also observed that the free NN cross section, compared to the reduced one, not only enhanced the spectator velocities by itself, but also enhanced the effect of the momentum dependence. In these calculations the free nucleon-nucleon cross section was the largest considered cross section but there has been indications, that in certain cases, the in-medium cross section could be even larger than the free cross section [ARS94, GLS96, ARB<sup>+</sup>95]. However the task of determining the exact parameters from the model comparison was not possible due to fact that the experimental results could be reproduced with a multitude of parameter sets.

The re-acceleration magnitude is surely ruled not only by the mean field parameters, but also by the spectator passage time. This time is ruled by the incident velocity of the projectile and the size of the reaction zone. This means that the re-acceleration of the spectator should be observed in similar conditions where also other observations, e.g. squeeze-out, related to the participant-spectator interaction are observed. In future, it would be interesting to see precise velocity analysis of the spectators from a larger range of projectile energies and in different sized systems.

Question we set out to ask was: What is the influence of the projectile isospin on the kinematical properties of projectile fragments at relativistic energies? We had in mind to restrict the problem field on that degree of freedom. However, as it turned out, the influence is rather trivial just for the re-acceleration effect. In case of the selected two systems, the observed difference in the re-

acceleration part of the velocity mean value comparison is merely due to mass difference of the projectile and not so much due to their different neutron-to-proton ratio. In other words the re-accelerating force, induced by the fireball to the spectator matter, is blind to the composition of spectator matter it encounters in the span of the  $N/Z$  values studied in the present work.



# Appendix A

## Information of the used targets

Isotope	112	114	115	116	117	118	119
Enrichment %	$99.5 \pm 0.2$	$0.2 \pm 0.1$	<0.1	<0.1	<0.1	$0.3 \pm 0.1$	<0.05
Isotope	120	122	124				
Enrichment %	<0.05	<0.05	<0.05				

Table A.1: Isotopic composition of  $^{112}\text{Sn}$  target.

Cmbpds of	Ca	Si	Fe	Cu	Ag	Al	Mg	Mn	Pb	Sb	Ni	Cr
PPM	100	50	60	5	4	1	80	15	25	<50	<50	<50

Table A.2: Chemical impurities of  $^{112}\text{Sn}$  target.

Isotope	112	114	115	116	117	118	119
Enrichment %	<0.02	<0.01	<0.2	0.2	0.14	0.5300	0.2200
Isotope	120	122	124				
Enrichment %	1.1800	0.2300	$97.5 \pm 0.2$				

Table A.3: Isotopic composition of  $^{124}\text{Sn}$  target.

Cmbpds of	Si	Fe	Cu	Al	Pb	Sb
%	0.00400	0.0100	0.00500	0.00300	0.00300	<0.00300
Cmbpds of	Bi	Zn	As	Ni	Cr	
%	<0.00200	0.00270	<0.00200	<0.00400	<0.00300	

Table A.4: Chemical impurities of  $^{124}\text{Sn}$  target.

## Appendix B

# Layers of matter in the experiment.

The trajectories of the particles passing through the FRS crosses different layers of matter, which corresponds to the different detectors, stripper foils or degraders placed along the FRS. The exact location of these layers at the intermediate S2 and at the final S4 areas are shown in figures B.1 and B.2, respectively. The thicknesses of the layers present in these experiments are listed in table B.1.

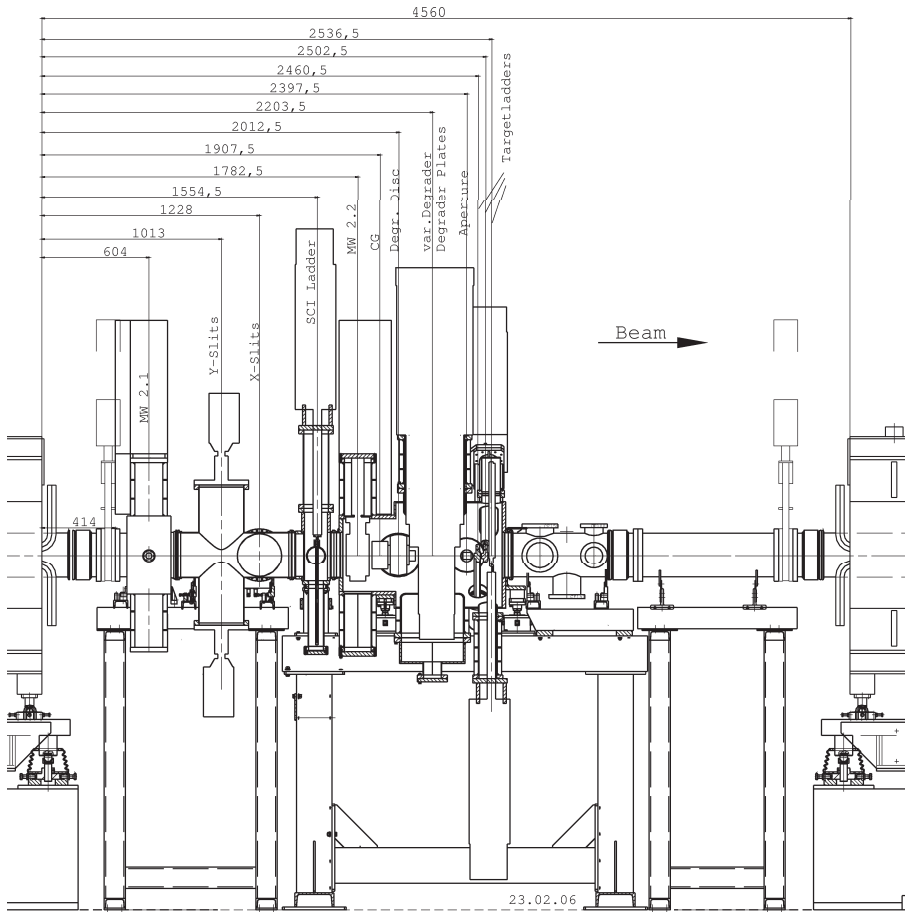


Figure B.1: Detector positions during the experiments at S2, the intermediate image plane of the FRS. After the vacuum window we have the first multiwire chamber (MW21), slits, plastic scintillator SCI21, the second multiwire chamber (MW22) and lastly the degrader. Positions of the mentioned elements are given as distances in units of mm measured from the last vacuum window of the FRS along the central beam line.

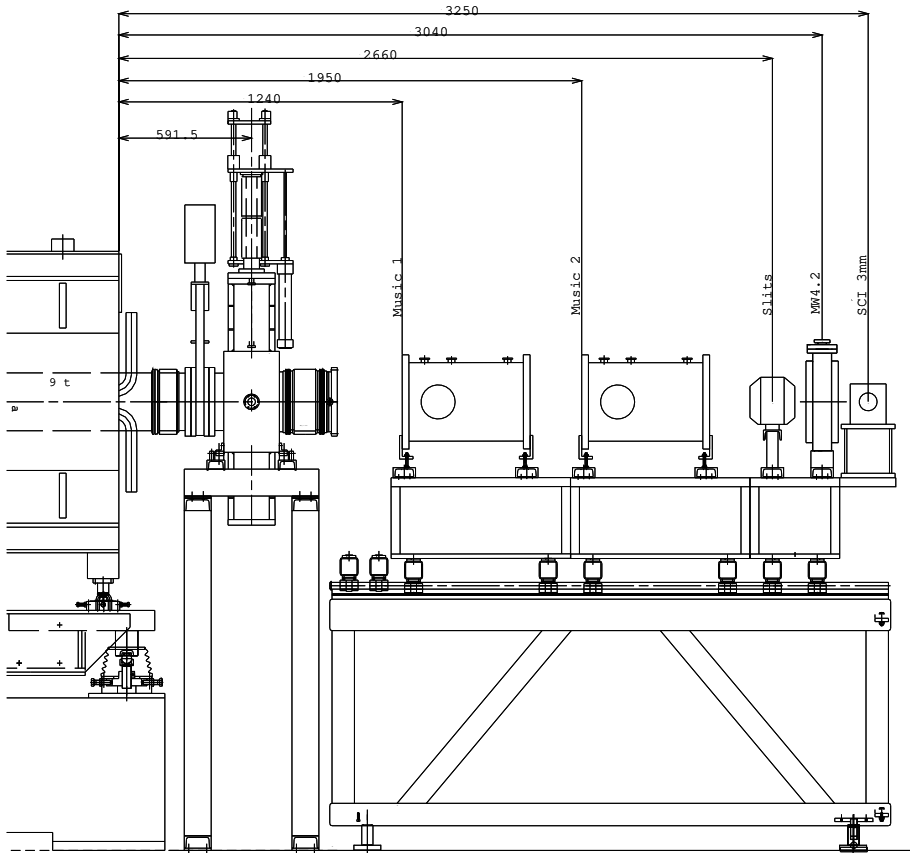


Figure B.2: Detector positions during the experiments at S4, the final image plane of the FRS. After the vacuum window we have the multiwire chamber (MW41), the first MUSIC detector (MUSIC41), the second MUSIC detector (MUSIC42), slits, the second multiwire chamber (MW42) and lastly the plastic scintillator SCI41. Positions of the mentioned elements are given as distances in units of mm measured from the last vacuum window of the FRS along the central beam line.

FRS section	Layer	Z	Thickness [ $\text{mg} \cdot \text{cm}^{-2}$ ]	Setup
S0	Vacuum window	13	4.07	Meas.
	SEETRAM	13	12.21	Calib.
	Be-target	4	6347	Calib.
	Al-target	13	1022	Calib.
	$^{112}\text{Sn}$ -target	50	126.720	Meas.
	$^{124}\text{Sn}$ -target	50	141.806	Meas.
S1	MW11	13	165	Calib.
S2	MW21	13	175	Calib.
	SCI21	13	393.4	Meas.
	MW22	13	175	Calib.
	Degrader	13	737.1	Meas.
S3	MW31	13	165	Calib.
S4	Vacuum window	22	90.2	Meas.
	MW41	13	165	Meas.
	Air gap	13	59.18	Meas.
	MUSIC1	22	90.2	Meas.
	Air gap	13	59.18	Meas.
	MUSIC2	22	90.2	Meas.
	Air gap	13	59.18	Meas.
	MW42	13	165	Meas.
	SCI41	13	355.3	Meas.

Table B.1: List of layers in the beam line. In the third column the nuclear charge of the layer material is given or if the layer consist of several different materials then the thickness is given in aluminum equivalent units ( $Z=13$ ). The setup column indicates the following: Calib.: The layer is used in the beam line during calibration runs only, Meas.: The layer is used in the beam line during the data measurement.

# Appendix C

## FRS Magnetic settings

FRS is operated in different magnetic setting in order to allow particles with different  $B\rho$  values to pass the apparatus. In tables C.1 and in C.2 the magnetic setting used to measure the data are presented. Columns 2 and 3 give the nuclear charge and the mass number, respectively, of the nucleus that is centered in the given magnetic setting. Columns 4 and 5 give the corresponding  $B\rho$  values of FRS sections 1 and 2 respectively. Columns 6 and 7 give the scaling factors for the magnets in order to obtain the given setting starting from the base setting. Column 8 report wether the degrader was present in the measurement. Column 9 reports the positions of the left and right slit, at S1, used to block the beam and/or its first two charge states from entering to S2.

#	Z	A	A/Z	$(B\rho)_{S2}$	$(B\rho)_{S4}$	$F_{S2}$	$F_{S4}$	Deg.	Slits
1	30	76.00	2.53	14.1564	14.0766	1.12275	1.12866	No	
2	30	74.86	2.50	13.9387	13.8589	1.10548	1.11120	No	
3	30	73.72	2.46	13.7209	13.6411	1.08821	1.09374	No	
4	30	72.58	2.42	13.5031	13.4232	1.07094	1.07627	No	
5	30	71.44	2.38	13.2871	13.2072	1.05380	1.05895	No	
6	30	70.30	2.34	13.0730	12.9931	1.03682	1.04178	No	-1]..
7	30	69.16	2.31	12.8588	12.7789	1.01984	1.02461	No	0]..
8	30	68.02	2.27	12.6446	12.5647	1.00285	1.00743	No	..[0.5
9	30	66.88	2.23	12.4304	12.3505	0.98586	0.99026	No	-3]..
10	30	65.74	2.19	12.2162	12.1363	0.96887	0.97308	No	
11	30	64.60	2.15	12.0020	11.9221	0.95188	0.95591	No	
12	14	35.47	2.53	14.0076	13.9020	1.11095	1.11466	Yes	
13	14	34.93	2.50	13.7902	13.6845	1.09371	1.09722	Yes	
14	14	34.40	2.46	13.5768	13.4711	1.07678	1.08011	Yes	
15	14	33.87	2.42	13.3634	13.2577	1.05986	1.06300	Yes	
16	14	33.34	2.38	13.1500	13.0443	1.04293	1.04589	Yes	..[0
17	14	32.81	2.34	12.9366	12.8308	1.02601	1.02877	Yes	-3]..[+1
18	14	32.27	2.31	12.7192	12.6134	1.00876	1.01134	Yes	-2]..[1.5
19	14	31.74	2.27	12.5058	12.4000	0.99184	0.99423	Yes	-1.5]..
20	14	31.21	2.23	12.2925	12.1867	0.97492	0.97712	Yes	
21	14	30.68	2.19	12.0791	11.9732	0.95800	0.96001	Yes	
22	14	30.15	2.15	11.8657	11.7598	0.94107	0.94290	Yes	
23	14	29.61	2.12	11.6483	11.5423	0.92383	0.92546	Yes	
24	14	29.08	2.08	11.4349	11.3985	0.90691	0.91393	No	
25	14	28.55	2.04	11.2215	11.1851	0.88998	0.89682	No	
26	14	28.02	2.00	11.0081	10.9716	0.87306	0.87970	No	
27	14	27.49	1.96	10.7947	10.7582	0.85613	0.86259	No	

Table C.1: List of FRS magnetic field setting used to measure the data in  $^{112}\text{Sn}$  +  $^{112}\text{Sn}$  experiment.

#	Z	A	A/Z	$(B\rho)_{S2}$	$(B\rho)_{S4}$	$F_{S2}$	$F_{S4}$	Deg.	Slits
1	30	76.00	2.53	14.1423	14.0625	1.01313	1.01737	No	-1.5]..[2.5
2	30	74.86	2.50	13.9281	13.8483	0.99779	1.00187	No	0]..
3	30	73.72	2.46	13.7139	13.6341	0.98244	0.98638	No	-3.5]..
4	30	72.58	2.42	13.4997	13.4198	0.96710	0.97087	No	
5	30	71.44	2.38	13.2856	13.2057	0.95176	0.95538	No	
6	30	70.30	2.34	13.0714	12.9915	0.93641	0.93989	No	
7	30	69.16	2.31	12.8572	12.7773	0.92107	0.92439	No	
8	30	68.02	2.27	12.6430	12.5631	0.90572	0.90889	No	
9	30	66.88	2.23	12.4288	12.3489	0.89038	0.89340	No	
10	30	65.74	2.19	12.2146	12.1347	0.87503	0.87790	No	
11	30	64.60	2.15	12.0005	11.9206	0.85970	0.86241	No	
12	14	35.47	2.53	14.0067	13.9011	1.00342	1.00569	Yes	-3.5]..[0.5
13	14	34.93	2.50	13.7893	13.6836	0.98784	0.98996	Yes	-2.5]..
14	14	34.40	2.46	13.5759	13.4702	0.97256	0.97452	Yes	
15	14	33.87	2.42	13.3625	13.2568	0.95727	0.95908	Yes	
16	14	33.34	2.38	13.1491	13.0434	0.94198	0.94364	Yes	
17	14	32.81	2.34	12.9358	12.8300	0.92670	0.92820	Yes	
18	14	32.27	2.31	12.7183	12.6125	0.91112	0.91247	Yes	
19	14	31.74	2.27	12.5050	12.3992	0.89584	0.89704	Yes	
20	14	31.21	2.23	12.2916	12.1857	0.88055	0.88159	Yes	
21	14	30.68	2.19	12.0782	11.9723	0.86526	0.86615	Yes	
22	14	30.15	2.15	11.8648	11.7589	0.84997	0.85071	Yes	
23	14	29.61	2.12	11.6474	11.6110	0.83440	0.84001	No	
24	14	29.08	2.08	11.4340	11.3976	0.81911	0.82457	No	
25	14	28.55	2.04	11.2206	11.1842	0.80383	0.80914	No	
26	14	28.02	2.00	11.0072	10.9707	0.78854	0.79369	No	
27	14	27.49	1.96	10.7938	10.7573	0.77325	0.77825	No	

Table C.2: List of FRS magnetic field setting used to measure the data in  $^{124}\text{Sn} + ^{124}\text{Sn}$  experiment.



# Appendix D

## Production cross-sections

Table D.1: Production cross section of nuclides produced in reactions  $^{112}\text{Sn} + ^{112}\text{Sn}$  at 1·A GeV. Data refers to the full production, corrected for the limited angular acceptance of the FRS.

$Z$	$A$	$\sigma$ [mb]	$Z$	$A$	$\sigma$ [mb]	$Z$	$A$	$\sigma$ [mb]
10	21	$18 \pm 4$	25	55	$2.8 \pm 0.6$	36	80	$3.1 \pm 0.7$
10	22	$11 \pm 2$	25	56	$1.1 \pm 0.2$	36	81	$1.1 \pm 0.3$
10	23	$1.9 \pm 0.8$	25	57	$0.32 \pm 0.07$	37	78	$2.4 \pm 0.5$
10	24	$0.9 \pm 0.4$	26	53	$0.7 \pm 0.1$	37	79	$6 \pm 1$
11	23	$16 \pm 3$	26	54	$3.2 \pm 0.6$	37	80	$11 \pm 2$
11	24	$8 \pm 2$	26	55	$7 \pm 1$	37	81	$9 \pm 2$
11	25	$2.9 \pm 0.6$	26	56	$8 \pm 2$	37	82	$3.8 \pm 0.8$
11	26	$0.8 \pm 0.2$	26	57	$3.8 \pm 0.8$	37	83	$2.0 \pm 0.6$
12	25	$13 \pm 3$	26	58	$1.3 \pm 0.3$	37	84	$1.5 \pm 0.4$
12	26	$11 \pm 2$	26	59	$0.37 \pm 0.08$	37	85	$0.18 \pm 0.04$
12	27	$3.8 \pm 0.8$	27	55	$0.40 \pm 0.08$	38	80	$1.8 \pm 0.4$
12	28	$1.0 \pm 0.2$	27	56	$2.3 \pm 0.5$	38	81	$6 \pm 1$
13	27	$15 \pm 3$	27	57	$6 \pm 1$	38	82	$12 \pm 2$
13	28	$8 \pm 2$	27	58	$8 \pm 2$	38	83	$10 \pm 2$
13	29	$4.4 \pm 0.9$	27	59	$6 \pm 1$	38	84	$6 \pm 1$
13	30	$0.6 \pm 0.2$	27	60	$1.5 \pm 0.3$	38	86	$0.9 \pm 0.3$
14	29	$12 \pm 2$	27	61	$0.5 \pm 0.1$	38	87	$0.5 \pm 0.1$
14	30	$11 \pm 2$	27	62	$0.16 \pm 0.03$	39	82	$1.2 \pm 0.3$
14	31	$3.9 \pm 0.8$	28	57	$0.24 \pm 0.05$	39	83	$6 \pm 2$
14	32	$0.9 \pm 0.2$	28	58	$1.5 \pm 0.3$	39	84	$10 \pm 2$
15	31	$9 \pm 2$	28	59	$4.9 \pm 1.0$	39	85	$14 \pm 3$
15	32	$7 \pm 1$	28	60	$8 \pm 2$	39	86	$20 \pm 6$

Table D.1 – Continued

$Z$	$A$	$\sigma$ [mb]	$Z$	$A$	$\sigma$ [mb]	$Z$	$A$	$\sigma$ [mb]
15	33	$4.4 \pm 0.9$	28	61	$7 \pm 1$	39	88	$5 \pm 2$
15	34	$0.8 \pm 0.3$	28	62	$2.1 \pm 0.4$	39	89	$0.5 \pm 0.2$
15	35	$0.4 \pm 0.1$	28	63	$0.7 \pm 0.1$	40	84	$0.9 \pm 0.2$
16	33	$7 \pm 1$	28	64	$0.25 \pm 0.05$	40	85	$4 \pm 1$
16	34	$12 \pm 2$	29	60	$1.0 \pm 0.2$	40	86	$10 \pm 2$
16	35	$4.4 \pm 0.9$	29	61	$3.7 \pm 0.7$	40	87	$14 \pm 3$
16	36	$1.1 \pm 0.2$	29	62	$7 \pm 1$	40	88	$10 \pm 2$
16	37	$0.37 \pm 0.08$	29	63	$7 \pm 1$	40	89	$3.8 \pm 0.8$
17	35	$6 \pm 1$	29	64	$2.6 \pm 0.5$	41	87	$6 \pm 2$
17	36	$8 \pm 2$	29	65	$1.0 \pm 0.2$	41	88	$9 \pm 2$
17	37	$4.9 \pm 1.0$	29	66	$0.27 \pm 0.06$	41	89	$15 \pm 3$
17	38	$2.1 \pm 0.4$	30	62	$0.7 \pm 0.1$	41	90	$11 \pm 2$
17	39	$0.5 \pm 0.1$	30	63	$3.1 \pm 0.6$	41	91	$5 \pm 1$
18	37	$4.5 \pm 0.9$	30	64	$7 \pm 1$	41	94	$0.15 \pm 0.04$
18	38	$8 \pm 2$	30	65	$8 \pm 2$	42	89	$6 \pm 3$
18	39	$5 \pm 1$	30	66	$4.4 \pm 0.9$	42	90	$8 \pm 2$
18	40	$2.5 \pm 0.5$	30	67	$1.3 \pm 0.3$	42	91	$16 \pm 3$
18	41	$0.6 \pm 0.1$	30	68	$0.5 \pm 0.1$	42	92	$12 \pm 2$
18	42	$0.22 \pm 0.05$	30	69	$0.18 \pm 0.04$	42	93	$7 \pm 1$
19	39	$3.5 \pm 0.7$	31	64	$0.43 \pm 0.09$	42	96	$0.5 \pm 0.2$
19	40	$7 \pm 1$	31	65	$2.0 \pm 0.4$	43	92	$7 \pm 1$
19	41	$5 \pm 1$	31	66	$5 \pm 1$	43	93	$16 \pm 3$
19	42	$2.8 \pm 0.6$	31	67	$8 \pm 2$	43	94	$17 \pm 3$
19	43	$1.5 \pm 0.3$	31	68	$6 \pm 1$	43	95	$10 \pm 2$
19	44	$0.29 \pm 0.06$	31	69	$2.1 \pm 0.4$	43	98	$0.8 \pm 0.3$
20	41	$3.3 \pm 0.7$	31	70	$1.7 \pm 0.7$	44	93	$5 \pm 2$
20	42	$7 \pm 1$	31	71	$0.27 \pm 0.05$	44	94	$6 \pm 1$
20	43	$6 \pm 1$	32	66	$0.32 \pm 0.06$	44	95	$15 \pm 3$
20	44	$3.6 \pm 0.7$	32	67	$1.5 \pm 0.3$	44	96	$17 \pm 4$
20	45	$1.4 \pm 0.3$	32	68	$4.9 \pm 1.0$	44	97	$11 \pm 2$
20	46	$0.34 \pm 0.07$	32	69	$8 \pm 2$	44	98	$6 \pm 3$
21	43	$2.2 \pm 0.4$	32	70	$7 \pm 1$	45	95	$2.2 \pm 0.9$
21	44	$6 \pm 1$	32	71	$2.1 \pm 0.8$	45	96	$4.7 \pm 1.0$
21	45	$8 \pm 2$	32	72	$1.2 \pm 0.4$	45	97	$14 \pm 3$
21	46	$3.6 \pm 0.7$	32	73	$0.3 \pm 0.1$	45	98	$18 \pm 4$
21	47	$1.6 \pm 0.3$	33	68	$0.24 \pm 0.05$	45	99	$15 \pm 3$
21	48	$0.40 \pm 0.08$	33	69	$1.0 \pm 0.2$	45	100	$8 \pm 3$
22	45	$1.9 \pm 0.4$	33	70	$3.3 \pm 0.7$	46	97	$1.1 \pm 0.4$
22	46	$6 \pm 1$	33	71	$8 \pm 2$	46	98	$3.9 \pm 0.8$
22	47	$8 \pm 2$	33	72	$8 \pm 2$	46	99	$12 \pm 3$
22	48	$4.7 \pm 0.9$	33	73	$3.9 \pm 0.8$	46	100	$19 \pm 4$
22	49	$1.8 \pm 0.4$	33	75	$0.44 \pm 0.09$	46	101	$19 \pm 4$

Table D.1 – Continued

$Z$	$A$	$\sigma$ [mb]	$Z$	$A$	$\sigma$ [mb]	$Z$	$A$	$\sigma$ [mb]
22	50	$0.44 \pm 0.09$	33	76	$0.16 \pm 0.03$	46	102	$12 \pm 3$
23	47	$1.3 \pm 0.3$	34	70	$0.16 \pm 0.03$	47	100	$2.8 \pm 0.6$
23	48	$4.7 \pm 0.9$	34	71	$0.9 \pm 0.2$	47	101	$10 \pm 2$
23	49	$8 \pm 2$	34	72	$3.5 \pm 0.7$	47	102	$17 \pm 3$
23	50	$5 \pm 1$	34	73	$7 \pm 1$	47	103	$27 \pm 6$
23	51	$2.2 \pm 0.4$	34	74	$10 \pm 2$	48	102	$1.6 \pm 0.3$
23	52	$0.8 \pm 0.2$	34	77	$1.9 \pm 0.8$	48	103	$7 \pm 1$
23	53	$0.19 \pm 0.04$	34	78	$0.23 \pm 0.08$	48	104	$16 \pm 3$
24	49	$1.2 \pm 0.2$	35	73	$0.33 \pm 0.07$	48	105	$29 \pm 6$
24	50	$4.5 \pm 0.9$	35	74	$1.4 \pm 0.3$	48	106	$24 \pm 10$
24	51	$8 \pm 2$	35	75	$5 \pm 1$	49	104	$0.8 \pm 0.2$
24	52	$7 \pm 1$	35	76	$9 \pm 2$	49	105	$3.5 \pm 0.7$
24	53	$1.9 \pm 0.4$	35	78	$2.7 \pm 0.6$	49	106	$9 \pm 2$
24	54	$1.0 \pm 0.2$	35	80	$0.28 \pm 0.06$	49	107	$24 \pm 5$
24	55	$0.22 \pm 0.04$	36	75	$0.7 \pm 0.1$	49	108	$24 \pm 9$
25	51	$0.8 \pm 0.2$	36	76	$3.2 \pm 0.7$	50	106	$0.32 \pm 0.07$
25	52	$3.8 \pm 0.8$	36	77	$7 \pm 2$	50	107	$1.1 \pm 0.2$
25	53	$7 \pm 1$	36	78	$12 \pm 2$	50	108	$9 \pm 2$
25	54	$7 \pm 1$	36	79	$9 \pm 2$	50	109	$20 \pm 4$

Table D.2: Production cross section of nuclides produced in reactions  $^{124}\text{Sn} + ^{124}\text{Sn}$  at 1·A GeV. Data refers to the full production, corrected for the limited angular acceptance of the FRS.

$Z$	$A$	$\sigma$ [mb]	$Z$	$A$	$\sigma$ [mb]	$Z$	$A$	$\sigma$ [mb]
10	21	$18 \pm 3$	25	52	$1.5 \pm 0.3$	35	75	$0.6 \pm 0.1$
10	22	$19 \pm 4$	25	53	$3.9 \pm 0.9$	35	76	$1.3 \pm 0.3$
10	23	$8 \pm 2$	25	54	$5 \pm 1$	35	77	$2.0 \pm 0.5$
11	23	$18 \pm 3$	25	55	$3.9 \pm 0.9$	35	78	$1.9 \pm 0.4$
11	24	$13 \pm 3$	25	56	$2.1 \pm 0.5$	35	79	$1.9 \pm 0.5$
11	25	$9 \pm 2$	25	57	$1.2 \pm 0.3$	35	80	$1.8 \pm 0.4$
12	25	$13 \pm 3$	25	58	$0.6 \pm 0.1$	35	81	$1.2 \pm 0.2$
12	26	$15 \pm 3$	26	54	$1.1 \pm 0.3$	35	82	$0.5 \pm 0.1$
12	29	$0.9 \pm 0.3$	26	55	$3.3 \pm 0.8$	36	81	$5 \pm 1$
13	27	$12 \pm 3$	26	56	$5 \pm 1$	36	82	$3 \pm 1$
13	28	$10 \pm 2$	26	57	$3.8 \pm 0.9$	36	83	$1.8 \pm 0.3$
13	29	$7 \pm 1$	26	58	$2.6 \pm 0.6$	36	84	$0.9 \pm 0.2$
13	30	$2.9 \pm 0.5$	26	59	$1.3 \pm 0.3$	36	85	$0.36 \pm 0.06$
14	29	$9 \pm 2$	26	60	$0.7 \pm 0.2$	37	84	$4 \pm 1$
14	30	$13 \pm 3$	27	56	$0.7 \pm 0.2$	37	85	$2.4 \pm 0.5$

Table D.2 – Continued

$Z$	$A$	$\sigma$ [mb]	$Z$	$A$	$\sigma$ [mb]	$Z$	$A$	$\sigma$ [mb]
14	31	$6 \pm 1$	27	57	$2.6 \pm 0.6$	37	86	$1.2 \pm 0.2$
14	32	$3.3 \pm 0.6$	27	58	$4 \pm 1$	37	87	$0.51 \pm 0.09$
14	33	$1.4 \pm 0.2$	27	59	$4 \pm 1$	37	88	$0.19 \pm 0.04$
15	31	$7 \pm 1$	27	60	$2.8 \pm 0.6$	38	86	$5 \pm 1$
15	32	$8 \pm 2$	27	61	$1.7 \pm 0.4$	38	87	$3.0 \pm 0.7$
15	33	$7 \pm 1$	27	62	$0.9 \pm 0.2$	38	88	$1.5 \pm 0.3$
15	34	$3.2 \pm 0.6$	27	63	$0.42 \pm 0.10$	38	89	$0.8 \pm 0.1$
15	35	$1.9 \pm 0.3$	28	58	$0.44 \pm 0.10$	38	90	$0.32 \pm 0.06$
15	36	$0.69 \pm 0.08$	28	59	$1.8 \pm 0.4$	39	88	$9 \pm 1$
16	33	$5 \pm 1$	28	60	$3.8 \pm 0.9$	39	89	$4 \pm 1$
16	34	$9 \pm 2$	28	61	$4 \pm 1$	39	90	$2.1 \pm 0.4$
16	35	$6 \pm 1$	28	62	$3.4 \pm 0.8$	39	91	$1.1 \pm 0.2$
16	36	$3.6 \pm 0.7$	28	63	$2.0 \pm 0.4$	39	92	$0.53 \pm 0.10$
16	37	$1.6 \pm 0.3$	28	64	$1.1 \pm 0.2$	39	93	$0.23 \pm 0.04$
16	38	$0.8 \pm 0.1$	28	65	$0.6 \pm 0.1$	40	90	$6 \pm 2$
17	35	$3.6 \pm 0.7$	28	66	$0.20 \pm 0.04$	40	91	$5 \pm 2$
17	36	$6 \pm 1$	29	60	$0.22 \pm 0.05$	40	92	$2.8 \pm 0.6$
17	37	$6 \pm 1$	29	61	$1.2 \pm 0.3$	40	93	$1.7 \pm 0.3$
17	38	$3.5 \pm 0.7$	29	62	$2.8 \pm 0.7$	40	94	$0.9 \pm 0.2$
17	39	$2.0 \pm 0.4$	29	63	$4 \pm 1$	40	95	$0.44 \pm 0.08$
17	40	$1.0 \pm 0.2$	29	64	$3.4 \pm 0.8$	40	96	$0.18 \pm 0.03$
18	37	$2.6 \pm 0.5$	29	65	$2.4 \pm 0.5$	41	92	$10.4 \pm 0.3$
18	38	$6 \pm 1$	29	66	$1.4 \pm 0.3$	41	93	$5 \pm 2$
18	39	$6 \pm 1$	29	67	$0.8 \pm 0.2$	41	94	$3.6 \pm 1.0$
18	40	$4.0 \pm 0.8$	29	68	$0.31 \pm 0.07$	41	95	$2.7 \pm 0.5$
18	41	$2.1 \pm 0.4$	30	63	$0.9 \pm 0.2$	41	96	$1.5 \pm 0.3$
18	42	$1.1 \pm 0.2$	30	64	$2.5 \pm 0.6$	41	97	$0.8 \pm 0.1$
18	43	$0.39 \pm 0.06$	30	65	$3.8 \pm 1.0$	41	98	$0.34 \pm 0.06$
19	39	$1.9 \pm 0.4$	30	66	$3.8 \pm 1.0$	42	95	$9 \pm 1$
19	40	$5 \pm 1$	30	67	$2.7 \pm 0.6$	42	96	$5 \pm 1$
19	41	$6 \pm 1$	30	68	$1.7 \pm 0.4$	42	97	$3.8 \pm 0.7$
19	42	$4.2 \pm 0.8$	30	69	$1.0 \pm 0.2$	42	98	$2.4 \pm 0.4$
19	43	$2.6 \pm 0.5$	30	70	$0.43 \pm 0.09$	42	99	$1.3 \pm 0.2$
19	44	$1.3 \pm 0.2$	30	71	$0.14 \pm 0.06$	42	100	$0.7 \pm 0.1$
19	45	$0.6 \pm 0.1$	31	65	$0.5 \pm 0.1$	43	97	$9 \pm 2$
20	41	$1.7 \pm 0.4$	31	66	$1.6 \pm 0.4$	43	98	$6 \pm 3$
20	42	$4.5 \pm 1.0$	31	67	$3.1 \pm 0.8$	43	99	$5 \pm 1$
20	43	$6 \pm 1$	31	68	$3.5 \pm 0.9$	43	100	$3.6 \pm 0.6$
20	44	$5 \pm 1$	31	69	$2.9 \pm 0.7$	43	101	$2.4 \pm 0.4$
20	45	$2.6 \pm 0.6$	31	70	$2.0 \pm 0.4$	43	102	$1.3 \pm 0.3$
20	46	$1.5 \pm 0.3$	31	71	$1.3 \pm 0.2$	44	99	$6 \pm 1$
20	47	$0.59 \pm 0.08$	31	72	$0.7 \pm 0.1$	44	100	$8 \pm 1$

Table D.2 – Continued

$Z$	$A$	$\sigma$ [mb]	$Z$	$A$	$\sigma$ [mb]	$Z$	$A$	$\sigma$ [mb]
21	43	$1.0 \pm 0.2$	31	73	$0.28 \pm 0.07$	44	101	$7 \pm 1$
21	44	$3.4 \pm 0.7$	32	67	$0.33 \pm 0.07$	44	102	$5.5 \pm 0.9$
21	45	$6 \pm 1$	32	68	$1.2 \pm 0.3$	44	103	$3.7 \pm 0.7$
21	46	$4.7 \pm 1.0$	32	69	$2.5 \pm 0.7$	44	104	$2.3 \pm 0.4$
21	47	$3.0 \pm 0.6$	32	70	$3.6 \pm 0.9$	45	102	$11 \pm 3$
21	48	$1.6 \pm 0.3$	32	71	$2.9 \pm 0.7$	45	103	$8 \pm 2$
21	49	$0.6 \pm 0.1$	32	72	$2.2 \pm 0.5$	45	104	$8 \pm 1$
22	45	$0.7 \pm 0.2$	32	73	$1.5 \pm 0.2$	45	105	$5.9 \pm 0.8$
22	46	$3.2 \pm 0.7$	32	74	$0.9 \pm 0.3$	45	106	$4.0 \pm 0.5$
22	47	$5 \pm 1$	32	75	$0.42 \pm 0.09$	46	104	$15 \pm 6$
22	48	$5 \pm 1$	32	76	$0.15 \pm 0.06$	46	105	$10 \pm 4$
22	49	$3.3 \pm 0.7$	33	69	$0.19 \pm 0.04$	46	106	$11 \pm 2$
22	50	$1.6 \pm 0.4$	33	70	$0.7 \pm 0.2$	46	107	$8 \pm 1$
22	51	$0.6 \pm 0.1$	33	71	$1.8 \pm 0.5$	46	108	$7 \pm 1$
22	52	$0.27 \pm 0.04$	33	72	$2.8 \pm 0.7$	47	106	$10 \pm 3$
23	47	$0.5 \pm 0.1$	33	73	$3.1 \pm 0.7$	47	107	$11 \pm 2$
23	48	$2.3 \pm 0.5$	33	74	$2.4 \pm 0.5$	47	108	$12 \pm 2$
23	49	$5 \pm 1$	33	75	$1.8 \pm 0.3$	47	109	$12 \pm 1$
23	50	$5 \pm 1$	33	76	$1.2 \pm 0.2$	47	110	$11 \pm 3$
23	51	$3.6 \pm 0.8$	33	77	$0.6 \pm 0.1$	48	109	$12 \pm 5$
23	52	$1.7 \pm 0.4$	33	78	$0.22 \pm 0.09$	48	110	$12 \pm 4$
23	53	$0.9 \pm 0.2$	34	71	$0.14 \pm 0.03$	48	111	$15 \pm 6$
23	54	$0.31 \pm 0.06$	34	72	$0.5 \pm 0.1$	48	112	$15 \pm 6$
24	49	$0.36 \pm 0.08$	34	73	$1.2 \pm 0.3$	49	111	$12 \pm 3$
24	50	$1.9 \pm 0.4$	34	74	$2.3 \pm 0.6$	49	112	$10 \pm 2$
24	51	$4 \pm 1$	34	75	$2.6 \pm 0.6$	49	113	$16 \pm 2$
24	52	$5 \pm 1$	34	76	$2.4 \pm 0.5$	49	114	$15 \pm 3$
24	53	$3.5 \pm 0.8$	34	77	$1.9 \pm 0.4$	50	113	$6 \pm 2$
24	54	$2.1 \pm 0.4$	34	78	$1.6 \pm 0.3$	50	114	$6 \pm 1$
24	55	$0.9 \pm 0.2$	34	79	$0.9 \pm 0.2$	50	115	$11 \pm 2$
24	56	$0.45 \pm 0.08$	34	80	$0.38 \pm 0.08$	50	116	$12 \pm 5$
25	51	$0.25 \pm 0.06$	35	74	$0.15 \pm 0.06$			



# Bibliography

- [19559] *Lectures in theoretical physics: lectures delivered at the summer institute for theoretical physics, university of colorado, boulder*, Lectures in Theoretical Physics: Lectures Delivered at the Summer Institute for Theoretical Physics, University of Colorado, Boulder, Interscience, 1959.
- [AMHS76] A. Abul-Magd, J. Hüfner, and B. Schürmann, *Friction in heavy ion reactions at relativistic energies*, Physics Letters B **60** (1976), no. 4, 327 – 330.
- [APB<sup>+</sup>88] J. Aichelin, G. Peilert, A. Bohnet, A. Rosenhauer, H. Stöcker, and W. Greiner, *Quantum molecular dynamics approach to heavy ion collisions: Description of the model, comparison with fragmentation data, and the mechanism of fragment formation*, Phys. Rev. C **37** (1988), 2451–2468.
- [ARB<sup>+</sup>95] T. Alm, G. Röpke, W. Bauer, F. Daffin, and M. Schmidt, *The in-medium nucleon-nucleon cross section and buu simulations of heavy-ion reactions*, Nuclear Physics A **587** (1995), no. 4, 815 – 827.
- [ARS94] T. Alm, G. Röpke, and M. Schmidt, *Critical enhancement of the in-medium nucleon-nucleon cross section at low temperatures*, Phys. Rev. C **50** (1994), 31–37.
- [BBB<sup>+</sup>93] G. Bizard, R. Bougault, R. Brou, J. Colin, D. Durand, A. Genoux-Lubain, J.L. Laville, C. Le Brun, J.F. Lecolley, M. Louvel, J. Péter, J.C. Steckmeyer, B. Tamain, A. Badala, T. Motobayashi, G. Rudolf, and L. Stuttgé, *From binary fission to multifragmentation in the decay of heavy excited nuclei*, Physics Letters B **302** (1993), no. 2-3, 162 – 166.
- [BBI<sup>+</sup>95] J.P. Bondorf, A.S. Botvina, A.S. Iljinov, I.N. Mishustin, and K. Sneppen, *Statistical multifragmentation of nuclei*, Physics Reports **257** (1995), no. 3, 133 – 221.

- [BD0PGB04] C.A. Bertulani, P. Danielewicz, and Institute of Physics (Great Britain), *Introduction to nuclear reactions*, Graduate student series in physics, Institute of Physics, 2004.
- [BFH<sup>+</sup>11] A. Bacquias, V. Föhr, D. Henzlova, A. Kelić-Heil, M. V. Ricciardi, and K. H. Schmidt, *Dispersion of longitudinal momentum distributions induced in fragmentation reactions*, submitted to Nucl. Instr. Meth. A.
- [BG88] G. F. Bertsch and S. Das Gupta, *A guide to microscopic models for intermediate energy heavy ion collisions*, Physics Reports **160** (1988), no. 4, 189 – 233.
- [BLT02] A. S. Botvina, O. V. Lozhkin, and W. Trautmann, *Isoscaling in light-ion induced reactions and its statistical interpretation*, Phys. Rev. C **65** (2002), no. 4, 044610.
- [BM04] A. S. Botvina and I. N. Mishustin, *Formation of hot heavy nuclei in supernova explosions*, Physics Letters B **584** (2004), no. 3-4, 233 – 240.
- [BMBB<sup>+</sup>95] A. S. Botvina, I. N. Mishustin, M. Begemann-Blaich, J. Hubele, G. Imme, I. Iori, P. Kreutz, G. J. Kunde, W. D. Kunze, V. Lindenstruth, U. Lynen, A. Moroni, W. F. J. Müller, C. A. Ogilvie, J. Pochodzalla, G. Raciti, Th. Rubehn, H. Sann, A. Schüttauf, W. Seidel, W. Trautmann, and A. Wörner, *Multifragmentation of spectators in relativistic heavy-ion reactions*, Nuclear Physics A **584** (1995), no. 4, 737 – 756.
- [BMP<sup>+</sup>91] M. Blann, M. G. Mustafa, G. Peilert, H. Stöcker, and W. Greiner, *Expectations of fragment decay from highly excited nuclei*, Phys. Rev. C **44** (1991), 431–439.
- [BP49] H. L. Bradt and B. Peters, *Nuclear collisions of heavy cosmic-ray primaries*, Phys. Rev. **75** (1949), no. 11, 1779–1780.
- [BPCS02] J. Benlliure, J. Pereira-Conca, and K. H. Schmidt, *New approach to determine the angular transmission in zero-degree magnetic spectrometers*, Nucl. Instrum. and Meth. A **478** (2002), no. 3, 493 – 505.
- [BST73] J. D. Bowman, W. J. Swiatecki, and C. F. Tsang, *ABRASION AND ABLATION OF HEAVY IONS*, LBL-2908, July 1973.
- [Car95] B. V. Carlson, *Microscopic abrasion-ablation approximation to projectile fragmentation*, Phys. Rev. C **51** (1995), 252–268.
- [CCR04] Philippe Chomaz, Maria Colonna, and Jorgen Randrup, *Nuclear spinodal fragmentation*, Physics Reports **389** (2004), no. 5-6, 263 – 440.

- [CDG<sup>+</sup>90] C. Cavata, M. Demoulin, J. Gosset, M.-C. Lemaire, D. L'Hôte, J. Poitou, and O. Valette, *Determination of the impact parameter in relativistic nucleus-nucleus collisions*, Phys. Rev. C **42** (1990), 1760–1763.
- [Cha98] R. J. Charity, *n-z distributions of secondary fragments and the evaporation attractor line*, Phys. Rev. C **58** (1998), no. 2, 1073–1077.
- [CKP94] X. Campi, H. Krivine, and E. Plagnol, *Size and excitation energy distributions of projectile spectators in multifragmentation data*, Phys. Rev. C **50** (1994), R2680–R2683.
- [CMW<sup>+</sup>88] R.J. Charity, M.A. McMahan, G.J. Wozniak, R.J. McDonald, L.G. Moretto, D.G. Sarantites, L.G. Sobotka, G. Guarino, A. Pantaleo, L. Fiore, A. Gobbi, and K.D. Hildenbrand, *Systematics of complex fragment emission in niobium-induced reactions*, Nuclear Physics A **483** (1988), no. 2, 371 – 405.
- [CSFN90] M. Cubero, M. Schönhofen, B. L. Friman, and W. Nörenberg, *Relaxation processes in intermediate-energy heavy-ion collisions*, Nuclear Physics A **519** (1990), no. 1-2, 345 – 356.
- [Dan95] P. Danielewicz, *Effects of compression and collective expansion on particle emission from central heavy-ion reactions*, Phys. Rev. C **51** (1995), 716–750.
- [Dan00] Pawel Danielewicz, *Determination of the Mean-Field Momentum-Dependence using Elliptic Flow*, Nucl. Phys. **A673** (2000), 375–410.
- [Dan09] P. Danielewicz, *Buu transport model*, private communication, 2009.
- [DB91] P. Danielewicz and G. F. Bertsch, *Production of deuterons and pions in a transport model of energetic heavy-ion reactions*, Nuclear Physics A **533** (1991), no. 4, 712 – 748.
- [dJIS97] M. de Jong, A. V. Ignatyuk, and K.-H. Schmidt, *Angular momentum in peripheral fragmentation reactions*, Nuclear Physics A **613** (1997), no. 4, 435 – 444.
- [DKLR95] D. J. Dean, S. E. Koonin, K. Langanke, and P. B. Radha, *Temperature dependence of the nuclear symmetry energy*, Physics Letters B **356** (1995), no. 4, 429 – 433.
- [DLG<sup>+</sup>98] P. Danielewicz, Roy A. Lacey, P.-B. Gossiaux, C. Pinkenburg, P. Chung, J. M. Alexander, and R. L. McGrath, *Disappearance of elliptic flow: A new probe for the nuclear equation of state*, Phys. Rev. Lett. **81** (1998), 2438–2441.

- [DP92] Paweł Danielewicz and Qiubao Pan, *Blast of light fragments from central heavy-ion collisions*, Phys. Rev. C **46** (1992), 2002–2011.
- [DPBB94] P. Donati, P. M. Pizzochero, P. F. Bortignon, and R. A. Broglia, *Temperature dependence of the nucleon effective mass and the physics of stellar collapse*, Phys. Rev. Lett. **72** (1994), no. 18, 2835–2838.
- [E+99] T. Enqvist et al., *Systematic experimental survey on projectile fragmentation and fission induced in collisions of U-238 at 1-A-GeV with lead*, Nucl. Phys. **A658** (1999), 47–66.
- [EAB+02] T. Enqvist, P. Armbruster, J. Benlliure, M. Bernas, A. Boudard, S. Czajkowski, R. Legrain, S. Leray, B. Mustapha, M. Pravikoff, F. Rejmund, K.-H. Schmidt, C. Stéphan, J. Taieb, L. Tassan-Got, F. Vivés, C. Volant, and W. Wlazlo, *Primary-residue production cross sections and kinetic energies in 1agev 208pb on deuteron reactions*, Nuclear Physics A **703** (2002), no. 1-2, 435 – 465.
- [G+92] H. Geissel et al., *The GSI projectile fragment separator (FRS): A Versatile magnetic system for relativistic heavy ions*, Nucl. Instrum. Meth. **B70** (1992), 286–297.
- [GBDG87] C. Gale, G. Bertsch, and S. Das Gupta, *Heavy-ion collision theory with momentum-dependent interactions*, Phys. Rev. C **35** (1987), 1666–1671.
- [GGL+84] Harvey Gould, Douglas Greiner, Peter Lindstrom, T. J. M. Symons, and Henry Crawford, *Electron capture by  $u^{91+}$  and  $u^{92+}$  and ionization of  $u^{90+}$  and  $u^{91+}$* , Phys. Rev. Lett. **52** (1984), no. 3, 180–183.
- [GGM+77] J. Gosset, H. H. Gutbrod, W. G. Meyer, A. M. Poskanzer, A. Sandoval, R. Stock, and G. D. Westfall, *Central collisions of relativistic heavy ions*, Phys. Rev. C **16** (1977), 629–657.
- [GH78] A S Goldhaber and H H Heckman, *High energy interactions of nuclei*, Annual Review of Nuclear and Particle Science **28** (1978), no. 1, 161–205.
- [GKK+90] H. H. Gutbrod, K. H. Kampert, B. Kolb, A. M. Poskanzer, H. G. Ritter, R. Schicker, and H. R. Schmidt, *Squeeze-out of nuclear matter as a function of projectile energy and mass*, Phys. Rev. C **42** (1990), 640–651.
- [GLS96] G. Giansiracusa, U. Lombardo, and N. Sandulescu, *Correlations in the in-medium nucleon-nucleon cross section*, Phys. Rev. C **53** (1996), R1478–R1482.

- [GM70] R. J. Glauber and G. Matthiae, *High-energy scattering of protons by nuclei*, Nucl. Phys. **B21** (1970), 135–157.
- [Gol74] A.S. Goldhaber, *Statistical models of fragmentation processes*, Physics Letters B **53** (1974), no. 4, 306 – 308.
- [GRS<sup>+</sup>87] C. Grégoire, B. Remaud, F. Sébille, L. Vinet, and Y. Raffray, *Semi-classical dynamics of heavy-ion reactions*, Nuclear Physics A **465** (1987), no. 2, 317 – 338.
- [GS91] J.-J. Gaimard and K.-H. Schmidt, *A reexamination of the abrasion-ablation model for the description of the nuclear fragmentation reaction*, Nuclear Physics A **531** (1991), no. 3-4, 709 – 745.
- [Har92] Bernard G. Harvey, *Beam-velocity fragment yields and momenta in nucleus-nucleus collisions from 20 mev/nucleon to 200 gev/nucleon*, Phys. Rev. C **45** (1992), 1748–1756.
- [HCLC89] B.G. Harvey, H.J. Crawford, P.J. Lindstrom, and A.J. Cole, *Statistical decay of fragments from  $C + {}^{12}C$ , 2.1 GeV-nucleon*, Physical Review C **39** (1989), 841–848, ISN 8885,LBL 25408.
- [Hen05] V. Henzl, *Spectator response to the participant blast*, Ph.D. thesis, TU Prague, 2005.
- [HF52] Walter Hauser and Herman Feshbach, *The inelastic scattering of neutrons*, Phys. Rev. **87** (1952), 366–373.
- [HKA<sup>+</sup>91] J. Hubele, P. Kreutz, J. C. Adloff, M. Begemann-Blaich, P. Bouissou, G. Imme, I. Iori, G. J. Kunde, S. Leray, V. Lindenstruth, Z. Liu, U. Lynen, R. J. Meijer, U. Milkau, A. Moroni, W. F. J. Müller, C. Ngô, C. A. Ogilvie, J. Pochodzalla, G. Raciti, G. Rudolf, H. Sann, A. Schüttauf, W. Seidel, L. Stuttge, W. Trautmann, and A. Tucholski, *Fragmentation of gold projectiles: From evaporation to total disassembly*, Zeitschrift für Physik A Hadrons and Nuclei **340** (1991), 263–270, 10.1007/BF01294674.
- [HKL<sup>+</sup>92] J. Hubele, P. Kreutz, V. Lindenstruth, J. C. Adloff, M. Begemann-Blaich, P. Bouissou, G. Imme, I. Iori, G. J. Kunde, S. Leray, Z. Liu, U. Lynen, R. J. Meijer, U. Milkau, A. Moroni, W. F. J. Müller, C. Ngô, C. A. Ogilvie, J. Pochodzalla, G. Raciti, G. Rudolf, H. Sann, A. Schüttauf, W. Seidel, L. Stuttge, W. Trautmann, A. Tucholski, R. Heck, A. R. DeAngelis, D. H. E. Gross, H. R. Jaqaman, H. W. Barz, H. Schulz, W. A. Friedman, and R. J. Charity, *Statistical fragmentation of au projectiles at  $E/A=600$  mev*, Phys. Rev. C **46** (1992), R1577–R1581.

- [HR01] N. Schneider H. Reeg, *Current transformers for GSI's keV/u to GeV/u ion beams -an overview*, Proceedings DIPAC 2001 - ESRF, Grenoble, France (Gesellschaft für Schwerionenforschung (GSI), Germany), 2001, pp. 120–122.
- [HSR<sup>+</sup>08] D. Henzlova, K.-H. Schmidt, M. V. Ricciardi, A. Kelić, V. Henzl, P. Napolitani, L. Audouin, J. Benlliure, A. Boudard, E. Casarejos, J. E. Ducret, T. Enqvist, A. Heinz, A. Junghans, B. Jurado, A. Krása, T. Kurtukian, S. Leray, M. F. Ordóñez, J. Pereira, R. Pleskač, F. Rejmund, C. Schmitt, C. Stéphan, L. Tassan-Got, C. Villagrasa, C. Volant, A. Wagner, and O. Yordanov, *Experimental investigation of the residues produced in the  $^{136}\text{Xe} + \text{pb}$  and  $^{124}\text{Xe} + \text{pb}$  fragmentation reactions at 1a gev*, Phys. Rev. C **78** (2008), no. 4, 044616.
- [HSS75] J. Hufner, K. Schafer, and B. Schurmann, *Abrasion-ablation in reactions between relativistic heavy ions*, Phys. Rev. **C12** (1975), 1888–1898.
- [JCG<sup>+</sup>96] A. Junghans, H. G. Clerc, A. Grewe, M. de Jong, J. Müller, and K.-H. Schmidt, *A self-calibrating ionisation chamber for the precise intensity calibration of high-energy heavy-ion beam monitors*, Nucl. Instrum. and Meth. A **370** (1996), no. 2-3, 312 – 314.
- [JdJC<sup>+</sup>98] A.R. Junghans, M. de Jong, H.-G. Clerc, A.V. Ignatyuk, G.A. Kudyaev, and K.-H. Schmidt, *Projectile-fragment yields as a probe for the collective enhancement in the nuclear level density*, Nuclear Physics A **629** (1998), no. 3-4, 635 – 655.
- [JSB02] B. Jurado, K.-H. Schmidt, and K.-H. Behr, *Application of a secondary-electron transmission monitor for high-precision intensity measurements of relativistic heavy-ion beams*, Nucl. Instrum. and Meth. A **483** (2002), no. 3, 603 – 610.
- [KABB<sup>+</sup>93] P. Kreutz, J.C. Adloff, M. Begemann-Blaich, P. Bouissou, J. Hubele, G. Imme, I. Iori, G.J. Kunde, S. Leray, V. Lindenstruth, Z. Liu, U. Lynen, R.J. Meijer, U. Milkau, A. Moroni, W.F.J. Müller, C. Ngô, C.A. Ogilvie, J. Pochodzalla, G. Raciti, G. Rudolf, H. Sann, A. Schüttauf, W. Seidel, L. Stuttge, W. Trautmann, and A. Tucholski, *Charge correlations as a probe of nuclear disassembly*, Nuclear Physics A **556** (1993), no. 4, 672 – 696.
- [Kie88] P. Kienle, *Studies of radioactive decays of completely ionized nuclei in a heavy ion storage ring*, Nucl. Instrum. and Meth. A **271** (1988), no. 2, 277 – 279.

- [KPA<sup>+</sup>07] A. Klimkiewicz, N. Paar, P. Adrich, M. Fallot, K. Boretzky, T. Aumann, D. Cortina-Gil, U. Datta Pramanik, Th. W. Elze, H. Emling, H. Geissel, M. Hellström, K. L. Jones, J. V. Kratz, R. Kulesa, C. Nociforo, R. Palit, H. Simon, G. Surówka, K. Sümmerer, D. Vretenar, and W. Waluś, *Nuclear symmetry energy and neutron skins derived from pygmy dipole resonances*, Phys. Rev. C **76** (2007), no. 5, 051603.
- [KRS09] Aleksandra Kelic, M. Valentina Ricciardi, and Karl-Heinz Schmidt, *ABLA07 - towards a complete description of the decay channels of a nuclear system from spontaneous fission to multifragmentation*.
- [LGL09] G. Lehaut, F. Gulminelli, and O. Lopez, *Isoscaling as a measure of symmetry energy in the lattice gas model*, Phys. Rev. Lett. **102** (2009), no. 14, 142503.
- [LL90] Francois Lamarche and Claude Leroy, *Evaluation of the volume of intersection of a sphere with a cylinder by elliptic integrals*, Computer Physics Communications **59** (1990), no. 2, 359 – 369.
- [Mor89] D. J. Morrissey, *Systematics of momentum distributions from reactions with relativistic ions*, Phys. Rev. C **39** (1989), no. 2, 460–470.
- [MS66] William D. Myers and Wladyslaw J. Swiatecki, *Nuclear masses and deformations*, Nuclear Physics **81** (1966), no. 1, 1 – 60.
- [MS74] W.D Myers and W.J Swiatecki, *The nuclear droplet model for arbitrary shapes*, Annals of Physics **84** (1974), no. 1-2, 186 – 210.
- [MS83] William D. Myers and Karl-Heinz Schmidt, *An update on droplet-model charge distributions*, Nuclear Physics A **410** (1983), no. 1, 61 – 73.
- [NSB<sup>+</sup>04] P. Napolitani, K.-H. Schmidt, A. S. Botvina, F. Rejmund, L. Tassan-Got, and C. Villagrasa, *High-resolution velocity measurements on fully identified light nuclides produced in  $^{56}\text{Fe} + \text{hydrogen}$  and  $^{56}\text{Fe} + \text{titanium}$  systems*, Phys. Rev. C **70** (2004), no. 5, 054607.
- [NSTG<sup>+</sup>07] P. Napolitani, K.-H. Schmidt, L. Tassan-Got, P. Armbruster, T. Enqvist, A. Heinz, V. Henzl, D. Henzlova, A. Kelić, R. Pleskač, M. V. Ricciardi, C. Schmitt, O. Yordanov, L. Audouin, M. Bernas, A. Lafriaskh, F. Rejmund, C. Stéphan, J. Benlliure, E. Casarejos, M. Fernandez Ordonez, J. Pereira, A. Boudard, B. Fernandez, S. Leray, C. Villagrasa, and

- C. Volant, *Measurement of the complete nuclide production and kinetic energies of the system  $^{136}\text{Xe}+\text{hydrogen}$  at 1 gev per nucleon*, Phys. Rev. C **76** (2007), no. 6, 064609.
- [NSTG11] P. Napolitani, K.-H. Schmidt, and L. Tassan-Got, *Inclusive selection of intermediate-mass-fragment formation modes in the spallation of  $^{136}\text{Xe}$* , Journal of Physics G: Nuclear and Particle Physics **38** (2011), no. 11, 115006.
- [OABB<sup>+</sup>91] C. A. Ogilvie, J. C. Adloff, M. Begemann-Blaich, P. Bouissou, J. Hubele, G. Imme, I. Iori, P. Kreutz, G. J. Kunde, S. Leray, V. Lindenstruth, Z. Liu, U. Lynen, R. J. Meijer, U. Milkau, W. F. J. Müller, C. Ng, J. Pochodzalla, G. Raciti, G. Rudolf, H. Sann, A. Schüttauf, W. Seidel, L. Stuttge, W. Trautmann, and A. Tucholski, *Rise and fall of multifragment emission*, Phys. Rev. Lett. **67** (1991), 1214–1217.
- [ODR79] Luiz F. Oliveira, Raul Donangelo, and John O. Rasmussen, *Abrasion-ablation calculations of large fragment yields from relativistic heavy ion reactions*, Phys. Rev. C **19** (1979), 826–833.
- [OHMO92] Akira Ono, Hisashi Horiuchi, Toshiki Maruyama, and Akira Ohnishi, *Antisymmetrized version of molecular dynamics with two-nucleon collisions and its application to heavy ion reactions*, Progress of Theoretical Physics **87** (1992), no. 5, 1185–1206.
- [PCG<sup>+</sup>96] R. Pak, D. Craig, E. E. Gualtieri, S. A. Hannuschke, R. A. Lacey, J. Lauret, W. J. Llope, N. T. B. Stone, A. M. Vander Molen, G. D. Westfall, and J. Yee, *Radial flow in  $^{40}\text{Ar}+^{45}\text{Sc}$  reactions at  $E = 35\sim 115$  mev/nucleon*, Phys. Rev. C **54** (1996), 1681–1687.
- [PGM<sup>+</sup>94] M. Pfützner, H. Geissel, G. Münzenberg, F. Nickel, Ch. Scheidenberger, K.-H. Schmidt, K. Sümmerer, T. Brohm, B. Voss, and H. Bichsel, *Energy deposition by relativistic heavy ions in thin argon absorbers*, Nucl. Instrum. and Meth. B **86** (1994), no. 3-4, 213 – 218.
- [PMR<sup>+</sup>95] J. Pochodzalla, T. Möhlenkamp, T. Rubehn, A. Schüttauf, A. Wörner, E. Zude, M. Begemann-Blaich, Th. Blaich, H. Em-ling, A. Ferrero, C. Gross, G. Immé, I. Iori, G. J. Kunde, W. D. Kunze, V. Lindenstruth, U. Lynen, A. Moroni, W. F. J. Müller, B. Ocker, G. Raciti, H. Sann, C. Schwarz, W. Seidel, V. Serfling, J. Stroth, W. Trautmann, A. Trzcinski, A. Tucholski, G. Verde, and B. Zwieglinski, *Probing the nuclear liquid-gas phase transition*, Phys. Rev. Lett. **75** (1995), no. 6, 1040–1043.
- [Poc97] J. Pochodzalla, *The search for the liquid-gas phase transition in nuclei*, Prog. Part. Nucl. Phys. **39** (1997), 443–501.

- [R<sup>+</sup>06] M. V. Ricciardi et al., *Light nuclides produced in the proton induced spallation of U-238 at 1-GeV*, Phys. Rev. **C73** (2006), 014607.
- [RAA<sup>+</sup>10] W. Reisdorf, A. Andronic, R. Averbeck, M.L. Benabderrahmane, O.N. Hartmann, N. Herrmann, K.D. Hildenbrand, T.I. Kang, Y.J. Kim, M. Kis, P. Koczon, T. Kress, Y. Leifels, M. Merschmeyer, K. Piasecki, A. Schüttauf, M. Stockmeier, V. Barret, Z. Basrak, N. Bastid, R. Caplar, P. Crochet, P. Dupieux, M. Dzelalija, Z. Fodor, P. Gasik, Y. Grishkin, B. Hong, J. Kecskemeti, M. Kirejczyk, M. Korolija, R. Kotte, A. Lebedev, X. Lopez, T. Matulewicz, W. Neubert, M. Petrovici, F. Rami, M.S. Ryu, Z. Seres, B. Sikora, K.S. Sim, V. Simion, K. Siwek-Wilczynska, V. Smolyankin, G. Stoicea, Z. Tyminski, K. Wisniewski, D. Wohlfarth, Z.G. Xiao, H.S. Xu, I. Yushmanov, and A. Zhilin, *Systematics of central heavy ion collisions in the 1a gev regime*, Nuclear Physics A **848** (2010), no. 3-4, 366 – 427.
- [REP<sup>+</sup>03] M. V. Ricciardi, T. Enqvist, J. Pereira, J. Benlliure, M. Bernas, E. Casarejos, V. Henzl, A. Kelić, J. Taïeb, and K.-H. Schmidt, *Experimental indications for the response of the spectators to the participant blast*, Phys. Rev. Lett. **90** (2003), no. 21, 212302.
- [RIJS00] F. Rejmund, A. V. Ignatyuk, A. R. Junghans, and K. H. Schmidt, *Pair breaking and even-odd structure in fission-fragment yields*, Nuclear Physics A **678** (2000), no. 3, 215 – 234.
- [RR97] W. Reisdorf and H. G. Ritter, *Collective flow in heavy-ion collisions*, Ann. Rev. Nucl. Part. Sci. **47** (1997), 663–709.
- [S<sup>+</sup>92] M. Steiner et al., *Preliminary measurements of SIS 18 beam parameters*, Nucl. Instrum. Meth. **A312** (1992), 420–424.
- [SB00] K. Sümmerer and B. Blank, *Modified empirical parametrization of fragmentation cross sections*, Phys. Rev. C **61** (2000), no. 3, 034607.
- [SBA<sup>+</sup>98] W. Schwab, M. Bernas, P. Armbruster, S. Czajkowski, Ph. Dessagne, C. Donzaud, H. Geissel, A. Heinz, C. Kozhuharov, C. Miché, G. Münzenberg, M. Pfützner, C. Stéphan, K. Sümmerer, L. Tassan-Got, and B. Voss, *Fission of highly excited fragments from collisions of 750 A MeV <sup>238</sup>U-ions on <sup>208</sup>Pb*, Eur. Phys. J. A **2** (1998), no. 2, 179–191.
- [SBB<sup>+</sup>98] S. Steinhäuser, J. Benlliure, C. Böckstiegel, H. G. Clerc, A. Heinz, A. Grewe, M. de Jong, A. R. Junghans, J. Müller, M. Pfützner, and K. H. Schmidt, *Odd-even effects observed in*

- the fission of nuclei with unpaired protons*, Nuclear Physics A **634** (1998), no. 1-2, 89 – 111.
- [SBC<sup>+</sup>93] K. H. Schmidt, T. Brohm, H. G. Clerc, M. Dornik, M. Fauerbach, H. Geissel, A. Grewe, E. Hanelt, A. Junghans, A. Magel, W. Morawek, G. Münzenberg, F. Nickel, M. Pfützner, C. Scheidenberger, K. Sümmerer, D. Vieira, B. Voss, and C. Ziegler, *Distribution of ir and pt isotopes produced as fragments of 1 a gev <sup>197</sup>au projectiles: a thermometer for peripheral nuclear collisions.*, Physics Letters B **300** (1993), no. 4, 313 – 316.
- [SBE<sup>+</sup>98] P. Spädtke, J. Bossler, H. Emig, K. D. Leible, C. Mühle, H. Reich, H. Schulte, and K. Tinschert, *Ion source development at gsi*, Ion source development at GSI, vol. 69, AIP, 1998, pp. 1079–1081.
- [Sch] K. H. Schmidt, *Amadeus (a magnet and degrader utility for scaling)*, <http://www.gsi.de/charms/amadeus.htm>.
- [SDL01] L. Shi, P. Danielewicz, and R. Lacey, *Spectator response to the participant blast*, Phys. Rev. C **64** (2001), no. 3, 034601.
- [Sen04] P. Senger, *Particle production in heavy-ion collisions*, Prog. Part. Nucl. Phys. **53** (2004), 1–23.
- [SGF<sup>+</sup>91] Th. Stöhlker, H. Geissel, H. Folger, C. Kozhuharov, P.H. Mokler, G. Münzenberg, D. Schardt, Th. Schwab, M. Steiner, H. Stelzer, and K. Sümmerer, *Equilibrium charge state distributions for relativistic heavy ions*, Nucl. Instrum. and Meth. B **61** (1991), no. 4, 408 – 410.
- [SKW<sup>+</sup>96] A. Schüttauf, W. D. Kunze, A. Wörner, M. Begemann-Blaich, Th. Blaich, D. R. Bowman, R. J. Charity, A. Cosmo, A. Ferrero, C. K. Gelbke, C. Groß, W. C. Hsi, J. Hubele, G. Immé, I. Iori, J. Kempter, P. Kreutz, G. J. Kunde, V. Lindenstruth, M. A. Lisa, W. G. Lynch, U. Lynen, M. Mang, T. Möhlenkamp, A. Moroni, W. F. J. Müller, M. Neumann, B. Ocker, C. A. Ogilvie, G. F. Peaslee, J. Pochodzalla, G. Raciti, F. Rosenberger, Th. Rubehn, H. Sann, C. Schwarz, W. Seidel, V. Serfling, L. G. Sobotka, J. Stroth, L. Stuttge, S. Tomasevic, W. Trautmann, A. Trzcinski, M. B. Tsang, A. Tucholski, G. Verde, C. W. Williams, E. Zude, and B. Zwieglinski, *Universality of spectator fragmentation at relativistic bombarding energies*, Nuclear Physics A **607** (1996), no. 4, 457 – 486.
- [SLM94] F. D. Swesty, J. M. Lattimer, and E. S. Myra, *The role of the equation of state in the 'prompt' phase of type ii supernovae*, ApJ **425** (1994), 195–204.

- [SRBE02] K.-H. Schmidt, M.V. Ricciardi, A.S. Botvina, and T. Enqvist, *Production of neutron-rich heavy residues and the freeze-out temperature in the fragmentation of relativistic  $^{238}\text{U}$  projectiles determined by the isospin thermometer*, Nuclear Physics A **710** (2002), no. 1-2, 157 – 179.
- [SSB<sup>+</sup>00] K. H. Schmidt, S. Steinhäuser, C. Böckstiegel, A. Grewe, A. Heinz, A. R. Junghans, J. Benlliure, H. G. Clerc, M. de Jong, J. Müller, M. Pfützner, and B. Voss, *Relativistic radioactive beams: A new access to nuclear-fission studies*, Nuclear Physics A **665** (2000), no. 3-4, 221 – 267.
- [Ste91] Herbert Stelzer, *Multiwire chambers with a two-stage gas amplification*, Nucl. Instrum. and Meth. A **310** (1991), no. 1-2, 103 – 106.
- [Tra05] W. Trautmann, *Multifragmentation and the liquid-gas phase transition: an experimental overview*, Nuclear Physics A **752** (2005), 407 – 416, Proceedings of the 22nd International Nuclear Physics Conference (Part 2).
- [Tra08] W Trautmann,  *$N/z$  dependence of projectile fragmentation*, International Journal of Modern Physics E **17** (2008), no. 9, 1838–1849.
- [TZD<sup>+</sup>09] M. B. Tsang, Yingxun Zhang, P. Danielewicz, M. Famiano, Zhuxia Li, W. G. Lynch, and A. W. Steiner, *Constraints on the density dependence of the symmetry energy*, Phys. Rev. Lett. **102** (2009), no. 12, 122701.
- [UU33] E. A. Uehling and G. E. Uhlenbeck, *Transport phenomena in einstein-bose and fermi-dirac gases. i*, Phys. Rev. **43** (1933), 552–561.
- [WDD<sup>+</sup>94] M. Weber, C. Donzaud, J.P. Dufour, H. Geissel, A. Grewe, D. Guillemaud-Mueller, H. Keller, M. Lewitowicz, A. Magel, A.C. Mueller, G. Münzenberg, F. Nickel, M. Pfützner, A. Piechaczek, M. Pravikoff, E. Roeckl, K. Rykaczewski, M.G. Saint-Laurent, I. Schall, C. Stéphan, K. Sümmerer, L. Tassan-Got, D.J. Vieira, and B. Voss, *Longitudinal momenta and production cross-sections of isotopes formed by fragmentation of a 500 amev  $^{86}\text{Kr}$  beam*, Nuclear Physics A **578** (1994), no. 3-4, 659 – 672.
- [WE40] V. F. Weisskopf and D. H. Ewing, *On the yield of nuclear reactions with heavy elements*, Phys. Rev. **57** (1940), 472–485.

- [WGJ<sup>+</sup>76] G. D. Westfall, J. Gosset, P. J. Johansen, A. M. Poskanzer, W. G. Meyer, H. H. Gutbrod, A. Sandoval, and R. Stock, *Nuclear fire-ball model for proton inclusive spectra from relativistic heavy-ion collisions*, Phys. Rev. Lett. **37** (1976), 1202–1205.
- [WMO<sup>+</sup>00] A. Wagner, C. Müntz, H. Oeschler, C. Sturm, R. Barth, M. Cieřlak, M. Dębowski, E. Grosse, P. Koczoń, F. Laue, M. Mang, D. Miřkowiec, E. Schwab, P. Senger, P. Beckerle, D. Brill, Y. Shin, H. Ströbele, W. Waluř, B. Kohlmeyer, F. Pühlhofer, J. Speer, and I. K. Yoo, *Emission pattern of high-energy pions: A new probe for the early phase of heavy-ion collisions*, Phys. Rev. Lett. **85** (2000), 18–21.
- [YF79] Y. Yariv and Z. Fraenkel, *Intranuclear cascade calculation of high-energy heavy-ion interactions*, Phys. Rev. C **20** (1979), 2227–2243.
- [YHG<sup>+</sup>09] T.-Z. Yan, S.-K. Hu, W.-X. Guo, S.-L. Wang, and J.-P. Xu, *NUCLEAR PHYSICS: Isospin Effects on Anisotropic Flows in Intermediate Energy Heavy Ion Collisions*, Chinese Physics Letters **26** (2009), no. 11, 112501–+.